REPORT DOCUMENTATION PAGE

Form Approved
OMB No. 0704-0188

1. REPORT DATE *(DD-MM-YYYY)*	2. REPORT TYPE	3. DATES COVERED *(From - To)*
16/Oct/2001	THESIS	

4. TITLE AND SUBTITLE
VALIDATION OF AN IMPROVED COMPUTER ALGORITHM FOR PRECIPITATION ECHO CLASSIFICATION

5a. CONTRACT NUMBER

5b. GRANT NUMBER

5c. PROGRAM ELEMENT NUMBER

6. AUTHOR(S)
2D LT AMRHEIN EDWARD T

5d. PROJECT NUMBER

5e. TASK NUMBER

5f. WORK UNIT NUMBER

7. PERFORMING ORGANIZATION NAME(S) AND ADDRESS(ES)
TEXAS A&M UNIVERSITY

8. PERFORMING ORGANIZATION REPORT NUMBER
CI01-264

9. SPONSORING/MONITORING AGENCY NAME(S) AND ADDRESS(ES)
THE DEPARTMENT OF THE AIR FORCE
AFIT/CIA, BLDG 125
2950 P STREET
WPAFB OH 45433

10. SPONSOR/MONITOR'S ACRONYM(S)

11. SPONSOR/MONITOR'S REPORT NUMBER(S)

12. DISTRIBUTION/AVAILABILITY STATEMENT
Unlimited distribution
In Accordance With AFI 35-205/AFIT Sup 1

13. SUPPLEMENTARY NOTES

14. ABSTRACT

15. SUBJECT TERMS

16. SECURITY CLASSIFICATION OF:			17. LIMITATION OF ABSTRACT	18. NUMBER OF PAGES	19a. NAME OF RESPONSIBLE PERSON
a. REPORT	b. ABSTRACT	c. THIS PAGE		132	19b. TELEPHONE NUMBER *(Include area code)*

VALIDATION OF AN IMPROVED COMPUTER ALGORITHM FOR PRECIPITATION ECHO CLASSIFICATION

A Thesis

by

EDWARD THOMAS AMRHEIN

Submitted to the Office of Graduate Studies of
Texas A&M University
in partial fulfillment of the requirements for the degree of

MASTER OF SCIENCE

December 2001

Major Subject: Atmospheric Sciences

VALIDATION OF AN IMPROVED COMPUTER ALGORITHM FOR PRECIPITATION ECHO CLASSIFICATION

A Thesis

by

EDWARD THOMAS AMRHEIN

Submitted to Texas A&M University
in partial fulfillment of the requirements for the degree of

MASTER OF SCIENCE

Approved as to style and content by:

Michael I. Biggerstaff
(Chair of Committee)

Richard E. Orville
(Member)

Richard W. Ermel
(Member)

Gerald R. North
(Head of Department)

December 2001

Major Subject: Atmospheric Sciences

VALIDATION OF AN IMPROVED COMPUTER ALGORITHM FOR PRECIPITATION ECHO CLASSIFICATION

A Thesis

by

EDWARD THOMAS AMRHEIN

Submitted to Texas A&M University
in partial fulfillment of the requirements for the degree of

MASTER OF SCIENCE

Approved as to style and content by:

Michael I. Biggerstaff
(Chair of Committee)

Richard E. Orville
(Member)

Richard W. Ermel
(Member)

Gerald R. North
(Head of Department)

December 2001

Major Subject: Atmospheric Sciences

ABSTRACT

Validation of an Improved Computer Algorithm for Precipitation Echo Classification.

(December 2001)

Edward Thomas Amrhein, B.S., Texas A&M University

Chair of advisory Committee: Dr. Michael I. Biggerstaff

A validation of an improved radar reflectivity partitioning scheme was performed using radar data collected for three separate precipitation systems in Central Texas. The improved algorithm was compared to a previously accepted method. Validation was performed using separate convective and stratiform mean vertical reflectivity profiles and mean vertical velocity profiles derived from dual-Doppler velocity data. The results were further validated through the use of convective and stratiform reflectivity and vertical velocity contour frequency by altitude diagrams (CFAD). As a final check, frequency distributions of reflectivity lapse rates in the mixed phase region were also examined.

The results show that the new algorithm brings us a step closer in properly partitioning radar reflectivity data into its convective and stratiform parts. However, a few more modifications are needed in order to make it a more functional algorithm.

The views expressed in this article are those of the author and do not reflect the official policy or position of the United States Air Force, Department of Defense, or the U.S. Government

In loving memory of Kevin P. Roberts

Sleep
Sleep tonight
And may your dreams
Be realized
If the thunder cloud
Passes rain
So let it rain
Rain down on him
So let it be
So let it be

--From "MLK" by U2 (1984)

ACKNOWLEDGEMENTS

I could not have completed this project without the help and support of many people. First I would like to express my heartfelt gratitude to my advisor, Dr. Biggerstaff, for inspiring me to pursue an education beyond the undergraduate level. While attending Texas A&M as an undergraduate, I had no interest in research and would say that I would "never" go to school again. On several occasions, Dr. Biggerstaff gave me the opportunity to see first hand what research is all about. Needless to say, I changed my mind and developed an interest in research.

Next I would like to thank Dr. Orville for stepping in at the last minute and joining my committee. Thanks for your patience and understanding. I would also like to express my gratitude to Dr. Ermel for being a member of my committee as well as and for the friendship our families share.

I am also grateful for all of the technical help, moral support, and friendship provided by Gordon Carrie, Kerry Moncla, and Dan Jamieson. Gordon was extremely instrumental in helping me with computer programs while Kerry and Dan spent numerous hours in editing radar data and performing the dual-Doppler analysis for my dataset.

I would also like to extend my deepest thanks to Maj. Zucarello and Maj. Luke Whitney of the Air Force Institute of Technology for taking a chance on a "butter bar" (a Second Lieutenant). They allowed me to stay at Texas A&M to further my education after completing my bachelors degree and Officer Training School, something usually unheard of for a Second Lieutenant.

Furthermore, I could not have completed this without the continuous love and support from my wife and daughter. During the past ten years, they have stood by me even when I spent many hours away in order to study and do research. They were also a great source of motivation during those difficult and challenging times.

Finally, I would like to pay tribute to my dear friend Kevin P. Roberts. Kevin and I attended high school together and like most high school friends we went our separate ways after graduating in May of 1985. I enlisted in the U.S. Air Force as a meteorologist and he went on to attend Texas A&M University. While at Texas A&M, he was a very dedicated member of the Fightin' Texas Aggie Band and served as a Drum Major for the band during his senior year.

Upon my return from Desert Storm in 1991, I had no goals in mind. Later that year, Kevin invited me to attend my first Aggie Bonfire and the Texas A&M - t.u. football game played at Kyle Field. Before attending those events, I never paid attention to the two schools and the rivalry nor was I aware of the deep traditions at A&M. After attending these events and walking around on campus, Kevin made sure I took a spark from the Bonfire with me, for I went home with a dream and a goal—I wanted to be an Aggie.

Becoming an Aggie required that I attend the university, but I was still on active duty in the Air Force. Kevin urged me to pursue my goal anyway. After spending six years to complete two years of night school at the local community college I earned an Air Force scholarship that paid my tuition while allowing me to stay on active duty and receive a monthly salary.

I started my studies at Texas A&M in the spring semester of 1997. During the two and half years of my undergraduate studies, Kevin would often visit us in Aggieland and participate in many of the Aggie traditions with my family and me.

On April 27, 1999, Kevin lost his life when the twin-engine plane he was piloting crashed in Oklahoma. About two weeks later, I walked across the stage and received my diploma—a dream realized.

TABLE OF CONTENTS

Page

LIST OF FIGURES

Page

Page

Page

Page

CHAPTER I

INTRODUCTION

Radar technology was first employed in the field of meteorology in the 1940's and was simply used as a tool to locate and track regions of rain (Burgess and Ray 1986, 85-117). In the late 40's and early 50's, hardware improvements were made that allowed more of a quantitative investigation of rain. The genealogical tree of radar meteorology, developed by Atlas and Ulbrich (1990, 86-97), shows that radar measurements of rainfall have been a widely studied topic focusing on a vast array of problems. Some of these problems, depicted as branches, include the empirical Z-R relationships (reflectivity [Z] to rainrate [R]), attenuation of the radar signal, and the radar bright band structure (Austin and Bemis 1950; Zawadzki 1984; Austin 1987; Joss 1990, 619-647).

Today, these branches of investigation are still growing. Improvements in computer technology have led to significant improvements in both the hardware and the software used in the radar itself, such as seen in the fielding of the Weather Surveillance Radar--1988 Doppler System (WSR-88D) radar network (Burgess and Lemon 1990, 619-647; Crum and Alberty 1993). Previous operational weather radar systems did not have the ability to quantitatively estimate rainfall in real-time for use in weather forecasting and flash flood warnings. The WSR-88D however, incorporates computer-based algorithms of Z-R relationships to provide real-time estimates of accumulated

---

This thesis follows the style and format of *Journal of Applied Meteorology*.

rainfall. Recent scientific studies have focused on optimizing these rainfall algorithms to improve the accuracy of rainfall measurements (Glitto and Choy 1997; Vieux and Bedient 1998; Anagnostou and Krajewski 1998, 1999a,b; Fulton 1999).

One way to improve the accuracy of radar derived rainfall estimates is to apply different Z-R relationships that take range dependency, precipitation type, and storm type into account (Shelton-Mur 1998). One of these variables, precipitation type, is based on the different microphysical processes that are dominant in convective versus stratiform clouds (Houghton 1968; Houze 1993; Biggerstaff and Listemaa 2000). Biggerstaff and Houze (1991) noted that convective and stratiform regions exhibit different distributions of the mean vertical wind field. These variations contribute to differences in cloud growth mechanisms and in drop size distributions within the clouds (Houghton 1968; Tokay and Short 1996). The radar reflectivity factor depends on both the number and size of the cloud particles (Doviak and Zrnic 1993). Variations in drop size distributions result in variations in reflectivity and therefore bring about different Z-R relationships (Rinehart 1997). Because of theses differences, separate Z-R relationships must be applied within these regions in order to better account for the precipitation type (Atlas et al. 1999). Unfortunately, a typical rainfall-estimating algorithm, such as that used in the WSR-88D (Fulton et al. 1998) uses only one Z-R relationship within the given volume of data. This can lead to rainfall estimates that are in considerable error (Steiner and Houze 1993, 1997) and have a rather large impact on the performance of meteorological and hydrological models (Pereira et al. 1998).

Ideally, one would use vertical velocity to separate the convective and stratiform precipitation (Atlas et al. 2000). However, most weather radars do not directly collect information about the vertical velocity field, consequently, partitioning has to be done based on the characteristics of the radar reflectivity field.

Previous investigators found that convective and stratiform echoes exhibit distinct features in the reflectivity field. Convective precipitation is indicated by high horizontal reflectivity gradients and high rain rates while regions of stratiform precipitation are identified by low reflectivity gradients and low rain rates (Churchill and Houze 1984). These basic observations formed the early beginnings of echo classification algorithms.

Within the last decade, several echo classification algorithms have been introduced. One of these algorithms, developed by Steiner et al. (1995), is currently being used in the Tropical Rainfall Measuring Mission (TRMM) for both observational and ground validation purposes (Marks et al. 1999; Kummerow et al., 2000; Schumacher and Houze, 2000). Recently, Biggerstaff and Listemaa (2000; hereafter referred to as BL) introduced a refined version of the Steiner et al. algorithm (1995; hereafter referred to as SHY). Preliminary tests conducted on both algorithms indicate that there is a 14% difference in the rain estimates that result from the echo classification.

One of the fundamental goals of TRMM is to obtain accurate heating profiles in the tropics to validate large-scale atmospheric circulation models (Simpson et al. 1988; Tao et al. 1993; Kummerow et al. 1998). To accomplish this goal, rainfall estimates

need to be within 10% error (Tao et al. 1993, Adler et al. 2000). Improvements to the echo classification process are needed to improve rainfall estimates.

To determine whether the modifications made by BL are improvements, there is a need to validate the echo classification scheme. The purpose of this project is to validate the BL algorithm in a manner consistent with the physical definitions of convective and stratiform rain.

CHAPTER II

PREVIOUS ECHO CLASSIFICATION TECHNIQUES

The utility of an algorithm that discriminates convective from stratiform precipitation is evident by noting the numerous techniques that have been developed for use with various meteorological observing platforms in use today. For example, Johnson and Hamilton (1988) developed one such algorithm for use on rainfall measurements obtained from rain gauge networks. Other schemes process data obtained from meteorological satellites (Adler and Negri, 1988; Kummerow et al. 1991; Hong et al. 1999). Likewise, separation strategies have been developed for use with wind profiler and disdrometer data (Williams et al. 1995; Tokay and Short 1996; Tokay et al. 1999) and radar reflectivity data (Churchill and Houze 1984; Rosenfeld et al. 1995a,b; Steiner et al. 1995; Biggerstaff and Listemaa 2000).

The concept of using radar reflectivity data to partition storm systems into convective and stratiform regions is based on the efforts of Battan (1973) and Houze (1973). However, it wasn't until 1984 when the first automated echo classification scheme was introduced (Churchill and Houze 1984) that partitioned reflectivity data based on derived rain rates. The reflectivity data were converted to rain rates and then partitioned by applying a set of test conditions, including a test for convective peaks and a test based on an absolute convective threshold (20 mm h^{-1}). Rain rates exceeding this threshold were immediately labeled as convective. Convective peaks were located by

comparing the maximum reflectivity to the average of the background rain rates. If a peak exceeded the average by a factor of two then it was labeled as convective. Once the centers of convection are located, a windowing technique was applied so that points within a designated radius were labeled convective as well.

This algorithm led to the development of the Steiner and Houze (1993) scheme, which adapted the Churchill-Houze method to use radar reflectivity instead of the reflectivity-derived rain rates. Later, Steiner et al. (1995) made further improvements to the algorithm by modifying the test conditions. They implemented the use of an intensity dependent threshold for locating the convective peaks and comparing them to the average background reflectivity. Those investigators also modified the convective window so that the size of the window used to identify any surrounding convective points was based on an intensity dependent radius. All remaining non-zero reflectivity points were classified as stratiform. According to the investigators, tests showed that this algorithm was somewhat limited since it incorrectly classified the high reflectivity values associated with the radar bright band as convective when it should have been labeled as stratiform. It was also found that this algorithm was inadequate when attempting to classify radar reflectivity echoes that are less than 20 km^2 in diameter.

CHAPTER III

THE BIGGERSTAFF-LISTEMAA ALGORITHM

The algorithms presented above are generally two-dimensional. That is, only the horizontal characteristics of the reflectivity field for a single level, the working level, are examined in order to partition the entire volume of radar data. Furthermore, the successful use of these algorithms is limited to regions that do not suffer from bright band contamination. Biggerstaff and Listemaa (2000) introduced an algorithm that is based on the SHY95 algorithm but uses the full three-dimensional volume of radar reflectivity. In the BL scheme, the SHY95 algorithm serves as a first guess convective-stratiform map where each point is evaluated by using a series of tests to determine if a different classification should be assigned. The series of tests uses four additional parameters so that the vertical characteristics of the reflectivity data are considered when determining the appropriate echo classification.

One parameter is the reflectivity value found 3 km above the height of the maximum reflectivity within the grid column. Stratiform precipitation will have lower reflectivity values aloft due the presence of ice crystals. Convective regions on the other hand may have higher values because more liquid water is found aloft due to the presence of strong vertical updrafts (DeMott and Rutledge 1995, 1998). Reflectivity values aloft that are greater (less) than 28 dBZ are generally associated with convective (stratiform).

Another parameter is the vertical reflectivity lapse rate, defined as the decrease in reflectivity with increasing height above the ground. It is calculated for the 3 km layer above the height of the maximum reflectivity to account for areas of weak convection as well as variations in the height of the melting level that can be observed from storm to storm and season to season. Lapse rates less (greater) than 3.5 dB km^{-1} are generally considered to be associated with convective (stratiform) precipitation.

To account for high reflectivity values associated with the bright band, a modified bright band fraction (BBF) is calculated (Rosenfeld et al. 1995a,b) and included in the tests used to determine if reclassification is required. The modified BBF is the fraction of the echo area that has maximum vertical reflectivity values located within ±1.5 km of the freezing level and stratiform vertical reflectivity lapse rates in the layer above the melting level. Including the lapse rate in the BBF calculation reduces the number of grid points that are incorrectly classified as stratiform due to convection having a maximum reflectivity near the melting level (Biggerstaff and Listemaa, 2000).

Finally, the magnitude of the two-dimensional horizontal reflectivity gradient is computed for each grid point. This is done using the log-scale reflectivity (dBZ) in a manner similar as Rosenfeld et al (1995a) but modified for a Cartesian coordinate system. Gradient values that are greater (less) than 3.0 dB km^{-1} are considered to be indicative of convective (stratiform) precipitation.

Together, these parameters are used to adjust the SHY95 first guess convective-stratiform map by reclassifying points when certain conditions are met. A point

originally classified as convective by the SHY95 algorithm is reclassified as stratiform if either of the following two conditions are satisfied:

1) The grid point has a weak horizontal reflectivity gradient, high vertical reflectivity lapse rate, and a low reflectivity value at the working level

2) The grid point has low reflectivity aloft, weak horizontal reflectivity gradient, and a high BBF

Likewise, a point that was originally classified as stratiform by the SHY95 algorithm is reclassified as convective if either of the following conditions is satisfied:

1) The grid point has a strong horizontal reflectivity gradient

2) The grid point has a weaker horizontal reflectivity gradient and a low BBF

When the above conditions are not satisfied, then the classification originally assigned to the point in the first guess field is retained.

After this adjustment is made, one final test is conducted in order to "smooth" the analysis. For each grid point, the algorithm determines the fraction of non-zero points within a 17 X 17 point window (9 km X 9 km) that has a classification different from the grid point in question. If the fraction is greater than 0.55, then the grid point is reclassified, otherwise no change is made to the adjusted convective-stratiform map. The result is the final version of the convective-stratiform map where each point, representing a grid column within the volume of radar data, is assigned a numerical value of either a "0", a "1", or a "2". A value of "0" indicates no echo to classify, a value of "1" indicates a stratiform point, and a value of "2" indicates a convective point.

CHAPTER IV

ALGORITHM PERFORMANCE

As mentioned previously, the developers of the SHY95 algorithm indicated that the algorithm has difficulty in classifying regions that contain the bright band. Comparison tests conducted on both the SHY95 and the BL algorithms reveal that the SHY95 algorithm has several other shortfalls as well (Biggerstaff and Listemaa 2000).

Both algorithms were used to partition the reflectivity field associated with a squall line (Houze et al. 1990). It was found that the SHY95 incorrectly identifies the leading edge of squall lines as stratiform precipitation when they should be classified as convective. It was suggested that increasing the intensity-dependent convective radius could minimize this problem. However, Biggerstaff and Listemaa showed that doing so resulted in other regions of the squall line being incorrectly classified as convective.

Another region where the SHY95 had difficulty was in classifying isolated cores of convection that often appear ahead of a squall line system (Biggerstaff and Listemaa 2000). Once again, the SHY95 labels the edges of these cores as stratiform. This too could be fixed by increasing the convective radius. Such a solution would be viable for isolated cores but not on a larger more developed system such as a squall line system.

The transition zone and the trailing stratiform regions were other portions of a squall line system where the SHY95 had difficulty in partitioning the radar echo. The SHY95 algorithm classified high reflectivity areas in the trailing stratiform anvil region

as convective. This gives the appearance of embedded convection when these regions are more likely a reflection of the bright band and should therefore be classified as stratiform. The transition zone on the other hand is classified as stratiform by the SHY95 algorithm. The investigators argue that based on studies by Biggerstaff and Houze (1993), a convective classification would be more appropriate because the precipitation found in this region actually develops in the regions of strong vertical updrafts.

One area where the BL algorithm incorrectly classified radar echoes is in regions that contain thin lines of convection that are surrounded by large regions of stratiform precipitation. In this type of case, the thin lines of convection are classified as stratiform. This is a result of the smoothing window that is applied. Biggerstaff and Listemaa point out that this may only be important in geographical regions where the environmental low-level wind shear is typically small enough to support narrow convective lines. In such low shear regions it may be more appropriate to decrease the window size used in the smoothing step.

CHAPTER V

DATA

Data Description

The data used in this study consists of radar reflectivity and velocity data collected during a local field project conducted by the Mesoscale Research Group under the Department of Meteorology at Texas A&M University. The group collected the data during the Texas A&M Convection and Lightning (TEXACAL) field experiment conducted from 1 May through 30 Jun 1997 in collaboration with the National Aeronautical Space Administration (NASA), the National Weather Service (NWS), and the National Severe Storms Laboratory (NSSL) (Biggerstaff et al. 1997; Tuttle and Biggerstaff 1997). This experiment involved the use of two strategically placed Doppler weather radars, the Texas A&M Aggie Doppler radar (ADRAD) and the NOAA/NASA Tropical Oceans-Global Atmosphere (TOGA) Doppler radar. The ADRAD (TOGA) transmits a vertically (horizontally) polarized linear beam that has a half-power beam width of 1.52° (1.65°) and a wavelength of 10.56 cm (5.33 cm). The ADRAD is permanently positioned on top of the Eller Oceanography and Meteorology building located on the campus of Texas A&M University, College Station, TX (30°37'04''N 96°20'12''W). The TOGA radar was positioned at 30°18'00''N 96°32'29''W giving way to a 40 km baseline between the two radars (Fig. 1). The radars were configured so

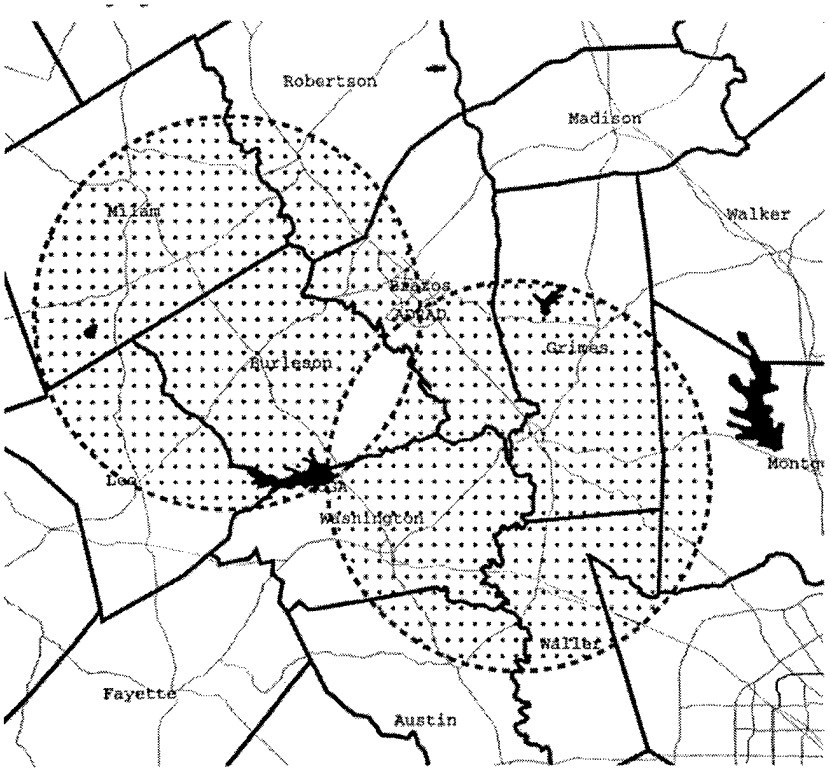

Fig. 1. A map of the TEXACAL dual-Doppler network over southeast Texas. The circular region with dots represents the effective domain of the network.

Table 1. Listing of the volume scan times used in this study. Each column represents one day with the date given in the top row. Remaining rows indicate scan start times.

970523	**970524**	**970617**
2051	1853	1228
2102	1930	1239
2113	2013	1250
2124	2034	1301
2135	2058	1312
2147	2112	1323
2158	2123	1334
2209	2155	
	2211	
	2224	
All scan times are UTC		

that the volume collection times were relatively the same. Table 1 lists the volume scan times used in this study.

Data Preparation

The first step in preparing the data for use required that it be inspected and edited to assure its quality. The data were inspected and meticulously edited with the aid of an interactive radar editing software package known as the Research Data Support System (RDSS) software (Oye and Carbone 1981). During the editing phase, reflectivity data were deleted from the volume that can occur due to anomalous propagation. Returns that result from non-meteorological targets, such as buildings, were also removed in addition to reflectivity returns that result from range aliasing (second trip echoes). The velocity field was edited to correct regions experiencing velocity aliasing by "unfolding" the data using a higher Nyquest interval (Rinehart 1997).

The edited volumes of data from both radars were then interpolated to a Cartesian coordinate system. Radar data are usually stored using the spherical coordinate system (azimuth, elevation, and range). With the aid of the "Sorted Position Radar Interpolation" (SPRINT) software (Mohr et al. 1979), the radar data were interpolated to a user defined Cartesian grid (x, y, and z) using a bilinear interpolation scheme. The SPRINT software reads in the raw radar data and produces a binary output file of the transformed data, leaving the original data unaltered. These output files were then used for further processing.

After the coordinate transformation was completed, the dual-Doppler synthesis was performed for each volume time by using the "Custom Editing and Display of Reduced Information in Cartesian space" (CEDRIC) software package (Mohr and Miller 1983). This software package was specifically designed to facilitate in deriving the three-dimensional wind field by using the radial velocity data collected by two or more Doppler radars. The main goal in this step was to derive the vertical velocity field in a similar manner as Biggerstaff and Houze (1991). First, radial velocities from both radars were combined to make an estimated horizontal velocity field. Next, particle fall speeds were removed from the estimated wind field and the vertical velocity field was determined from the anelastic continuity equation after calculating the divergence field. The vertical velocity field was used to determine a new estimate of the horizontal winds. The divergence was once again calculated and a new vertical velocity field was calculated. This procedure was repeated until the mean of the absolute value of the change in the horizontal wind between iterations was less than 0.1 ms^{-1}. The CEDRIC software was also used to create a single reflectivity field by taking the maximum of the two-reflectivity values at each grid point. The echo classification was performed using this single reflectivity field. Validation of the echo classification was based on the derived vertical velocity field.

CHAPTER VI

METHOD OF ANALYSIS AND VALIDATION

The algorithm used to perform the echo classification is written in the C programming language. It reads in binary CEDRIC output files and produces ASCII text files containing the results of the SHY95 and the BL algorithms. The text files also contain the values of the parameters used during the classification as well as information identifying the points that were classified differently by the two algorithms. Interactive Data Language (IDL) programs were used to produce digital displays of the convective-stratiform maps and the reflectivity fields for each volume scan. By comparing these displays (DeMott et al. 1995), one can make a visual estimate of the performance of the techniques. However, due to the subjective nature of visual inspections, alternate methods were used to judge the validity of the algorithm.

After analyzing reflectivity plots and the convective-stratiform maps, vertical profiles of the mean vertical velocity and reflectivity were examined for each volume scan. The mean reflectivity profiles were derived by first converting the logarithmic values to linear values. Then the average of the linear values was computed and then converted back logarithmic values. These profiles were generated separately for the convective regions and the stratiform regions and then compared to similar types of profiles shown in studies such as those by Gamache and Houze (1982), Houze (1989), and Biggerstaff and Houze (1991). These studies show that convective and stratiform

vertical velocity profiles have distinct differences that are easy to identify (Fig. 2). With this in mind, close attention was given to the profiles that were generated based strictly on the points where differences in echo classification occurred between the two algorithms. It was anticipated that these points would help determine the overall improvement gained by using one technique over the other.

To supplement the information gained from the vertical profiles, the frequency distributions of the reflectivity and vertical velocity fields were also examined for each volume scan by using contoured frequency by altitude diagrams (CFADs) as shown in Fig. 3c. Yuter and Houze (1995a) demonstrated the usefulness of such diagrams in diagnosing the kinematic and microphysical evolution of storms in Florida.

According to Yuter and Houze, a CFAD is a diagram where contours of frequency are plotted in a coordinate system where the ordinate is the height and the abscissa contains the parameter whose distribution is being examined. It is generated by using a subset of the data points within the entire volume of radar data. First, normalized histograms (such as shown in Fig. 3a) of the parameter under study are created for each altitude that contains more than 10% of the data points found in the volume. These histograms are then placed one behind the other, resembling the peak of a mountain (Fig. 3b). The actual CFAD is then created by drawing contours of frequency (representing the percentage of data points per unit variable per unit height) for this ensemble of histograms, just as one would draw height contours to create a topographic map of a mountain. A single CFAD diagram can provide the same

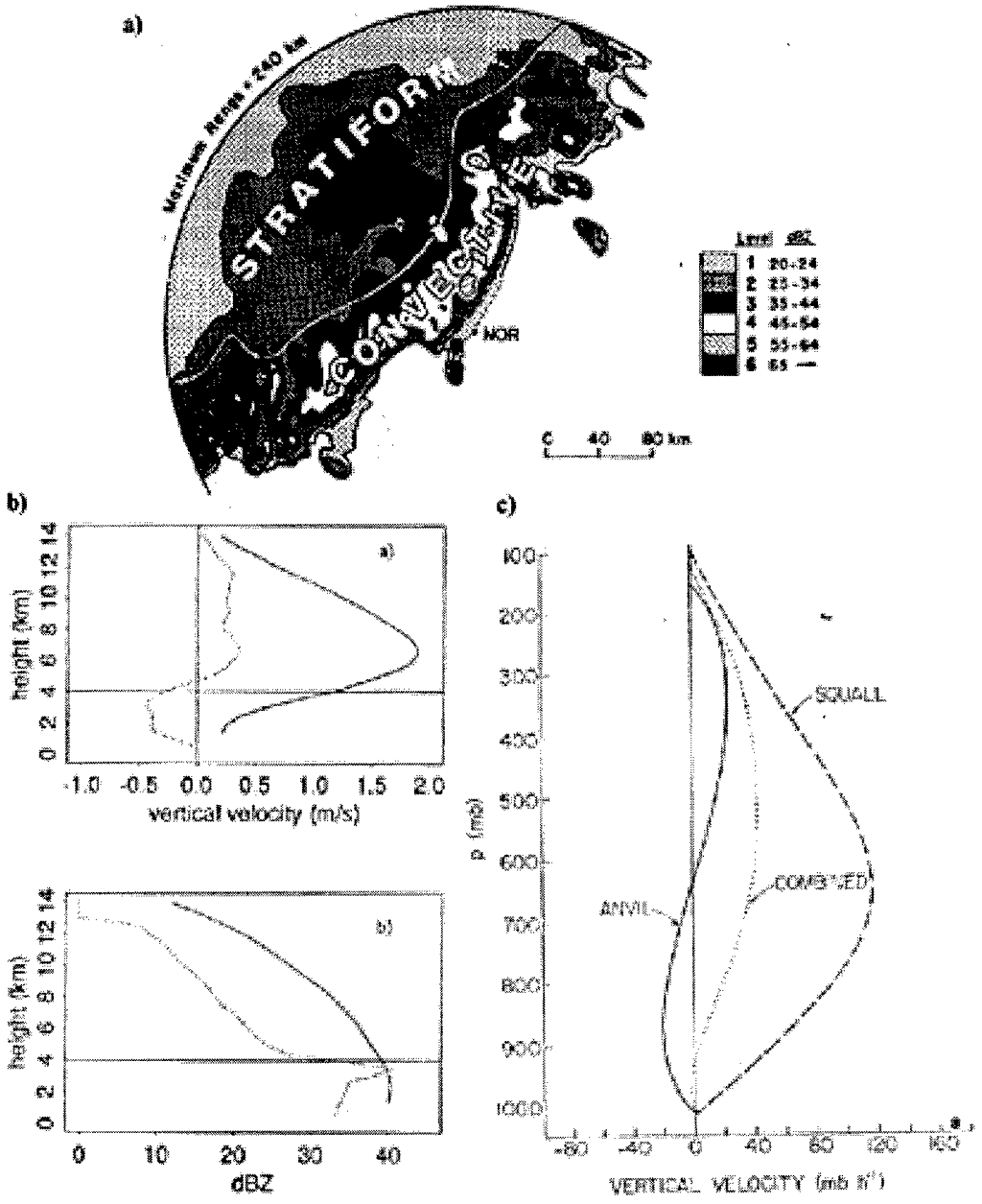

Fig. 2. (a) Example of a partitioned radar reflectivity field. Shaded values indicate reflectivity levels (dBZ) (after Houze et al. 1990). (b) Characteristic mean profiles of reflectivity (top) and vertical velocity (bottom) for convective (solid lines) and stratiform (dashed lines). Horizontal line at 4 km indicates freezing level (after Yuter and Houze 1995b). (c) Representative mean vertical profile for a squall line with a trailing stratiform region. Solid line is profile for the convective squall line. Dashed line represents profile for the stratiform anvil (from Gamache and Houze 1982).

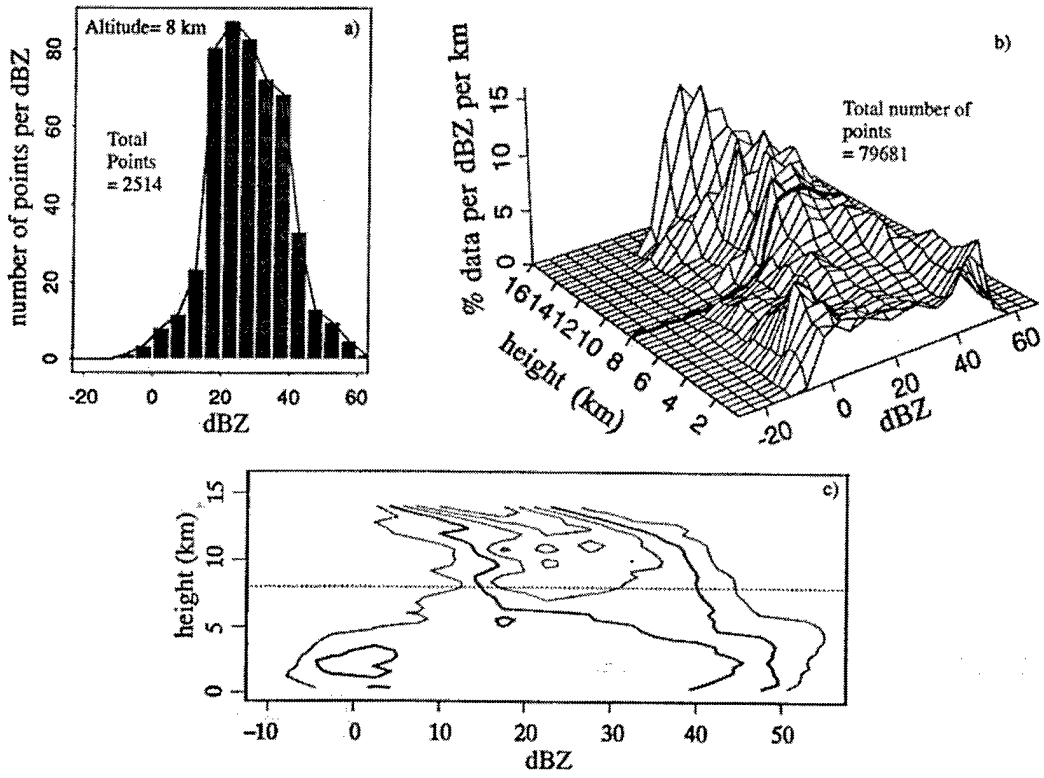

Fig. 3. The development of the reflectivity contoured frequency by altitude diagram. First, single level histograms like that shown in (a) are created for each altitude of data using a bin size of 5 dBZ. The histograms are then stacked one behind the other as shown in (b). The heavy line corresponds to the histogram shown in (a). Selected contours are then drawn as shown in (c) to create the CFAD. In (c), the heavy line represents the 5% dBZ^{-1} km^{-1}. CFADs are often truncated to include only the altitudes that have more 10% of the total data points in the volume (adapted from Yuter and Houze 1995b).

information that would normally require as many as 20 histograms. The CFAD offers insight into the width of the frequency distribution, the mode of the distribution, the skewness and the peakedness of the data. A narrow frequency distribution is seen when the contours are spaced closely together while loosely packed contours indicate a much wider distribution.

When evaluating CFADs, Yuter and Houze made a comparison of the spatial patterns of the contours between levels within a single volume. They also compared the spatial patterns of CFADs from successive volumes by overlaying contours from two or more CFADs to assist in determining storm evolution. The investigators found that during the early and more convective stages of evolution, the reflectivity CFAD exhibits a fairly wide frequency distribution at most levels (Figs. 4a,c,e) and may also be multimodal. During the later stages where more stratiform precipitation is found, the investigators found that the reflectivity frequency distribution narrows and often becomes unimodal at all levels (Figs. 4g,i). In addition, the contours undergo a decrease in slope and become more diagonal, indicating a fairly uniform distribution at each level and a decrease in the reflectivity with increasing height.

Steiner et al. (1995) and DeMott et al. (1998) showed that the CFAD could be useful in determining the validity of radar echo classification algorithms. The investigators validated their algorithms by creating separate CFADs of reflectivity and vertical velocity for the convective and stratiform regions and then comparing the spatial patterns of the frequency distribution contours. The algorithms were found to be

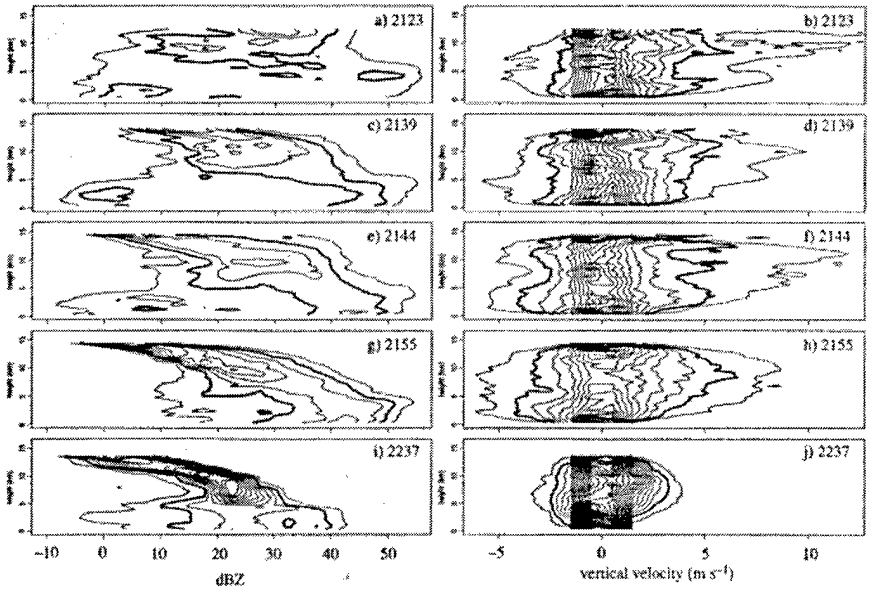

Fig. 4. An example of a time series of CFADs of radar reflectivity (left) and vertical velocity frequency (right) used to study Florida cumulonimbus (from Yuter and Houze 1995a). In this example, the CFADs are generated using the entire volume of data. In this study, this procedure is used to create separate stratiform and convective CFADs based only on those points classified as convective or stratiform.

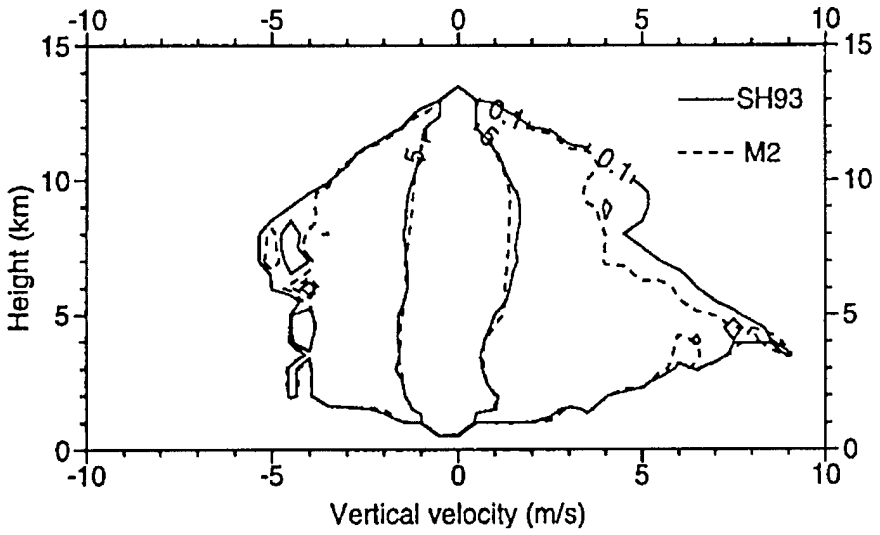

Fig. 5. An example of overlaying selected contours from two separate CFADs. In this case, the 0.1% and the 0.5% velocity frequency contours are displayed based on the Steiner and Houze 93 echo classification algorithm and a modified algorithm (from DeMott et al. 1998).

Successful in identifying stratiform regions since the stratiform CFADs displayed narrow frequency distribution and diagonal frequency contours. Likewise, the algorithms were successful in identifying convective regions since the convective CFADs indicated a wide frequency distribution.

In this study, CFADs were used in a manner similar to that used in the SHY95 validation study. Convective and stratiform CFADs were created using the output of both algorithms. Algorithm performance was checked by overlaying the 5% frequency contours from the CFADs of both algorithms onto a single plot as shown in Fig. 5. In general, an algorithm was considered as performing better than the other if the CFADs that were generated based on its classification displayed the narrowest (widest) distribution for stratiform (convective) regions. As an additional check, CFADs were created using only the points that were reclassified by the BL technique, one based on those points that went from convective to stratiform and the other based on the points that went from stratiform to convective. In the case of the points that went from convective to stratiform, the CFADs were evaluated to determine if the spatial patterns exhibit the stratiform characteristics of narrow distributions and uniformity at each level. Likewise, for the points that went from stratiform to convective, the CFADs were evaluated to determine if the frequency distributions were rather wide. If the appropriate signatures were observed in the correct CFADs, then it was concluded that the BL algorithm provided better echo classification results.

In addition to the mean vertical profiles and CFADs, plots of the distribution of the reflectivity lapse rate (defined as the change in reflectivity with increasing height) for

the 4 – 7 km layer were created and examined. The 4 – 7 km layer was chosen since it is the layer that best represents the mixed phase region (for this study the region where temperatures range from 0° C to –20° C). Like the mean profiles and CFADs, these plots were generated separately for the convective and stratiform regions. The convective and stratiform distributions that resulted from each of the algorithms were compared as well as the distribution of the lapse rates for the points that were classified differently by the two algorithms.

Once the mean profiles, CFADs, and lapse rate distributions were examined for each individual volume, multiple volumes for each case were combined and processed such that individual volume scans representing the developing stage of a precipitation system were combined together while those representing the mature stage were combined together. A new set of profiles, CFADs, and lapse rate distributions were created and analyzed based on these combined volumes.

CHAPTER VII

RESULTS AND DISCUSSION

Both the BL and the SHY95 algorithms were used to partition radar reflectivity data collected for three different precipitation systems that occurred within the dual-Doppler domain. The first case involves precipitation resulting from the interaction of a northward moving squall line and an eastward moving band. The second case is precipitation associated with an asymmetric squall line. Both of these cases are precipitation systems that consist of a mixture of convective and stratiform precipitation. It was of interest to determine how the algorithms perform on systems where the precipitation is predominately convective. To determine this, a bow echo system was used as the third case.

Algorithm Adaptable Parameters

The echo classification algorithm has many parameters that can be changed depending on geographical location and the type and physical location of the radar in use. During this validation study, all of the parameters were set to the same values as found in Biggerstaff and Listemaa (2000) with the exception of the working level range threshold. Biggerstaff and Listemaa followed Steiner et al. (1995) and used a split working level defined such that for distances up to 100 km from the radar, reflectivity values from the 1.5 km altitude were used while values from the 3.0 km altitude were

used for distances beyond 100 km. The 100 km range was used because at this distance, the center of the radar beam at the lowest elevation angle is 1.5 km above the ground. For this study, echo classification was completed with respect to the ADRAD, which has a wider beam and a greater minimum elevation angle. With the ADRAD, the beam center for the lower elevation angle intersects the 1.5 km altitude at a range of about 80 km. Therefore the range threshold was decreased from 100 km to 80 km.

In addition to changing the working level range threshold, it was also necessary to modify the method used to determine the horizontal reflectivity gradient. In the original version of the algorithm, the horizontal reflectivity gradient is determined using the three point centered difference method. This method was sufficient for the data used in the Biggerstaff-Listemaa study since echo classification was performed within the entire domain of the radar.

In this study, echo classification is limited to a subsection of the domain due to the boundaries of the dual-Doppler network. Before computing the horizontal reflectivity gradients at each grid point, a check is performed to determine how many of the four points surrounding the grid point contains a valid reflectivity measurement. If all four points contain valid data, then the three point centered difference method is used to determine the reflectivity gradient. If one, two, or three of the surrounding points contain valid data, then the two-point method is used to calculate the gradient. A gradient is not computed for a grid point if none of the surrounding points contain valid data.

Case 1: Interacting Boundaries (970523)

a) Reflectivity Description

This case consisted of eight volume scans of data from 2051 UTC to 2209 UTC and the evolution of the system is depicted using the 3.1 km constant altitude plane position indicator (CAPPI) (Figs. 6 and 7). At 2051UTC (Fig. 6a), there were two separate regions of precipitation, a curvilinear west to east oriented squall line moving north and an eastward moving band of convection that has a north-south orientation. Between 2102 UTC (Fig. 6b) and 2113 UTC (Fig. 6c), the two systems began to merge and by 2147 UTC (Fig. 7b) the embedded convective cells found in the southern region began to weaken while the northern cells become more organized. At 2209 UTC (Fig. 7d), the southern half of the system was mainly composed of a uniform reflectivity field of values in the 40-45 dBZ range while the stronger cells were found in the northern region and had reflectivity values in the 50-55 dBZ range.

b) BL and SHY95 Convective-Stratiform Maps

Figures 8 and 9 show the convective-stratiform maps for the two algorithms as well as maps of the working level reflectivity and differences in echo classification between the BL and SHY95. Throughout the life cycle of the event, most of the points that were reclassified by BL were points that were originally classified as stratiform by

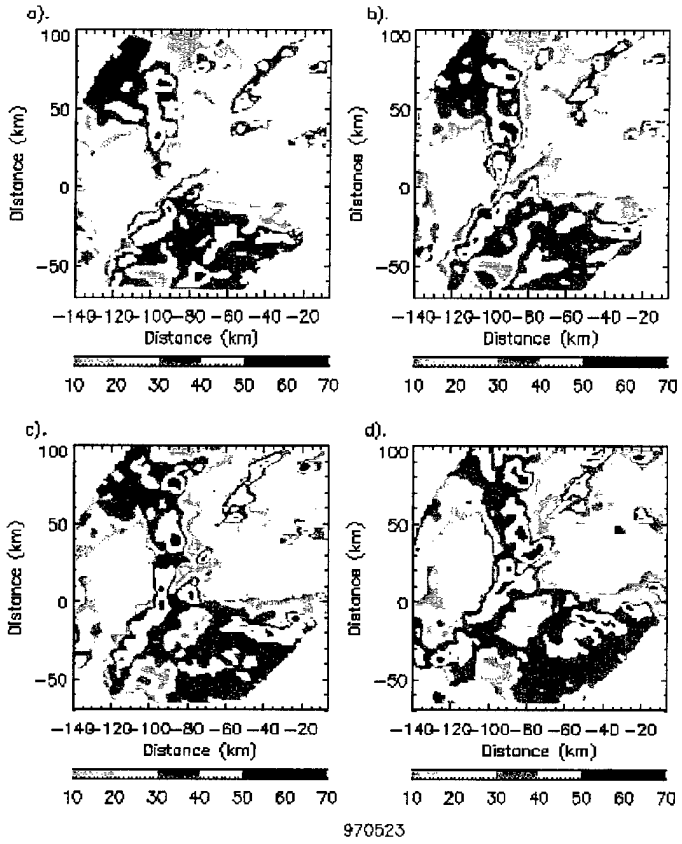

Fig. 6. Reflectivity for the 3.1 km altitude from the TOGA and ADRAD radars using the maximum reflectivity value measured by the two radars. Contours are every 10 dBZ starting at 10 dBZ. (a) 2051 UTC (b) 2102 UTC (c) 2113 UTC (d) 2124 UTC 23 May 1997.

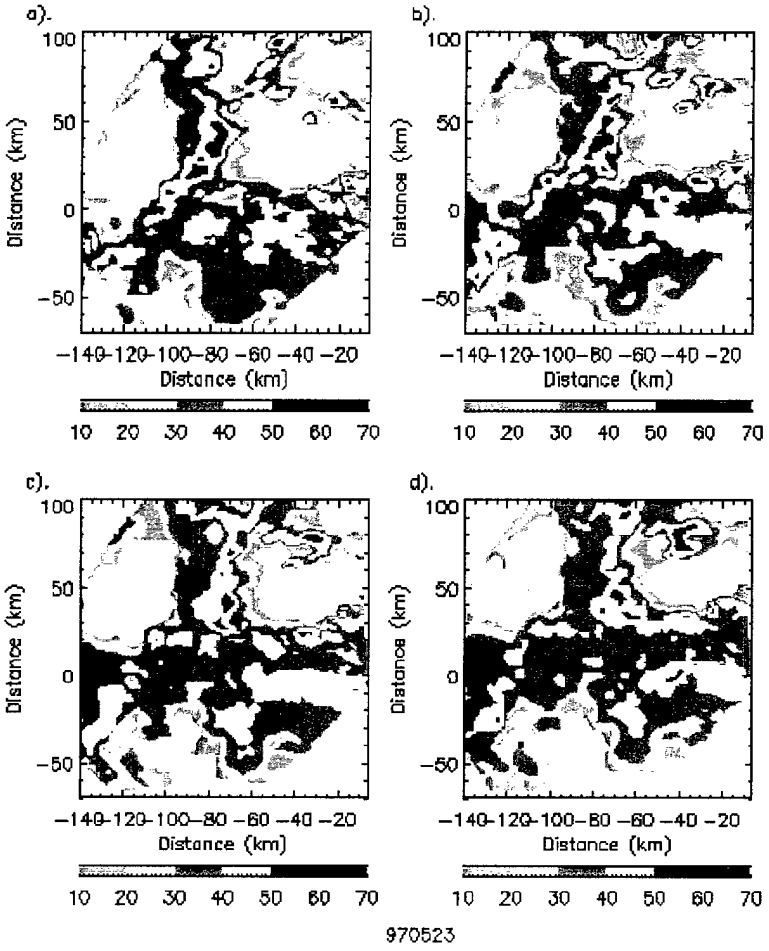

Fig. 7. Reflectivity for the 3.1 km altitude from the TOGA and ADRAD radars using the maximum reflectivity value measured by the two radars. Contours are every 10 dBZ starting at 10 dBZ. (a) 2135 UTC (b) 2147 UTC (c) 2158 UTC (d) 2209 UTC 23 May 1997.

SHY95. Indicated in Figs. 8b and 9b are the regions that changed classification from convective (stratiform) to stratiform (convective) based on BL. In these particular plots, one can see that the reclassified points are those that lie in close proximity to the 40 dBZ reflectivity contour. This particular result is a characteristic that is most prominent in the early stages of the system's development.

Occasionally, SHY95 also misidentified stratiform regions as isolated random cores of convection as seen in Fig. 9c. These isolated pixels are described as random since they appear in different regions of the system from one volume scan to the next and exhibit no time continuity as one would expect. BL correctly reclassifies most of these regions as stratiform.

In the previous section, it was noted that as the system evolved, the southern region of the system appeared to weaken. This observation can easily be inferred from the BL convective-stratiform maps (Figs. 10 and 11). At the beginning of the event, the BL algorithm classified most of the southern region as convective (Fig. 8d); with time, more and more of the southern region received the stratiform classification (Fig. 10d). This observation is not as readily apparent in the SHY95 maps until the very last volume scan (Fig. 11c). This is attributed to the fact that the BL algorithm was optimized for classifying regions containing high reflectivities that result due to the presence of the bright band, which is a feature often associated with stratiform precipitation. Despite this optimization of the algorithm, BL experiences some difficulty in properly identifying the back edge of the trailing stratiform region (located in the vicinity of -80, -

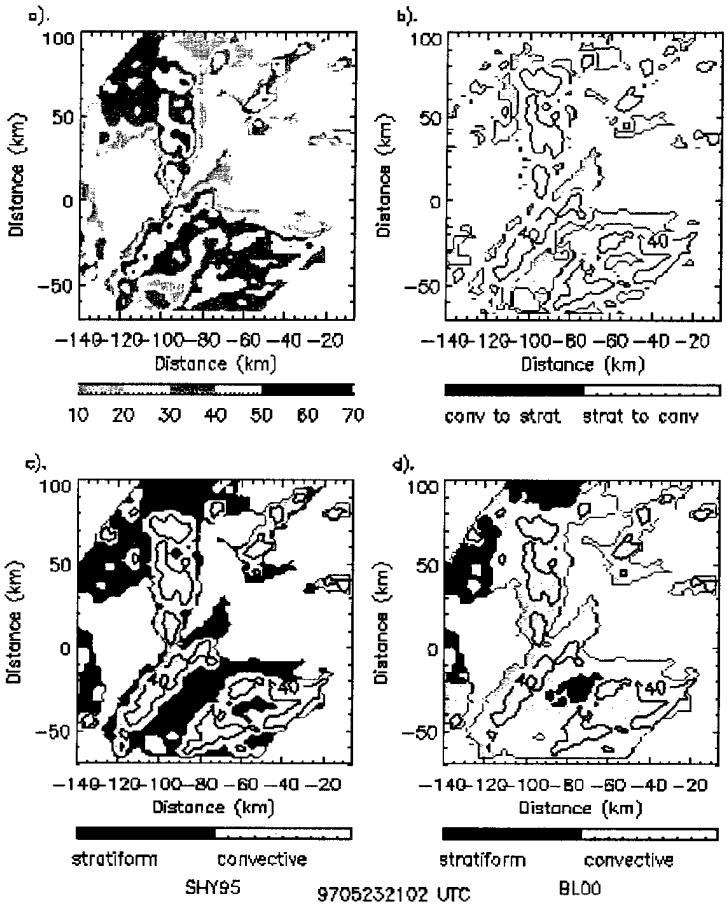

Fig. 8. (a) Reflectivity at the working level using the maximum reflectivity value recorded by the TOGA and ADRAD radars. Contours are every 10 dBZ starting at 10 dBZ. (b) Contour plot of the points BL reclassified. Darker (lighter) shading represents points that went from convective (stratiform) to stratiform (convective). No shading for the points that did not change. (c) Convective-stratiform map for SHY95 classification. Darker (lighter) shading represents stratiform (convective) regions. Also plotted is the 40 dBZ contour from the working level reflectivity. (d) Same as in (c) but for the BL classification. All plots are for 2102 UTC 23 May 1997.

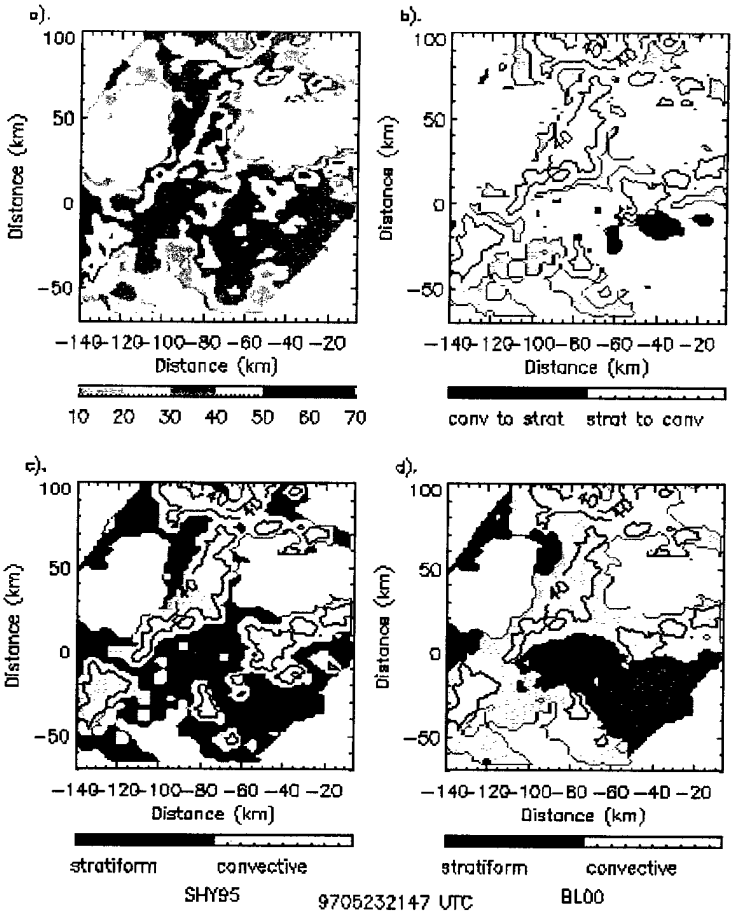

Fig. 9. As in Fig. 8 except for 2147 UTC.

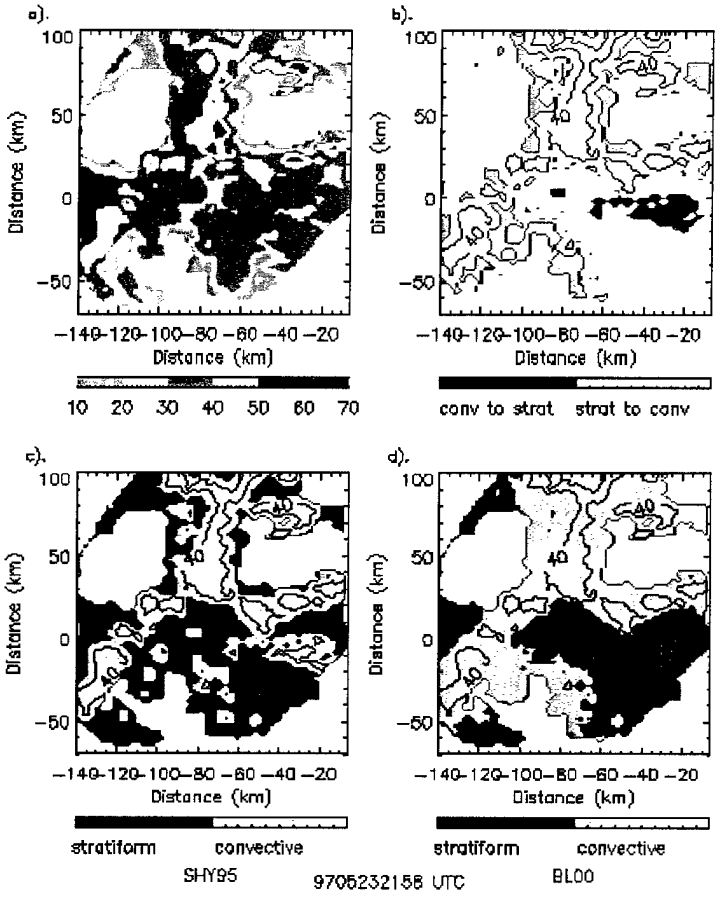

Fig. 10. As in Fig. 8 except for 2158 UTC.

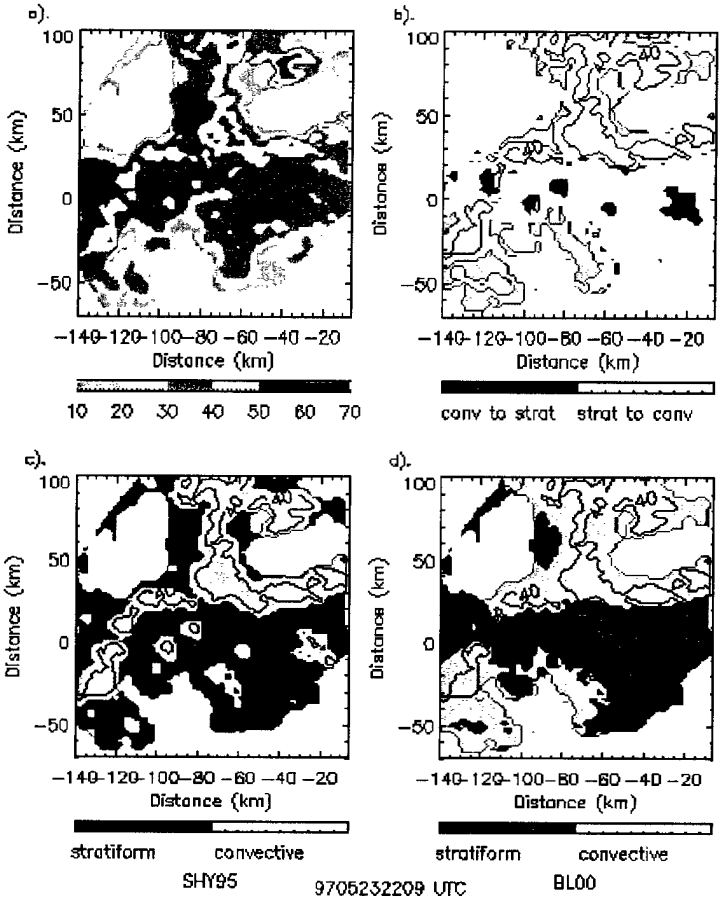

Fig. 11. As in Fig. 8 except for 2209 UTC.

30 in Figs. 9d, 10d, and 11d). This region should be classified as stratiform instead of convective.

c) Mean Reflectivity Profiles

Figure 12 shows vertical profiles of the mean reflectivity for the convective regions and the stratiform regions, as determined by both BL (solid) and SHY95 (dotted). The difference profiles (dash-dot; labeled as RCP) are also drawn and represent the points that were first classified as stratiform (convective) by SHY95 but were then reclassified as convective (stratiform) by BL.

A comparison of the convective profiles (Figs. 12a,b) reveal that the BL and the SHY95 curves have the same general shape where higher reflectivity values (> 40 dBZ) are found up to about 4 km and then decrease with increasing height. The BL curve also shows values that are slightly less than those indicated by the SHY95 curve for altitudes less than 4 km. Above 7 km, the reflectivity values are generally the same.

The convective difference curves (Figs. 12a,b) show the same general shape as the BL and SHY95 curves with higher mean reflectivity values found in the low levels. These difference profiles have means in the low levels that are about 10 dBZ smaller than in BL and SHY95 mean profiles. Above 4 km, the convective difference curve has a much steeper slope than the BL and SHY95 curves. A steeper slope aloft implies that higher reflectivities are found aloft which is indicative of the presence of larger ice particles in this region. Therefore, one can infer that the BL scheme properly changed the classification of these points from stratiform to convective.

Like the convective profiles, the stratiform reflectivity profiles (Figs. 12c,d) contain BL and SHY95 curves that have the same general shape but with subtle differences. The BL curve indicates slightly higher mean reflectivity values for altitudes

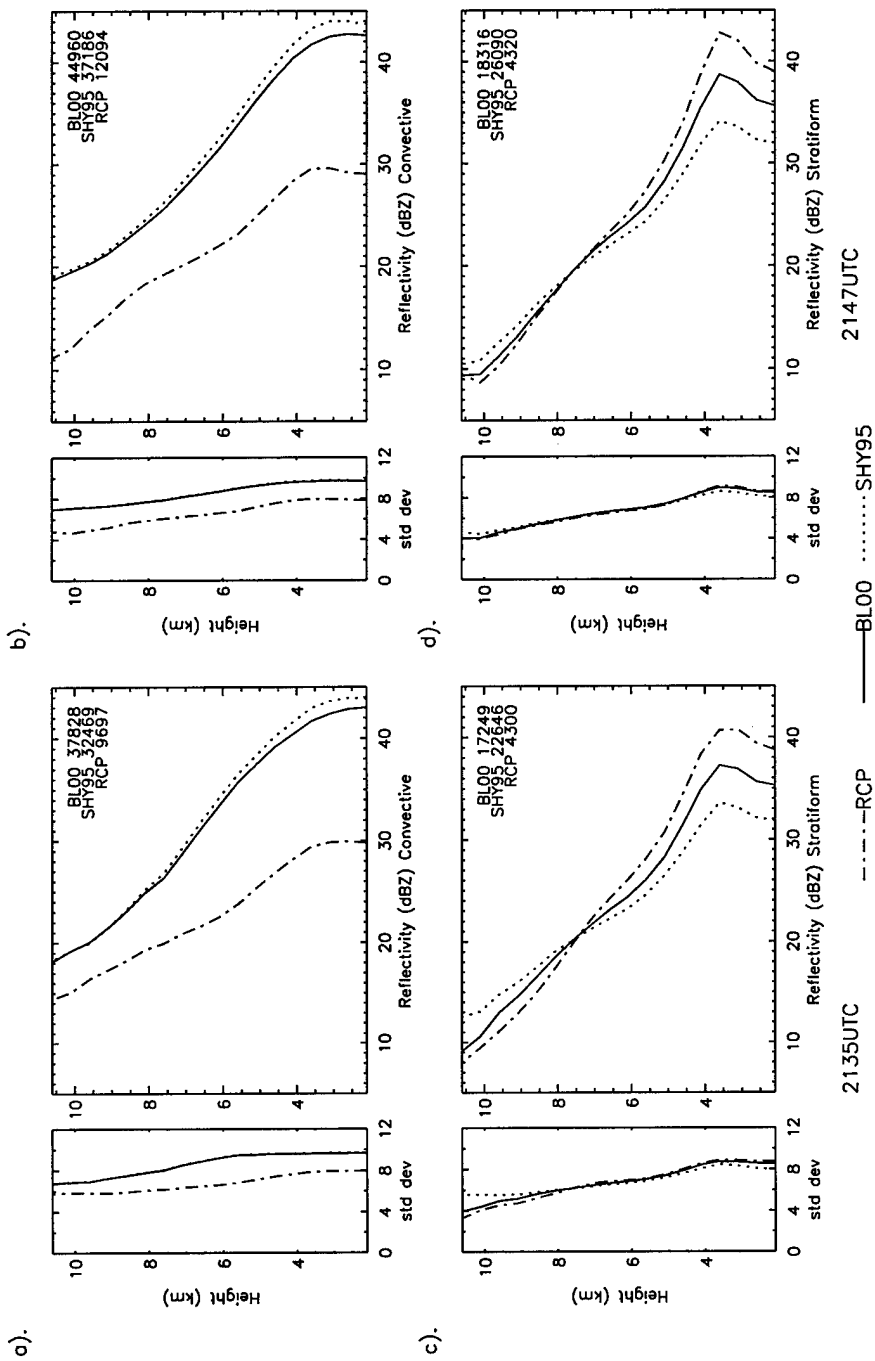

Fig. 12. Mean profiles of reflectivity and standard deviation of the reflectivity for the convective (top) and stratiform (bottom) regions for the 23 May 97 case. Solid line is profile based on the BL classification. Dotted line is profile for SHY95 classification. Dash-dot line is profile for the points BL reclassified. (a) and (c) is for 2135 UTC. (b) and (d) is for 2147 UTC. Also shown in the top right corner of profile plot is the number of points used to calculate the means.

below 7km and slightly lower mean reflectivities for those above 7 km. In addition, a peak in the mean reflectivity values is seen just below the melting level (~4 km) in both profiles but it is often more evident in the BL curves (Fig. 12d). This peak is a reflection of the higher reflectivity values that result due to the presence of melting ice, which is characteristic of stratiform precipitation.

Above the 7 km level, it can be seen that the BL curves indicates smaller mean reflectivity values than the SHY95 curve resulting in smaller slopes than in the SHY95 curves. This shows that the SHY95 technique classifies regions that have higher reflectivities aloft as stratiform when they should be classified as convective. This suggestion can further be verified by looking at the stratiform difference profiles (Figs. 12c,d). In these profiles, the mean reflectivity above the 7 km altitude is even less than that shown in the BL curves allowing for smaller slopes. This further suggests that BL correctly reclassified points as stratiform that were once considered as convective by SHY95. In addition, these difference profiles have higher mean peaks in the mean reflectivity just below the melting level leading to a more enhanced bright band signature just below the melting level. In fact, the peak mean reflectivity in the stratiform difference curve is as high as 10 dBZ higher than that in the SHY95 curve.

d) Mean Vertical Velocity Profiles

Shown in figures 13, 14, and 15 are mean vertical velocity profiles. For the convective regions (Figs. 13a,b), BL results in mean vertical velocities that are slightly smaller than those that result from SHY95. The points that changed from stratiform to

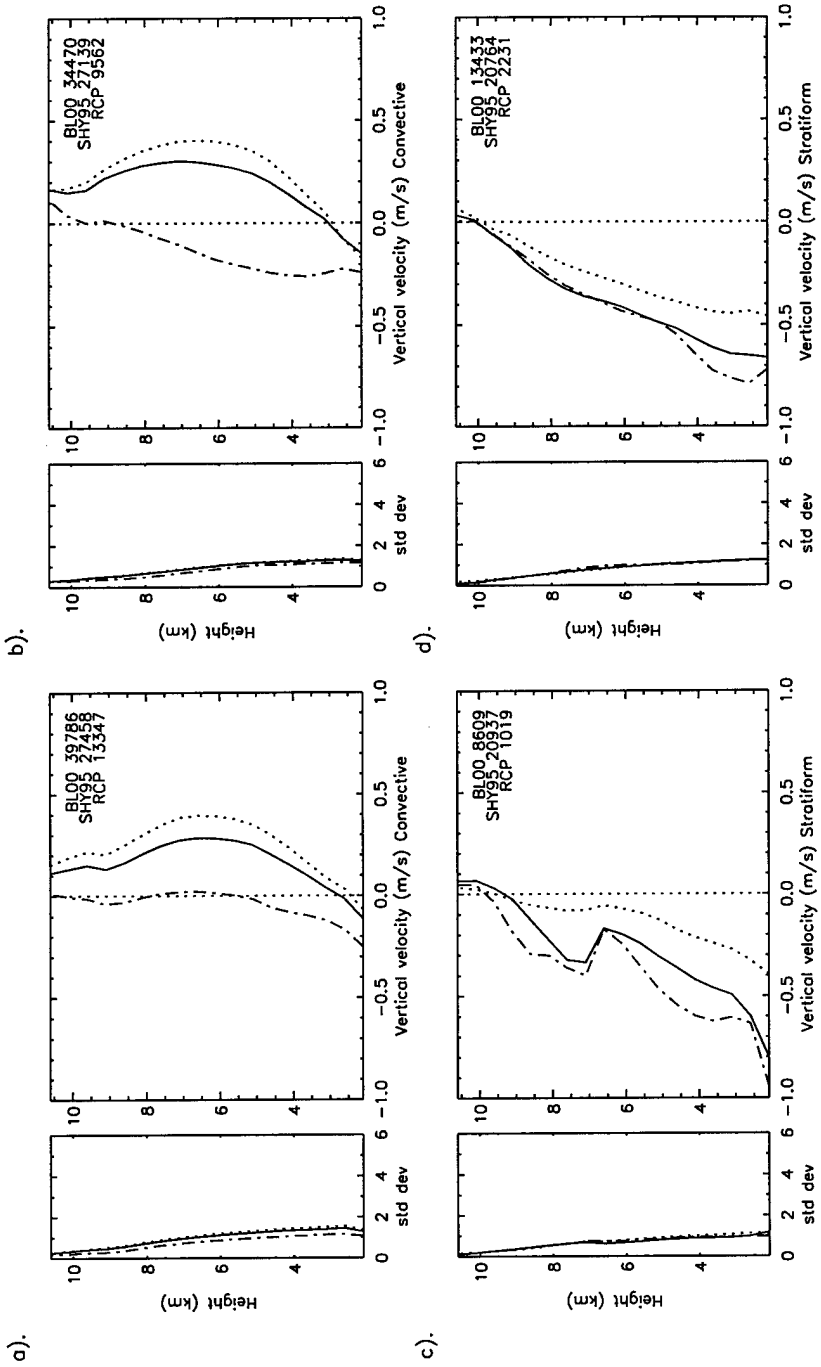

Fig. 13. Mean profiles of vertical velocity and standard deviation of the vertical velocity for the convective (top) and stratiform (bottom) regions for the 23 May 97 case. Solid line is profile based on the BL classification. Dotted line is profile for SHY95 classification. Dash-dot line is profile for the points BL reclassified. (a) and (c) is for 2113 UTC. (b) and (d) is for 2124 UTC. Also shown in the top right corner of profile plot is the number of points used to calculate the means.

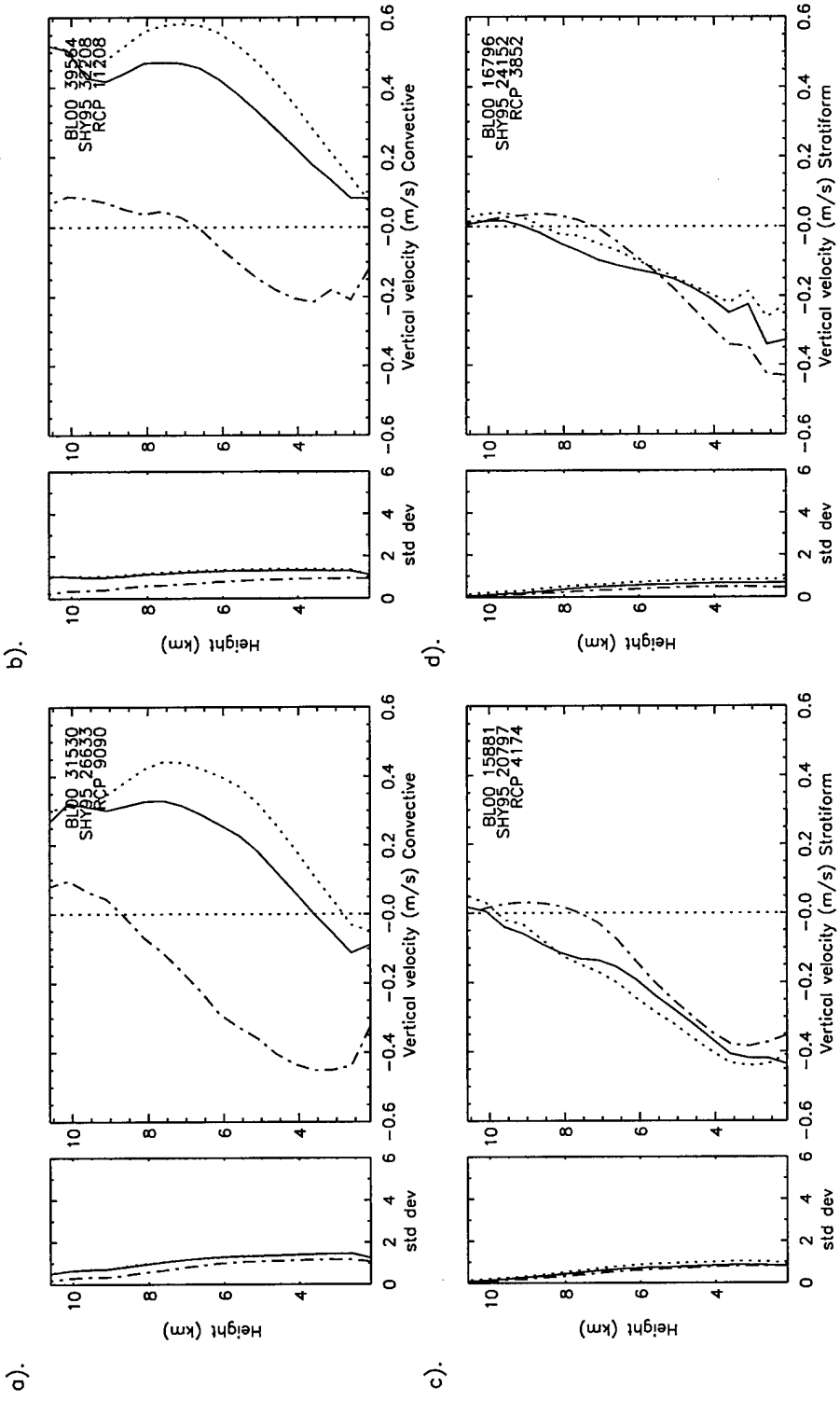

Fig. 14. Same as in Fig. 13 except for 2135 UTC and 2147 UTC.

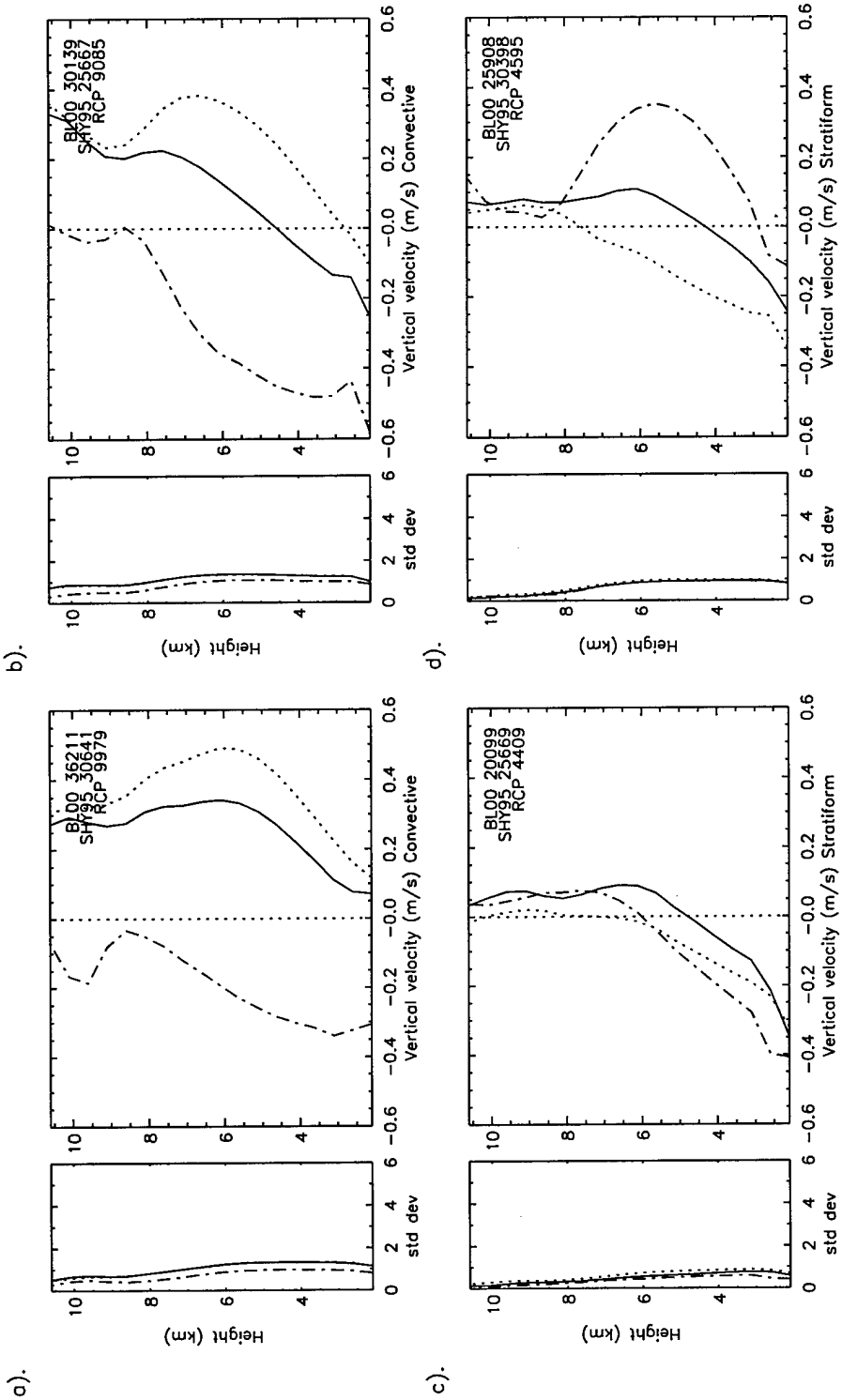

Fig. 15. Same as in Fig. 13 except for 2158 UTC and 2209 UTC.

convective contain weaker mean vertical velocities than that of BL and SHY95; this is especially true in the later stages of the system's evolution (Figs. 14a,b and 15a,b). Beginning at 2135 UTC (Fig. 14a), the reclassified points indicate stronger net subsidence below 8 km and either weak subsidence or positive vertical velocities above 8 km. Deep subsidence is often found in the forward anvil and transition zone regions of squall lines (Biggerstaff and Houze 1993). The mean vertical velocity profiles of the reclassified points are consistent with this type of structure. Given that much of the reclassified area was adjacent to high reflectivity bands, the vertical velocity profile is not surprising. Nevertheless, the mean vertical velocity profile over the stratiform region also exhibits subsidence, which suggests that the mesoscale updraft at mid-to-upper levels has not yet become established. Given the similarity between the reclassified convective points and the stratiform regions, it is not clear from the vertical velocity field that the reclassified convective points have been correctly adjusted. This discrepancy between reflectivity profiles and vertical velocity profiles was noted by Biggerstaff and Listemaa (2000). From the perspective of precipitation growth mechanisms, the BL00 result might be more appropriate than the SHY95 result. However, from the perspective of instantaneous divergence profiles, or cooling at low levels, the BL00 result suggests that the reclassified convective area might better be classified as stratiform.

For regions classified as stratiform, the BL mean vertical velocity profiles are once again generally weaker than the SHY95 profiles. At 2158 UTC (Fig. 15c) and 2209 UTC (Fig. 15d), the BL profiles are stronger than the SHY95 profiles below 8 km.

Both the BL and the SHY95 profiles indicate net subsidence below 8 km and upward vertical velocities above 8 km. This vertical velocity structure is likely over developing stratiform regions. The profiles that were generated based on the points that changed from convective to stratiform are, for the most part, weaker than the BL and SHY95 (Figs. 13c,d) profiles until 2135 UTC (Figs. 14c,d). Beginning at this time, the difference profiles indicate weak upward vertical velocities in the 6 – 9 km layer and stronger subsidence below. At 2209 UTC (Figs. 15c,d), the difference curve shows stronger upward mean vertical velocities throughout a larger layer with subsidence confined to the lowest levels, probably an indication of the ascending front to rear flow found in the trailing stratiform region, further evidence suggesting that BL properly reclassified these points.

e) Reflectivity CFADs

Shown in the reflectivity CFADs (Fig. 16) is the 5% contour from the BL (solid) and the SHY95 (dotted) CFADs. For the convective regions (Figs. 16a,b), the BL CFADs consistently show a wider reflectivity distribution than that shown by SHY95, especially for the altitudes below 7 km. For the stratiform regions (Figs. 16c,d), BL and SHY95 show narrower reflectivity distributions than seen in their convective counterparts. In comparing BL to SHY95 for stratiform regions, BL leads to a slightly narrower distribution in the low levels that is shifted a few dBZs to higher reflectivity values. More importantly though, the bright band signature is better seen in the BL distribution curve as a peak in the 5% contour located on the side of higher reflectivity

values. This is particularly more noticeable in the 2158 UTC CFAD. The more enhanced bright band signature further implies that better results can be obtained from BL.

The CFADs generated for the points that were reclassified by BL show wide reflectivity distributions with loosely packed frequency contours in the low levels for the points that were reclassified as convective (Figs. 17a,b). For the points that BL reclassified as stratiform, the CFADs show narrow distributions with frequency contours that are closely packed together (Figs. 17c,d). Furthermore, the stratiform CFADs show a pronounced peak in higher reflectivity values just below the melting level, an

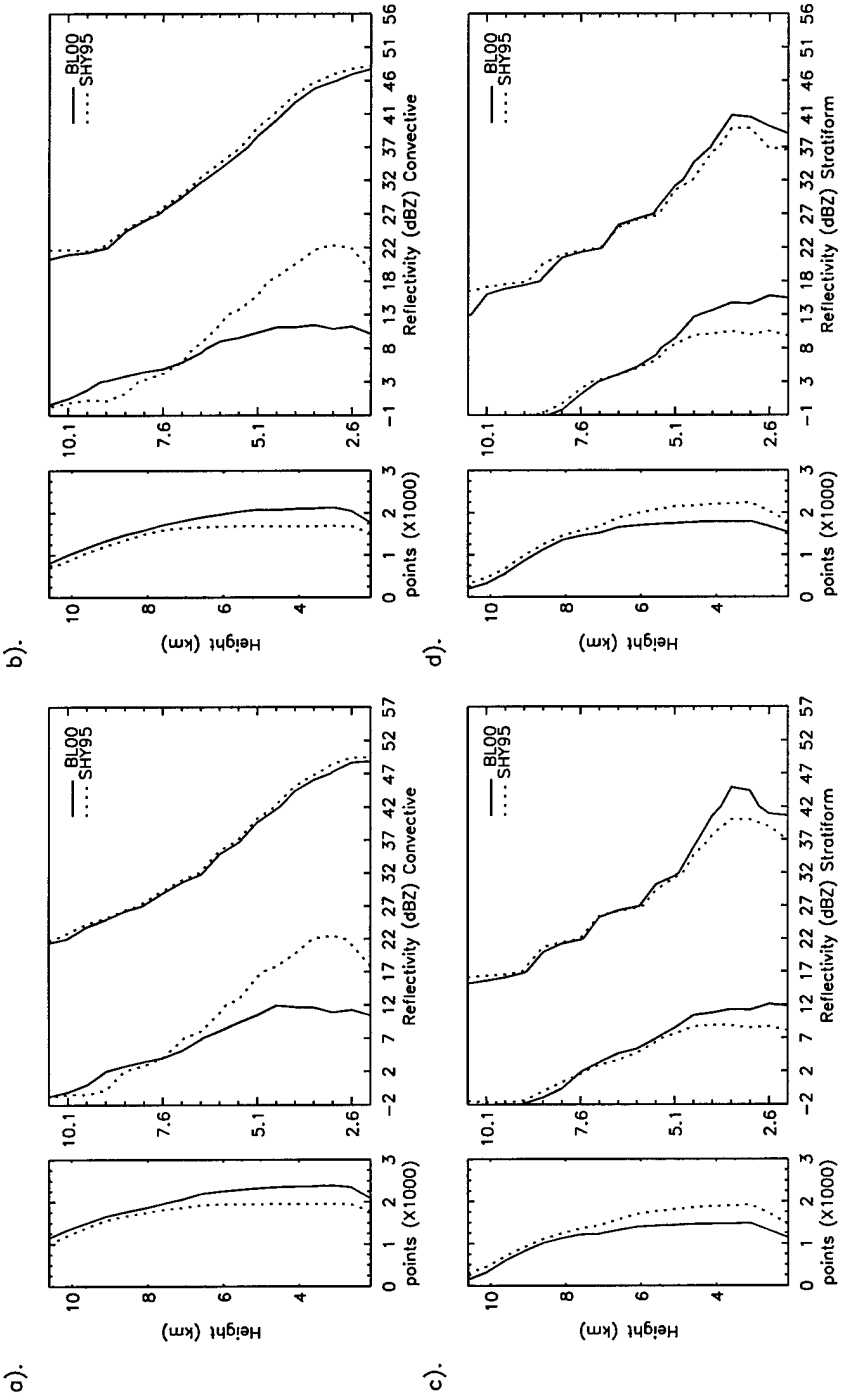

Fig. 16. Overlays of the 5% dBZ^{-1} km^{-1} contour from the contour frequency by altitude diagrams (CFAD) and the number of points used at each level to generate the CFADs for the convective (top) and stratiform (bottom) regions for the 23 May 1997 case. Bin size used was 5 dBZ. Solid line is for BL and dotted line is for SHY95. (a) and (c) is for 2158 UTC. (b) and (d) is for 2209 UTC.

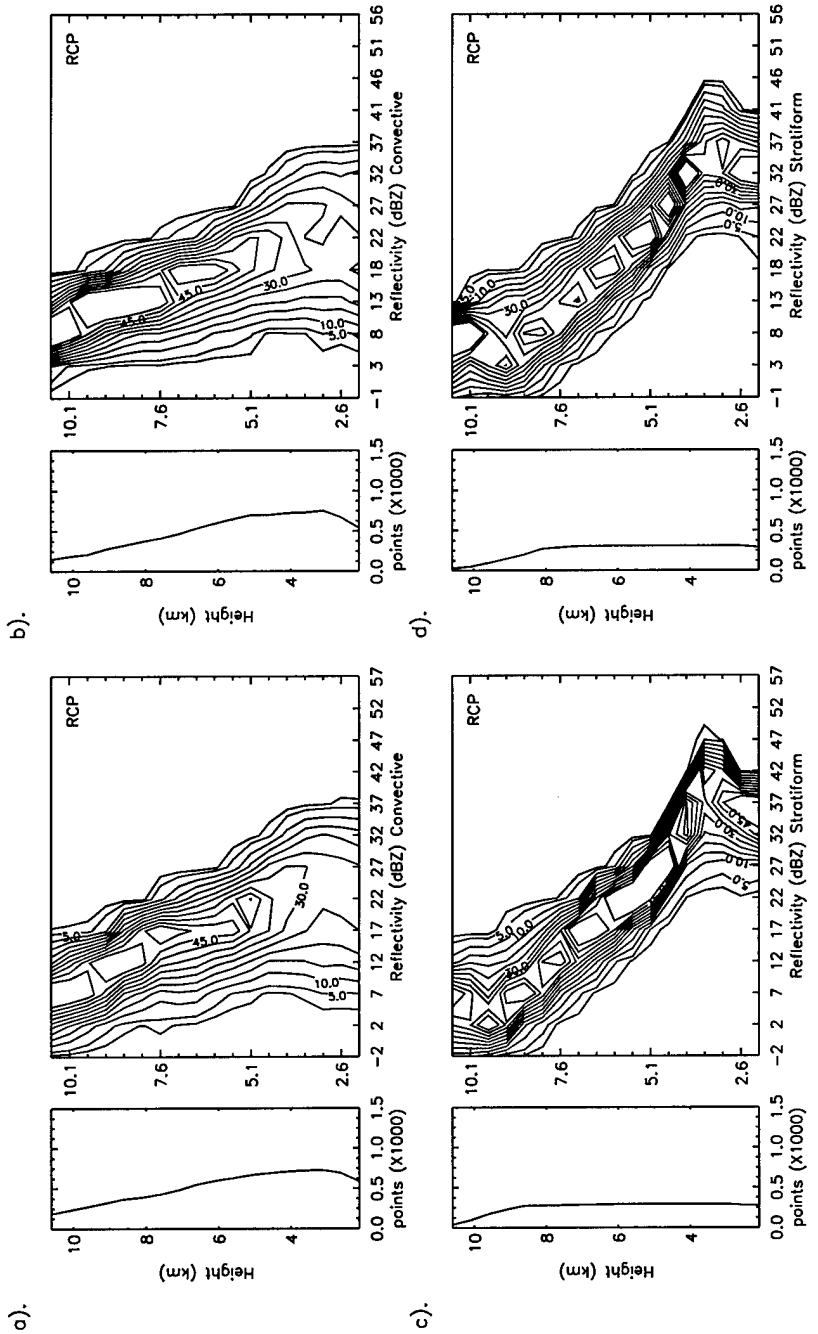

Fig. 17. CFADs and the number of points used at each level to generate the CFADs for the BL reclassified convective (top) and stratiform (bottom) regions for the 23 May 1997 case. Bin size used was 1 ms^{-1}. Contours start at 2% dBZ^{-1} km^{-1}. (a) and (c) is for 2158 UTC. (b) and (d) is for 2209 UTC.

indication of the presence of the bright band, further showing that these points were properly reclassified as stratiform.

f) Vertical Velocity CFADs

The CFADs of vertical velocity show similar results as those of the reflectivity CFADs. That is, the convective CFADs (Figs. 18a,b) show wider distributions in BL and SHY95 and narrow distributions in the stratiform regions (Figs. 18c,d). For both stratiform and convective regions, BL and SHY95 exhibit similar shapes in the contours with only minor differences appearing as a slight shift in the BL distributions toward lower vertical velocities in convective regions and a slight shift toward higher values in the stratiform regions (Fig. 19).

g) Mixed Phase Lapse Rates

Plots of the distribution of the 4 – 7 km lapse rates (Figs. 20 and 21) indicate that BL (solid) and SHY95 (dotted) have near normal and unimodal distributions for convective regions (Figs. 20a,b and 21a,b). Likewise, they peak at relatively the same values and the width of their distributions are generally the same. For the stratiform regions (Figs. 20c,d, and 21c,d), the two distributions are sometimes bimodal but appear somewhat similar in shape with BL showing higher peaks at times.

For the points that were reclassified as convective (dashed in Figs. 20a,b and 21a,b), the distributions are generally unimodal and have the same general shape as shown in the BL and SHY95 curves. However, the distributions for the reclassified

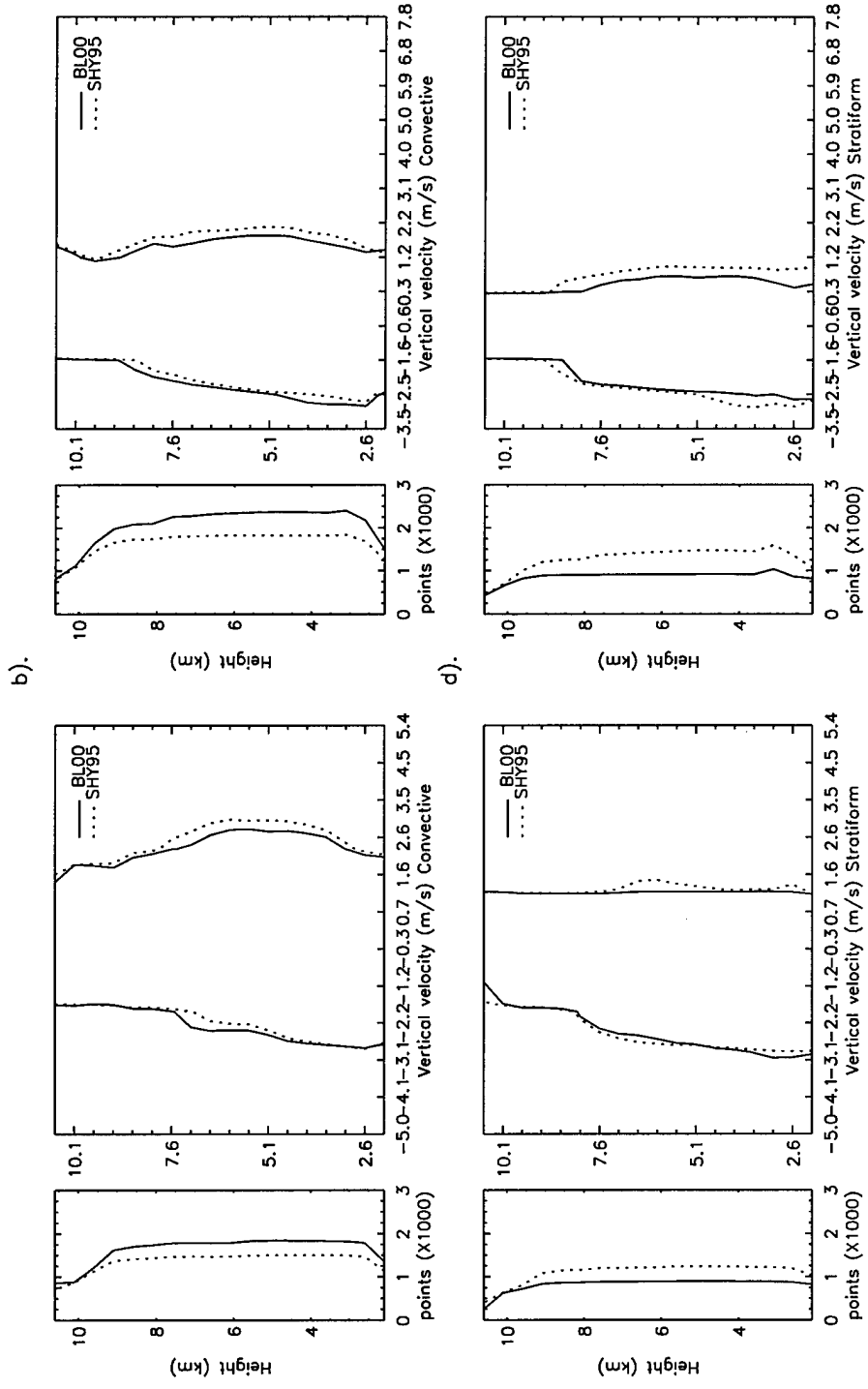

Fig. 18. Same as in Fig. 16 except for vertical velocity. (a) and (c) is for 2135 UTC. (b) and (d) is for 2147 UTC.

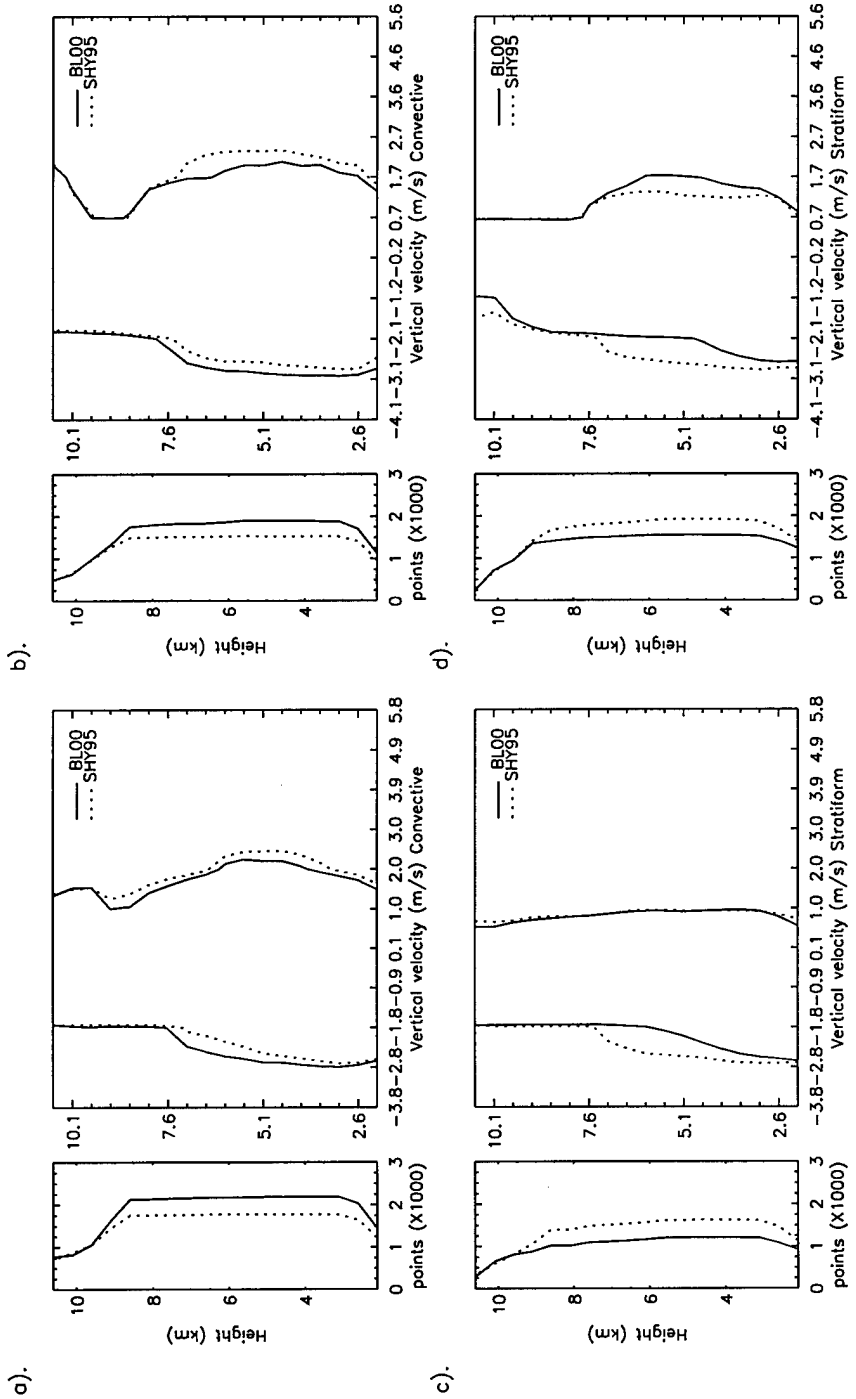

Fig. 19. Same as in Fig. 18 except for 2135 UTC and 2147 UTC.

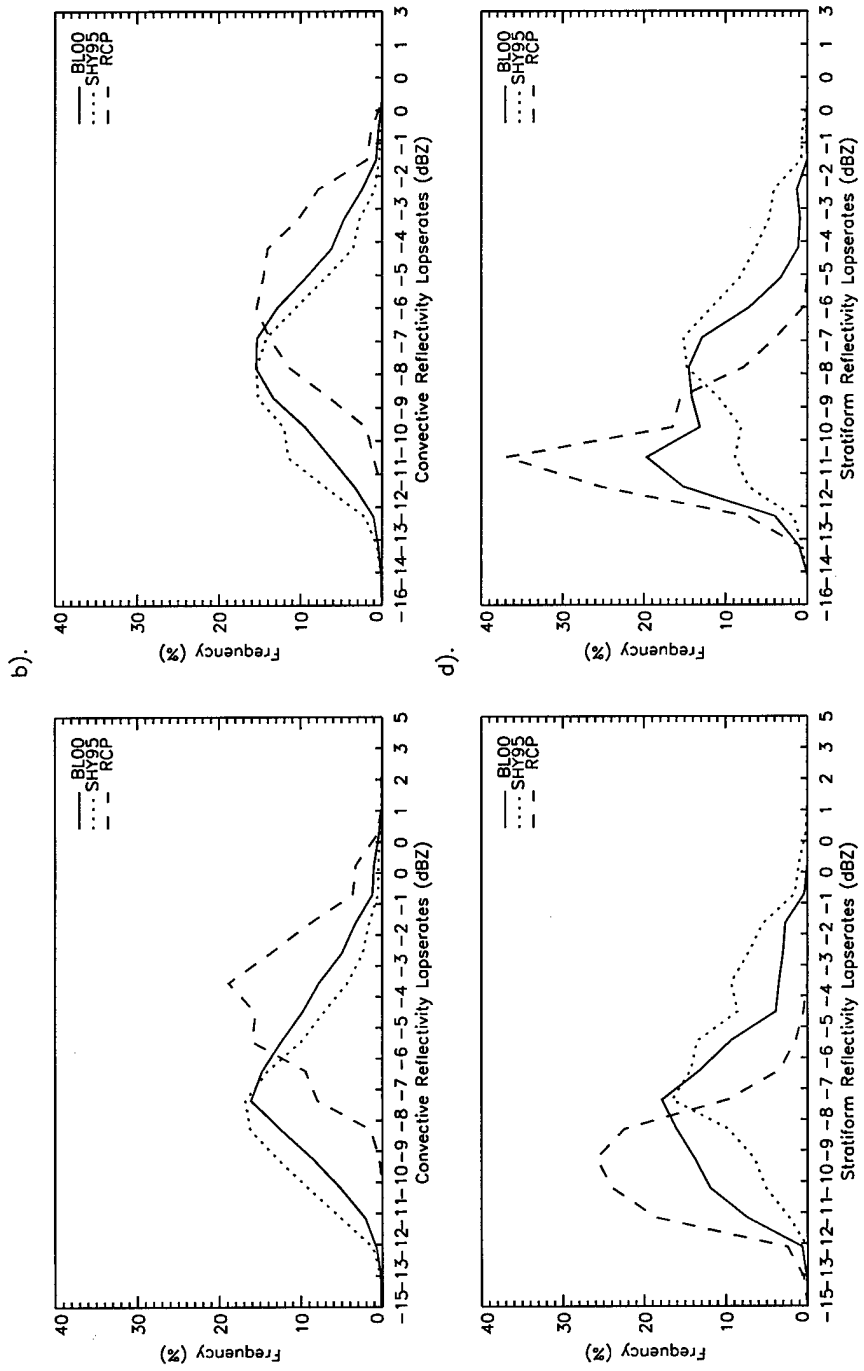

Fig. 20. Plots of the frequency (%) distribution of the reflectivity lapse rates for the convective and stratiform regions for the 23 May 1997 case. Solid line is for points as classified by BL. Dotted is for SHY95 and dashed is for the points reclassified by BL. (a) and (c) is for 2135 UTC. (b) and (d) is for 2147 UTC.

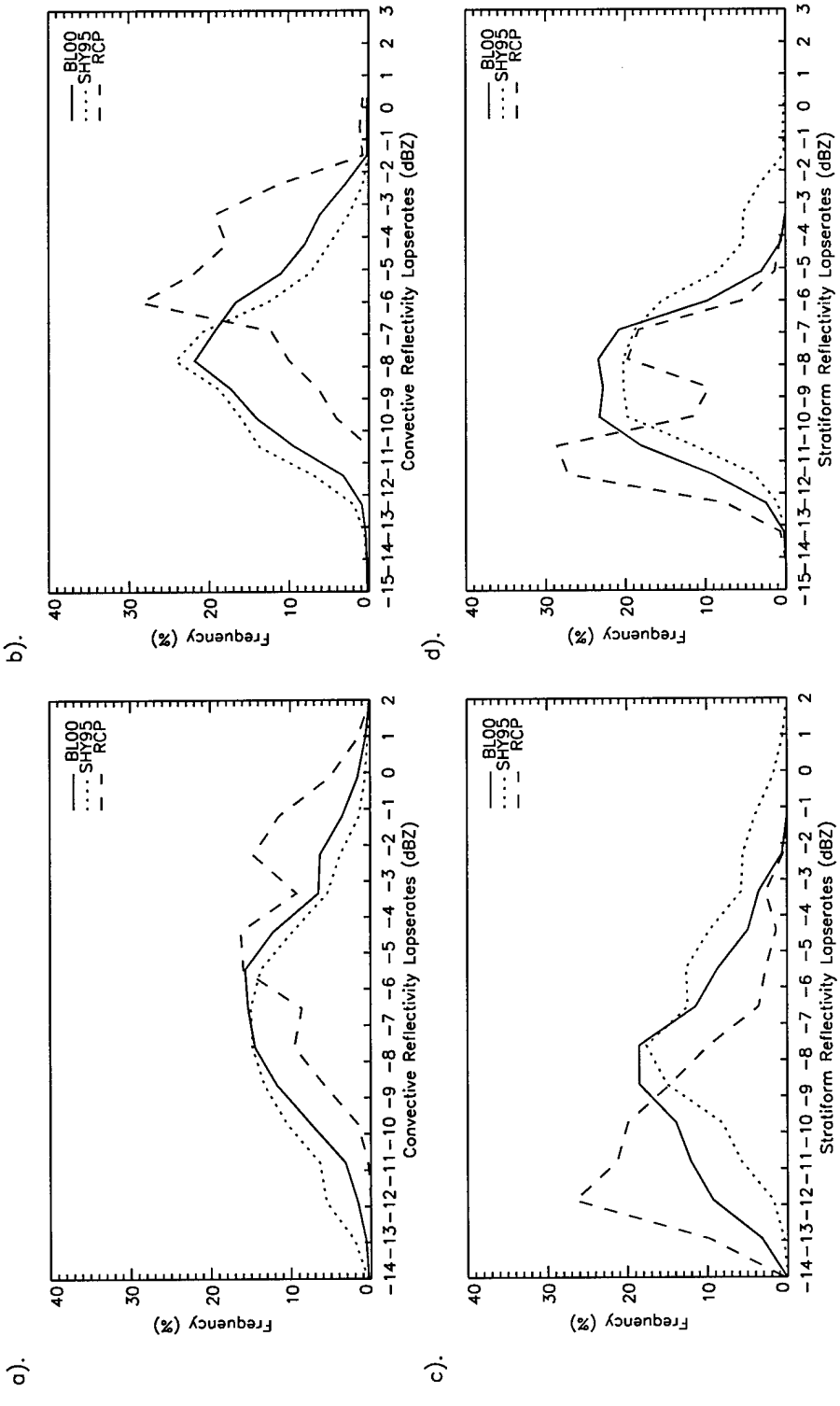

Fig. 21. As in Fig. 20 except for 2158 UTC and 2209 UTC.

points have peaks that are shifted toward lower lapse rates (e.g. more positive values), once again an indication that larger ice particles are being held aloft by stronger updrafts resulting in higher reflectivity values aloft. In regions where the points were reclassified to stratiform (Figs. 20c,d and 21c,d), the distributions are multimodal at times but generally have distributions that are shifted towards higher lapse rates (e.g. more negative values). These shifts in the lapse rate distributions for the reclassified points indicate that, overall, BL does a better job at classifying the convective and stratiform points than SHY95.

h) Multivolume Profiles, CFADs, and Lapse Rates

Multivolume products were created to represent the early development of the storm system as well as the mature stages of the system. The early stages are represented by combining the volume scans from 2051 UTC through 2135 UTC while the mature stage is represented by the 2147 UTC through 2209 UTC volume scans. It must be noted that the method used to determine the classification of a volume scan as "early" or "mature" was somewhat subjective. In this case, the classification was made based upon the stratiform region that develops in the bright band region. Those volume scans with a well-developed bright band region were considered as mature while the others were classified as early development.

The multivolume mean profiles of reflectivity and vertical velocity (Figs. 22 and 23) for the convective and stratiform regions show similar results as previously

discussed. The BL mean reflectivity values are slightly less than that of the SHY95 profiles for convective regions (Figs. 22a,b). In the stratiform regions (Figs. 22c,d) the BL profile has higher mean values for altitudes less than 8 km and lower values for those above 8 km. The profiles have similar slopes in the upper levels of the convective and stratiform regions for the early stages of the system (Figs. 22a,c). In the mature stages (Figs. 22b,d), the stratiform region has a smaller slope than its convective counterpart. Furthermore, the bright band is better depicted in the BL stratiform profile than in the SHY95 profile for the mature stage. The points reclassified as stratiform during the mature stage have a more pronounced bright band signature.

The BL and SHY95 mean vertical velocity profiles during the early stage show a net updraft in the convective regions (Figs. 23a,b) and subsidence in the stratiform regions (Figs. 23c,d). The mature stage convective regions also show a net updraft while the stratiform regions show subsidence below 6 km and weak upward vertical motion above 6 km, a reflection of the mesoscale updraft.

As expected, the BL and SHY95 reflectivity CFADs show the similar results as the CFADs for the individual volume scans. More important are the CFADs for the reclassified points. For the points that BL changed to convective (Figs. 24a,b), the CFADs show a wide distribution in the low levels with the mature stage having a slightly wider distribution. For the points that were reclassified as stratiform by BL (Figs. 25c,d), the CFADs have distributions that are much narrower than their convective counter parts and have the sharp diagonal pattern in the upper levels indicating a uniform reflectivity field. The mature stage stratiform CFAD also shows the peak in low-level

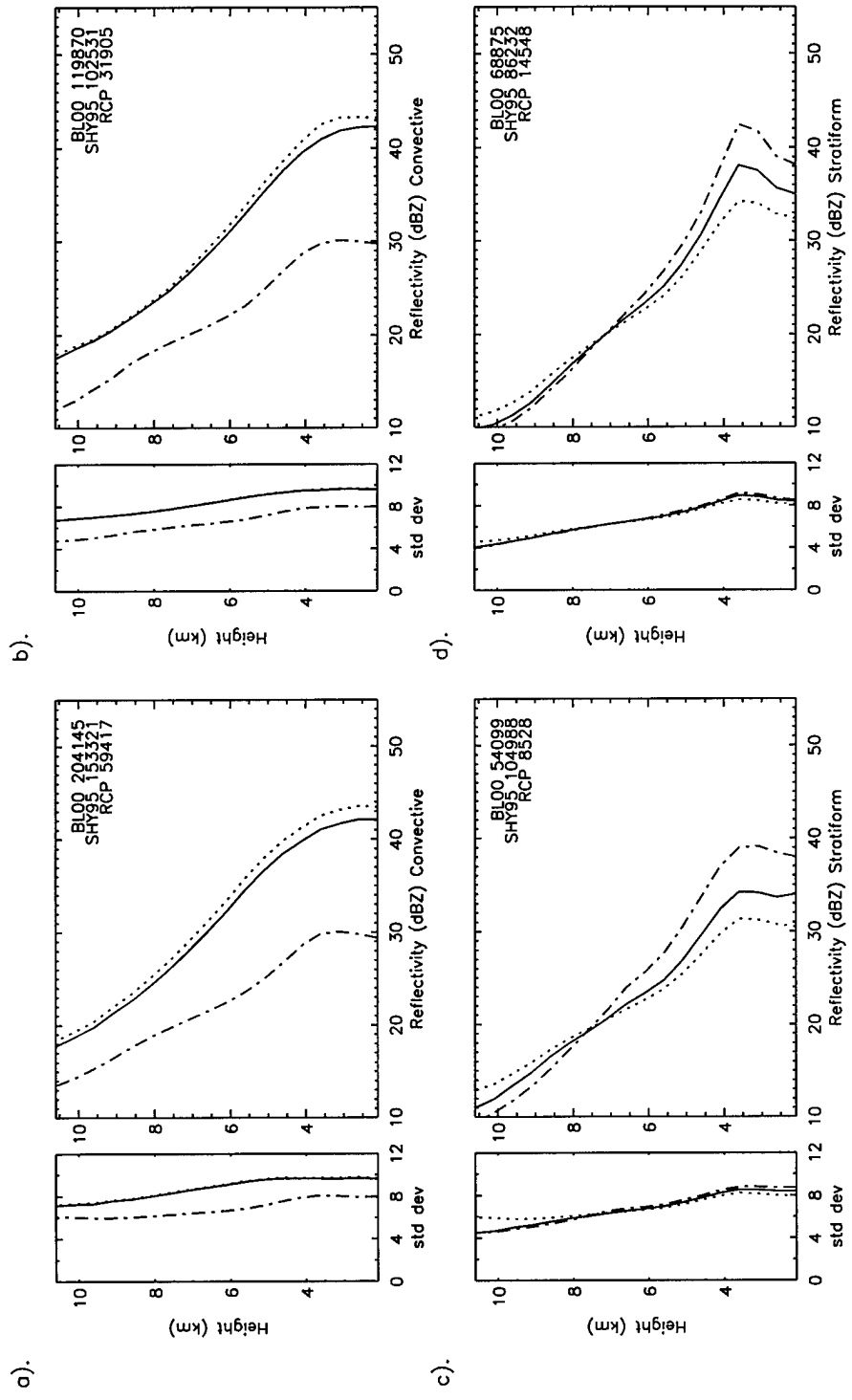

Fig. 22. Same as in Fig. 12 except for early (left) and mature (right) stages of the precipitation system. See text for a description on how the early and mature stages are defined.

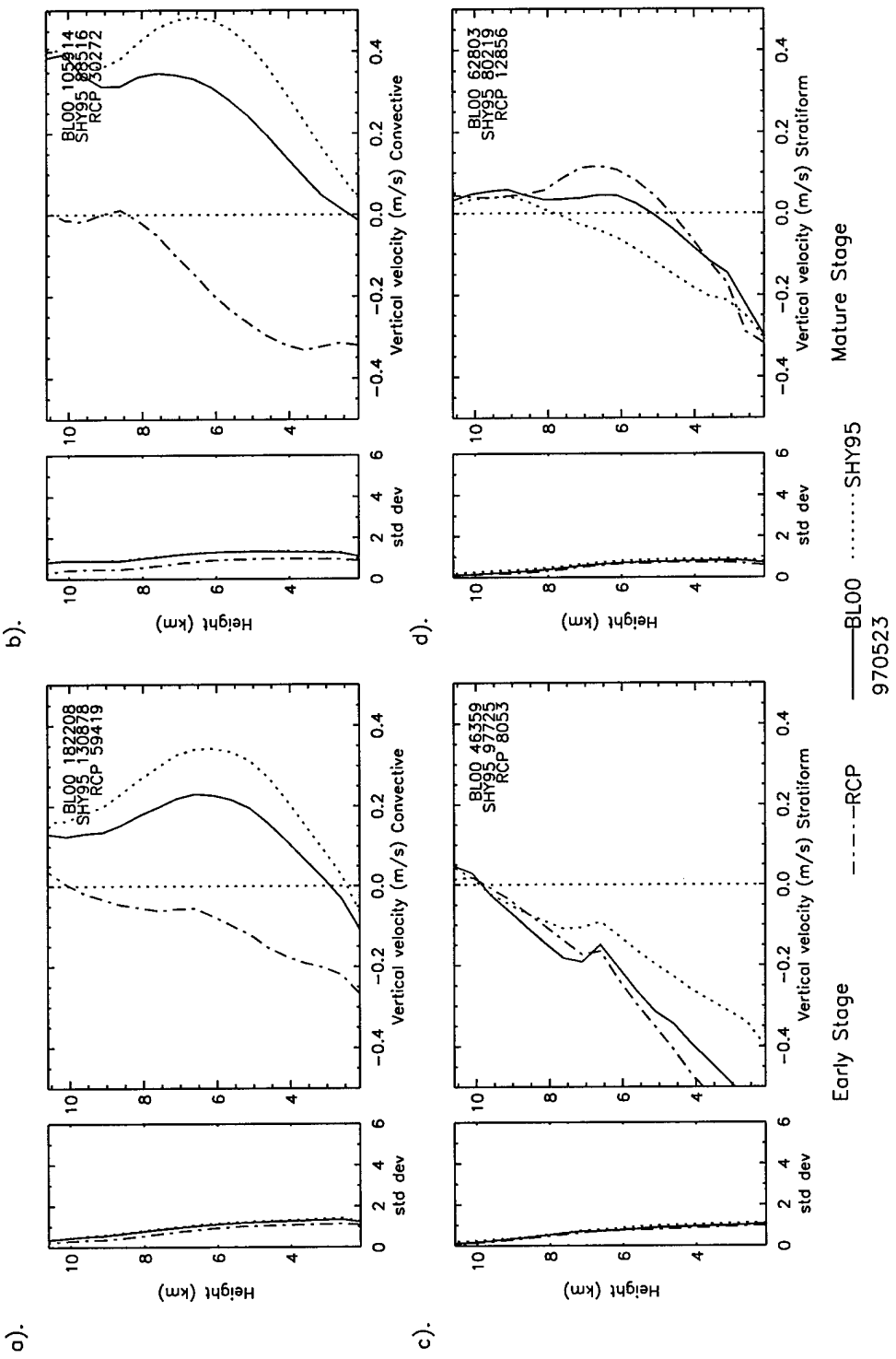

Fig. 23. Same as in Fig. 22 except for vertical velocity.

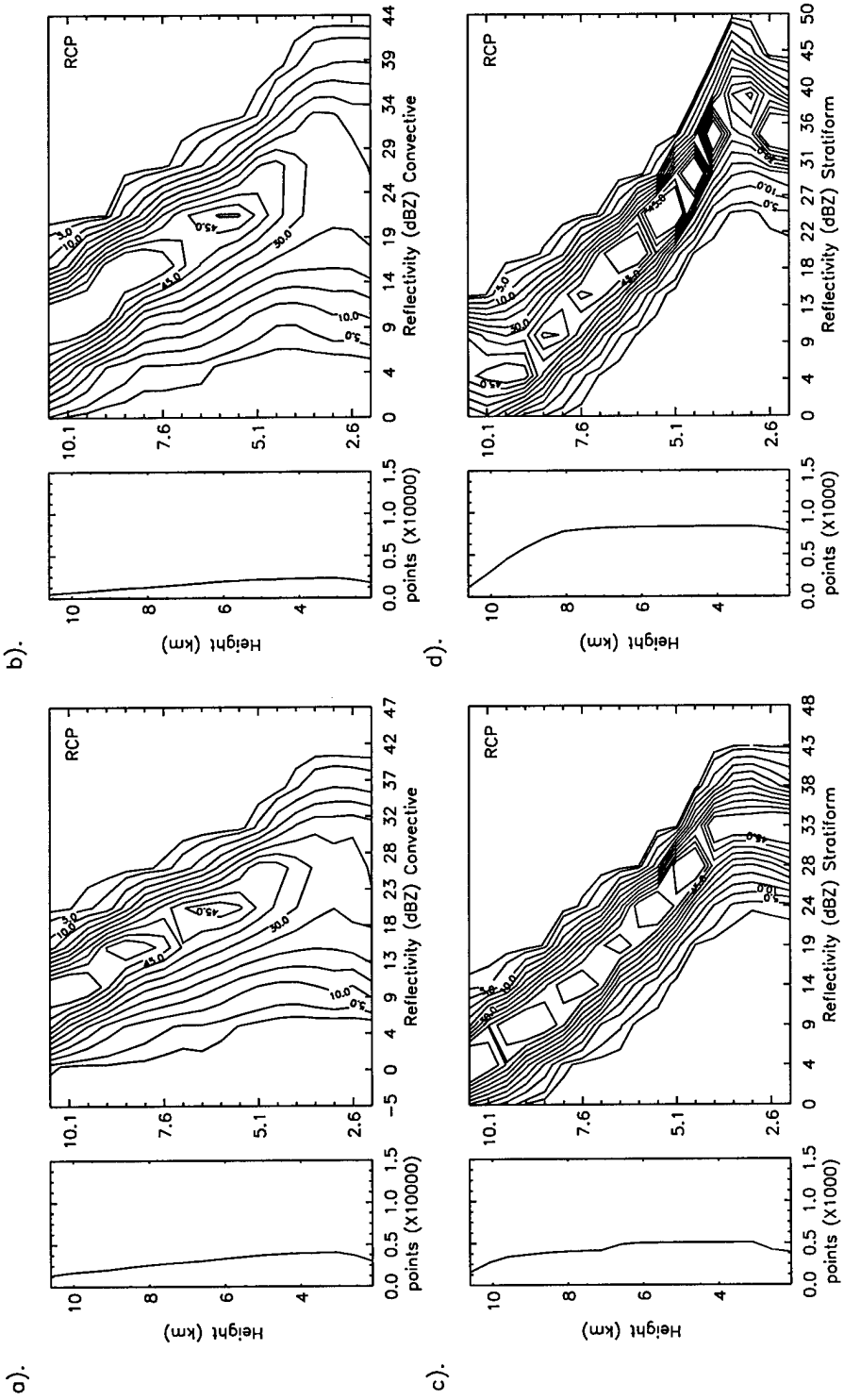

Fig. 24. As in Fig. 17 except for the early (left) and mature (right) stages of system development.

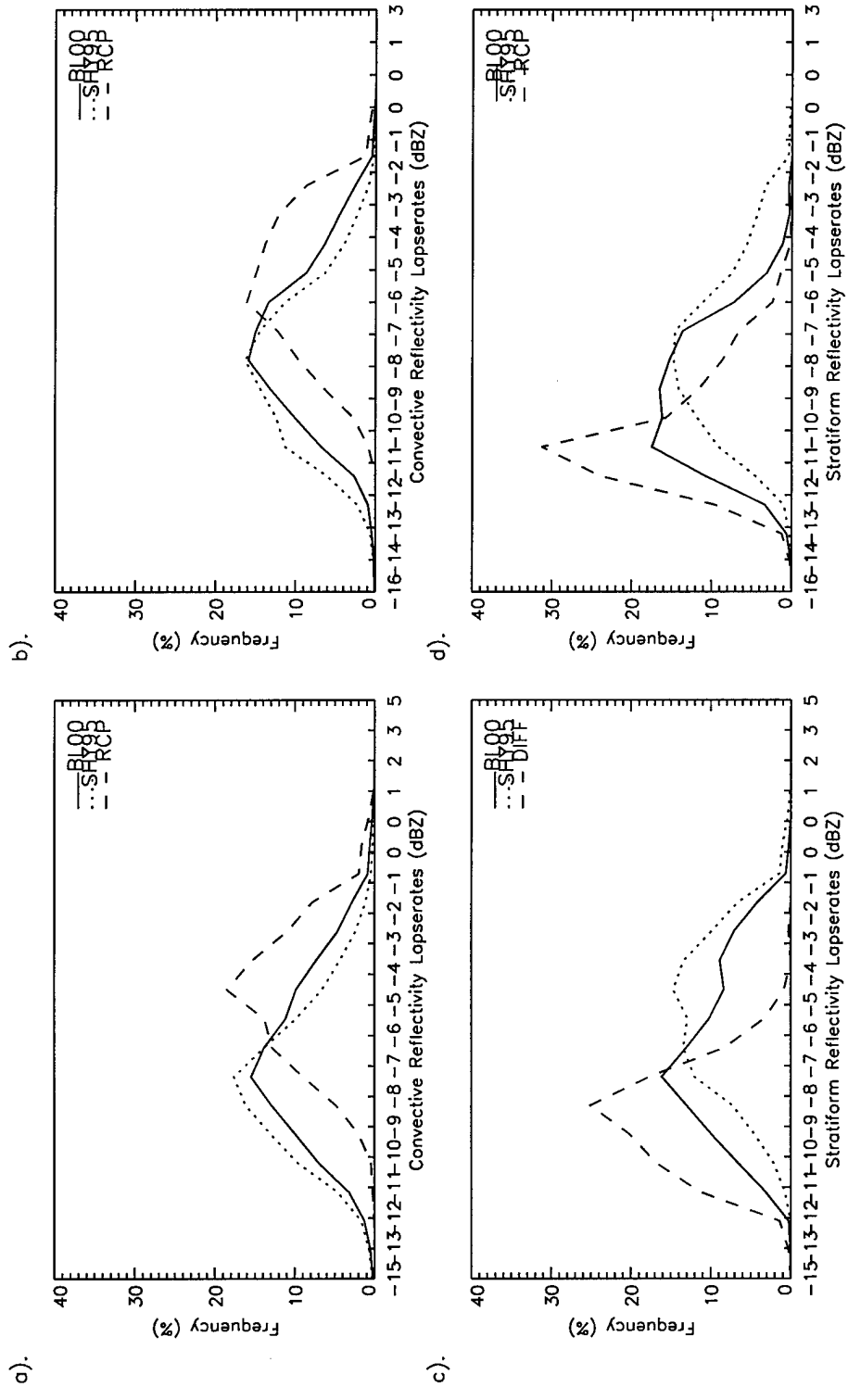

Fig. 25. As in Fig. 20 except for the early (left) and mature (right) stages of system development.

reflectivities below the melting level, further evidence of stratiform precipitation and therefore a proper reclassification of the points.

The multivolume reflectivity lapse rate distributions (Fig. 25) show the same results as those for the individual volume scans. One difference to point out though is the fact that the multivolume stratiform distributions (Figs. 25c,d) become somewhat more unimodal than compared to the individual volume scans, showing more clearly the shift in the BL distribution to higher lapse rates with the reclassified points shifted even further to higher lapse rates.

Case 2: An Asymmetric Squall Line (970524)

a) Reflectivity Description

This case spans 1853 UTC to 2224 UTC and includes ten volume scans of data. The evolution of the system is portrayed in the 3.1 km CAPPIs (Figs. 26 and 27). At 1853 UTC (Fig. 26a), two distinct bands of convection were oriented in a north – south direction. Reflectivity values for these bands are in excess of 55 dBZ. By 2034 UTC (Fig. 26c), these bands take on a more of an east – west orientation and encompass the southern portion of the system. The individual convective cells are still somewhat disorganized at this stage but a trailing stratiform region is now apparent. Within this stratiform region, a rather large area of high reflectivities (40 – 50 dBZ) resulting from the melting of ice particles can be seen. The leading line of convection becomes more

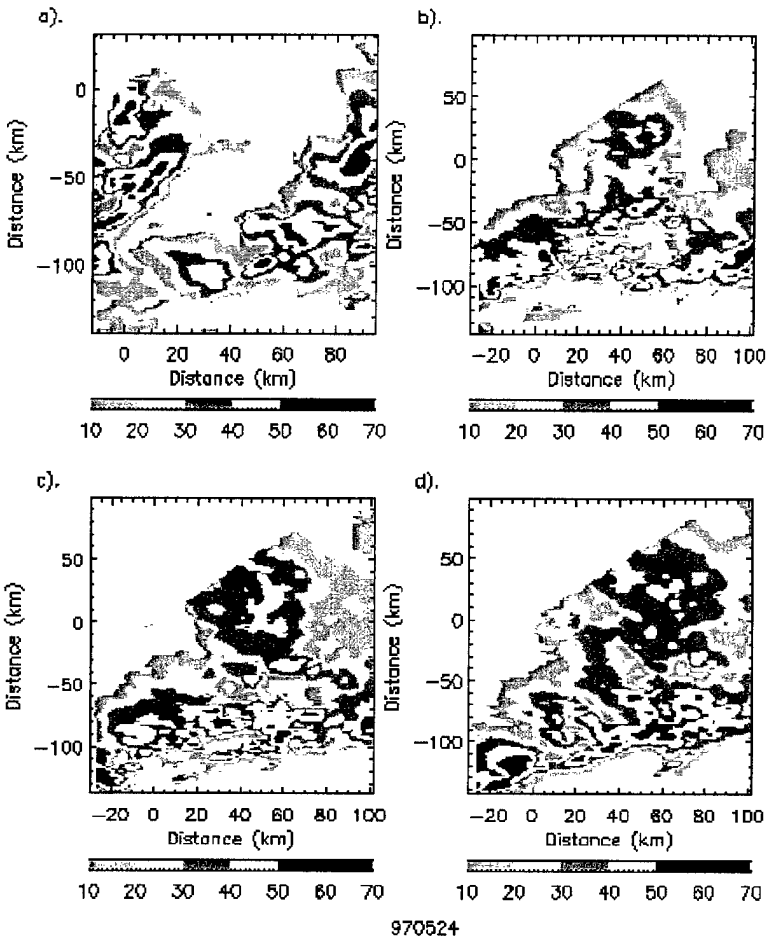

Fig. 26. Same as Fig. 6 except for the 24 May 1997 case. (a) 1930 UTC, (b) 2013 UTC, (c) 2034 UTC, (d) 2058 UTC.

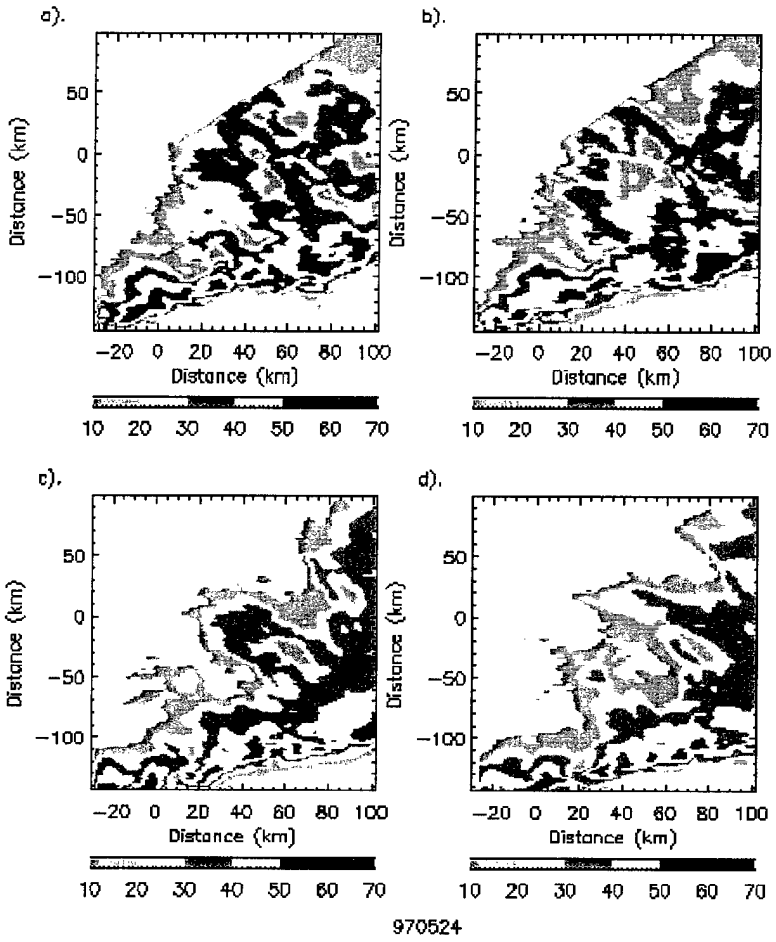

Fig. 27. Same as in Fig. 26 except for (a) 2112 UTC, (b) 2123 UTC, (c) 2155 UTC, (d) 2211 UTC.

organized by 2058 UTC (Fig. 26d) and forms a solid line by 2123 UTC (Fig. 27b) with an extensive trailing stratiform region.

b) BL and SHY95 Convective-Stratiform Maps

Figures 28, 29, 30, and 31 show the convective-stratiform maps for the two algorithms. Throughout the evolution of this system, the SHY95 algorithm consistently misclassifies the leading edge of convection as stratiform, such as in Fig. 30c. This deficiency was pointed out in a previous study (Biggerstaff and Listemaa, 2000). The BL algorithm correctly classifies these regions as convective (Fig. 30d). BL also classifies more of the region in between closely spaced cells as convective, as in Fig. 28d, whereas SHY95 continues to classify connective regions as those regions that are within close proximity to the 40 dBZ reflectivity contour (Fig. 28c). Other differences can be seen in the stratiform region as SHY95 once again classifies the high reflectivity associated with the bright band as convective (Fig. 29c). BL properly reclassifies most of this region as stratiform (Fig. 29d). However, as in the previous case, there are times when BL experiences problems in classifying the back edge of the stratiform region (Fig. 30d), but by the last volume scan (Fig. 31d) this seems to no longer be a problem resulting in a seemingly perfect partitioning of the system.

c) Mean Reflectivity Profiles

The profiles of mean reflectivity for the convective regions show similar results as the previous case where higher mean reflectivities are found in the low levels and the

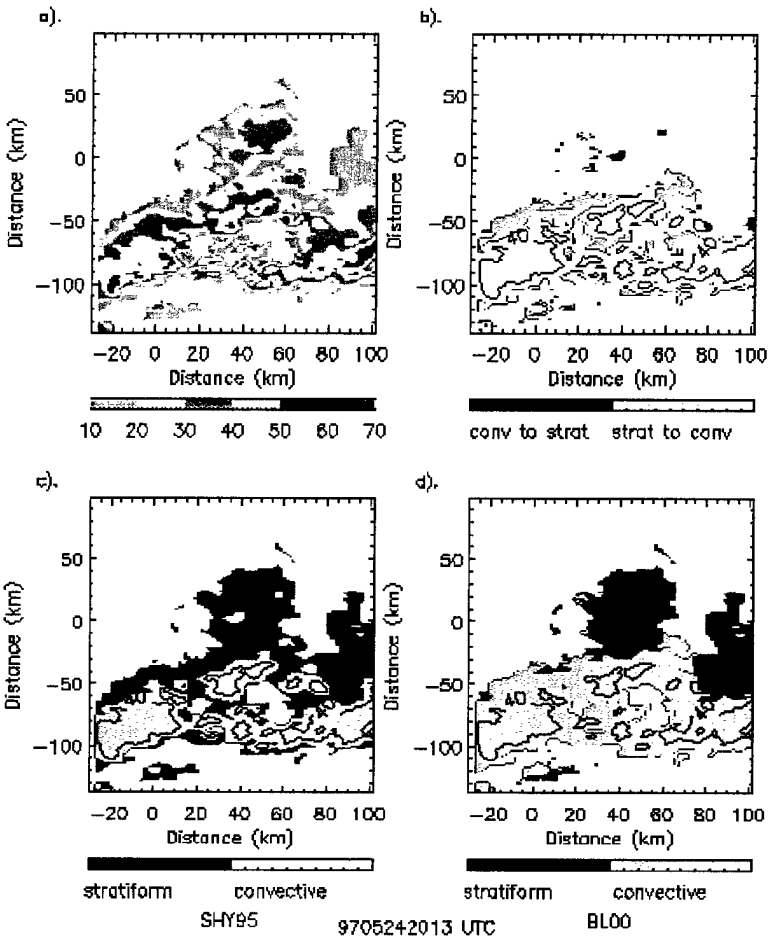

Fig. 28. As in Fig. 8 except for 2013 UTC 24 May 1997.

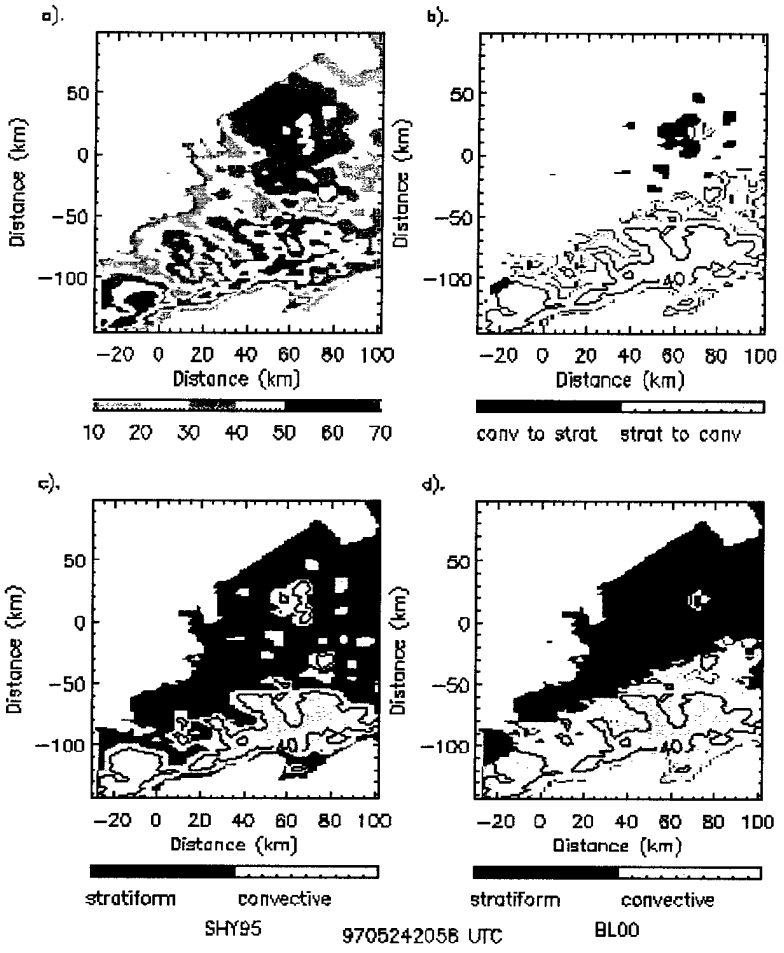

Fig. 29. As in Fig. 8 except for 2058 UTC 24 May 1997.

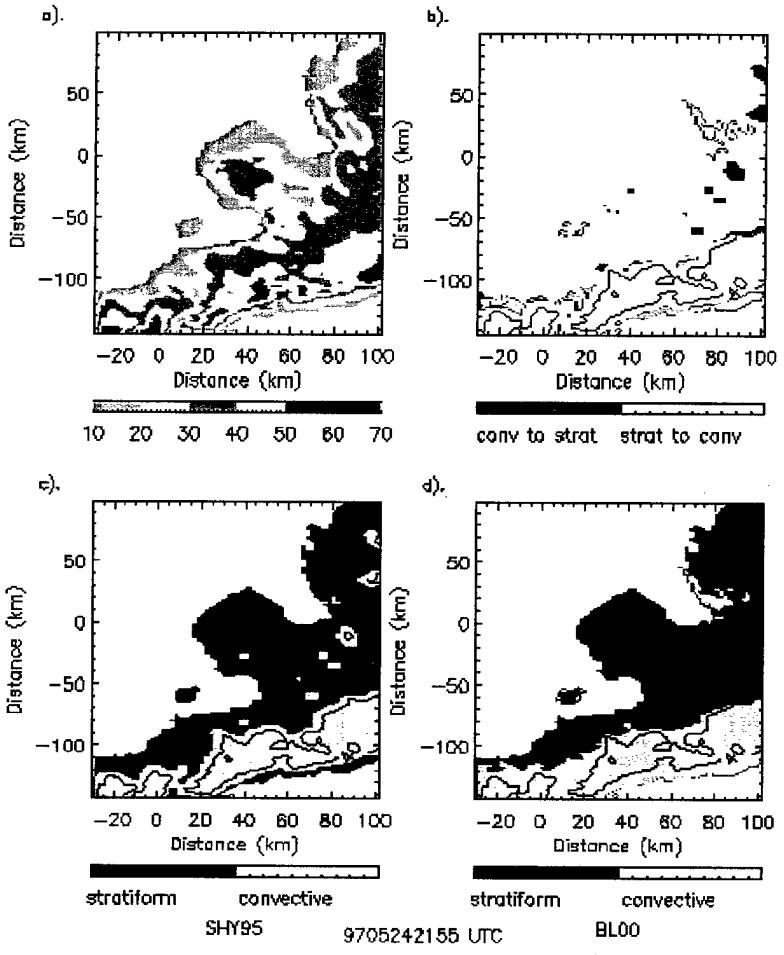

Fig. 30. As in Fig. 8 except for 2155 UTC 24 May 1997.

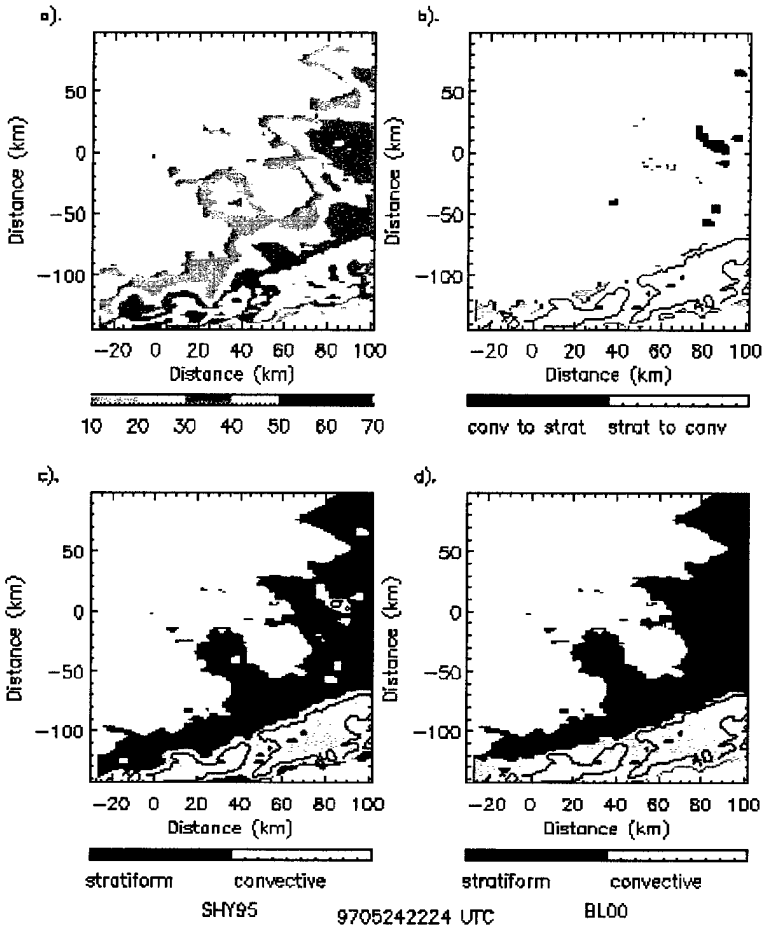

Fig. 31. As in Fig. 8 except for 2224 UTC 24 May 1997.

4 – 7 km lapse rates are small (Figs. 32 and 33). The BL and SHY95 profiles have similar shapes with the BL profiles indicating slightly weaker mean reflectivities (Figs. 32a,b and 33a,d). The profiles for the points that were reclassified as convective by BL have mean reflectivities that are 10 – 15 dBZ smaller than that of BL and SHY95. Furthermore, the profiles for these points have a much smaller lapse rate in the mixed phase region showing that these points were properly reclassified.

The stratiform profiles (Figs. 32c,d) also show results that are consistent with the ones in the previous case. Both the SHY95 and the BL profiles contain a peak in the mean reflectivity just below the melting level indicating the bright band associated with stratiform precipitation. The mixed phase region, however, contains lapse rates that are similar to that depicted in the convective profiles. This suggests that possibly too many points are being classified as stratiform and that some of these points may indeed be in regions of decaying convective cells. The BL curve indicates higher mean reflectivities throughout all levels during the early phases of development. When the trailing stratiform region becomes well-developed, the two profiles indicate nearly the same mean reflectivity values above 6 km (Figs. 33c,d). The profiles for the points that changed from convective to stratiform have similar shapes as the BL and SHY95 stratiform reflectivity profiles but with mean reflectivities that are close to 10 dBZ higher. In addition, the peak in the mean reflectivity below the melting level (~4 km) is more evident. This implies that BL generally does a nicer job in partitioning the system.

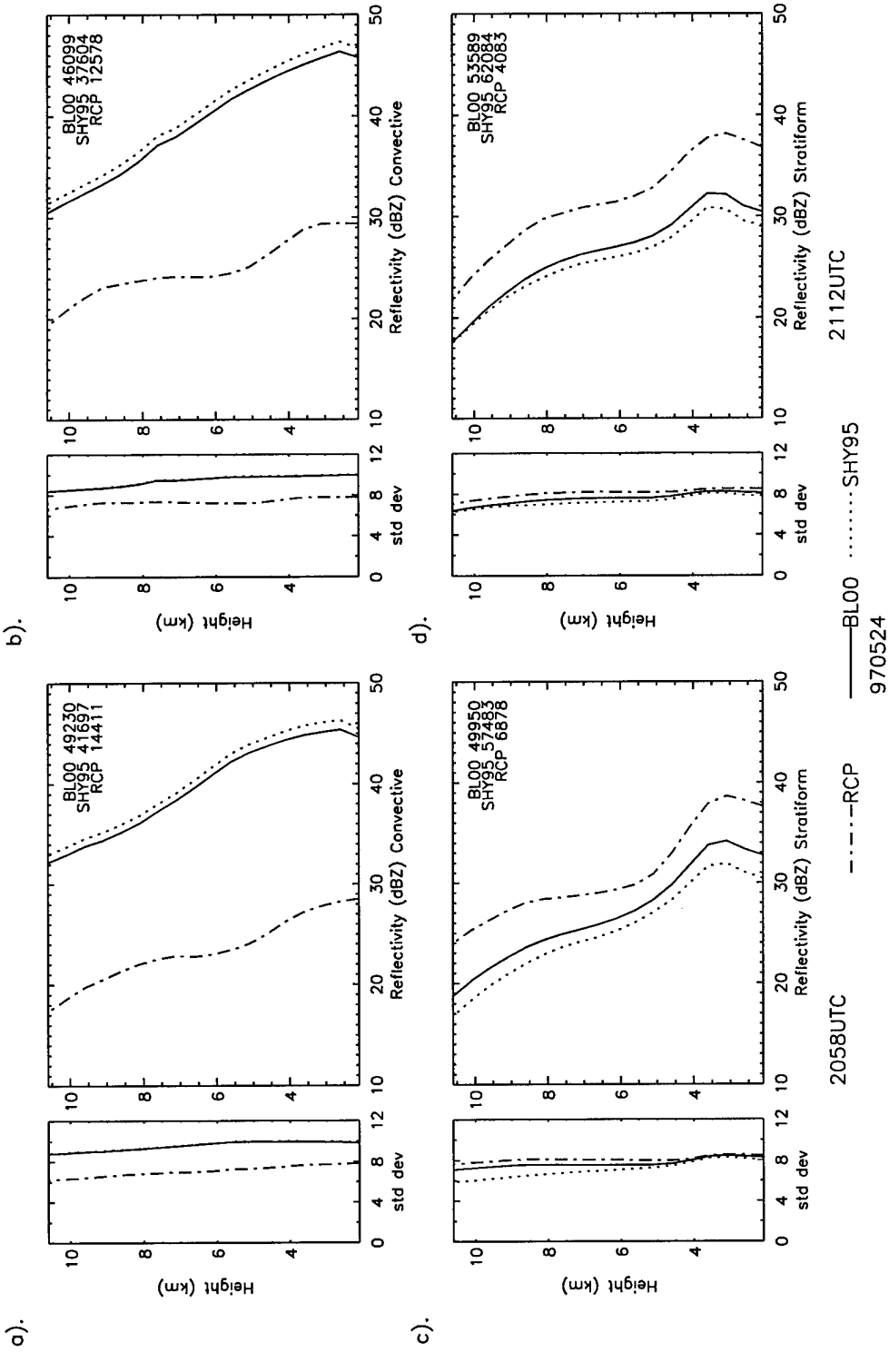

Fig. 32. As in Fig. 12 except for 2058 UTC and 2112 UTC 24 May 1997.

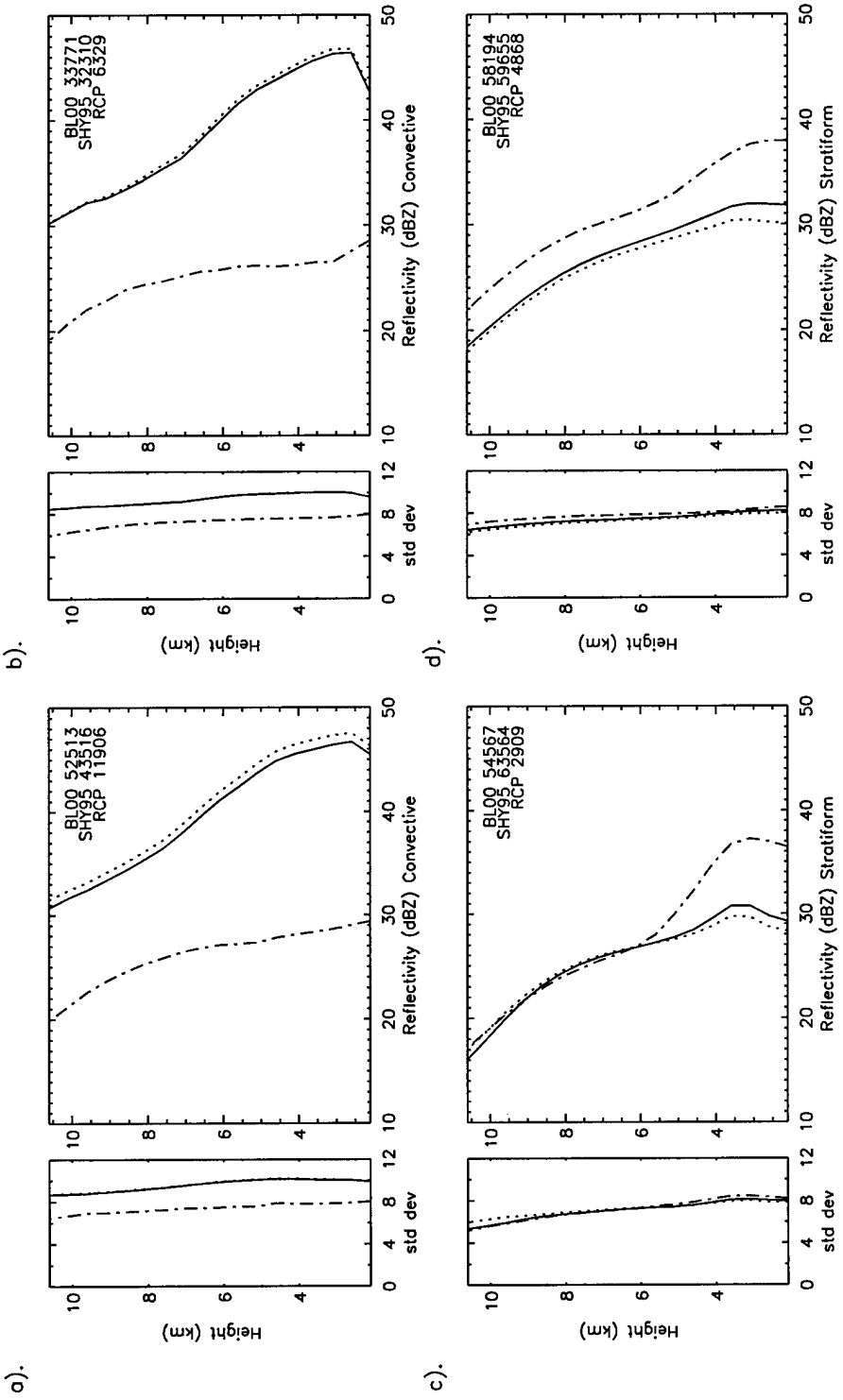

Fig. 33. As in Fig. 12 except for 2123 UTC and 2155 UTC 24 May 1997.

d) Mean Vertical Velocity Profiles

Profiles of the mean vertical velocities are shown in Figs. 34, 35, and 36. In the convective regions, both the BL and the SHY95 mean vertical velocity profiles show upward vertical motions in the upper levels (above 7 km) (Figs. 34a,b). Upward vertical motions are also indicated in the low levels (below 5 km) until 2155 UTC (Figs. 35a,b) where subsidence is indicated. In comparing the two together, there are times when the BL curves have higher mean vertical velocities than the SHY95 curves (Figs. 34a,b) while at other times they are lower, especially in the upper levels (Figs. 35a,b). The profiles for the points that were reclassified to convective contain weaker updrafts than BL and SHY95 until 2155 UTC where they indicate subsidence throughout all levels. Stronger subsidence is found in the upper levels between 8 and 10 km (Figs. 36a,b). Figure 30b shows that some of the points that were changed to convective were located along the front edge of the leading line of convection. Other points that were reclassified as convective are located on the back edge of the convective line and on the back edge of the trailing stratiform region. The points along the back edge of the convective line could be those that are associated with decaying convective cells which may explain the upper level subsidence. The upper level subsidence indicated could also be further enhanced by the incorrectly classified points in the trailing stratiform region. These points are located in the vicinity of the rear to front inflow notch which would lead to the subsidence profile seen in the upper and mid levels.

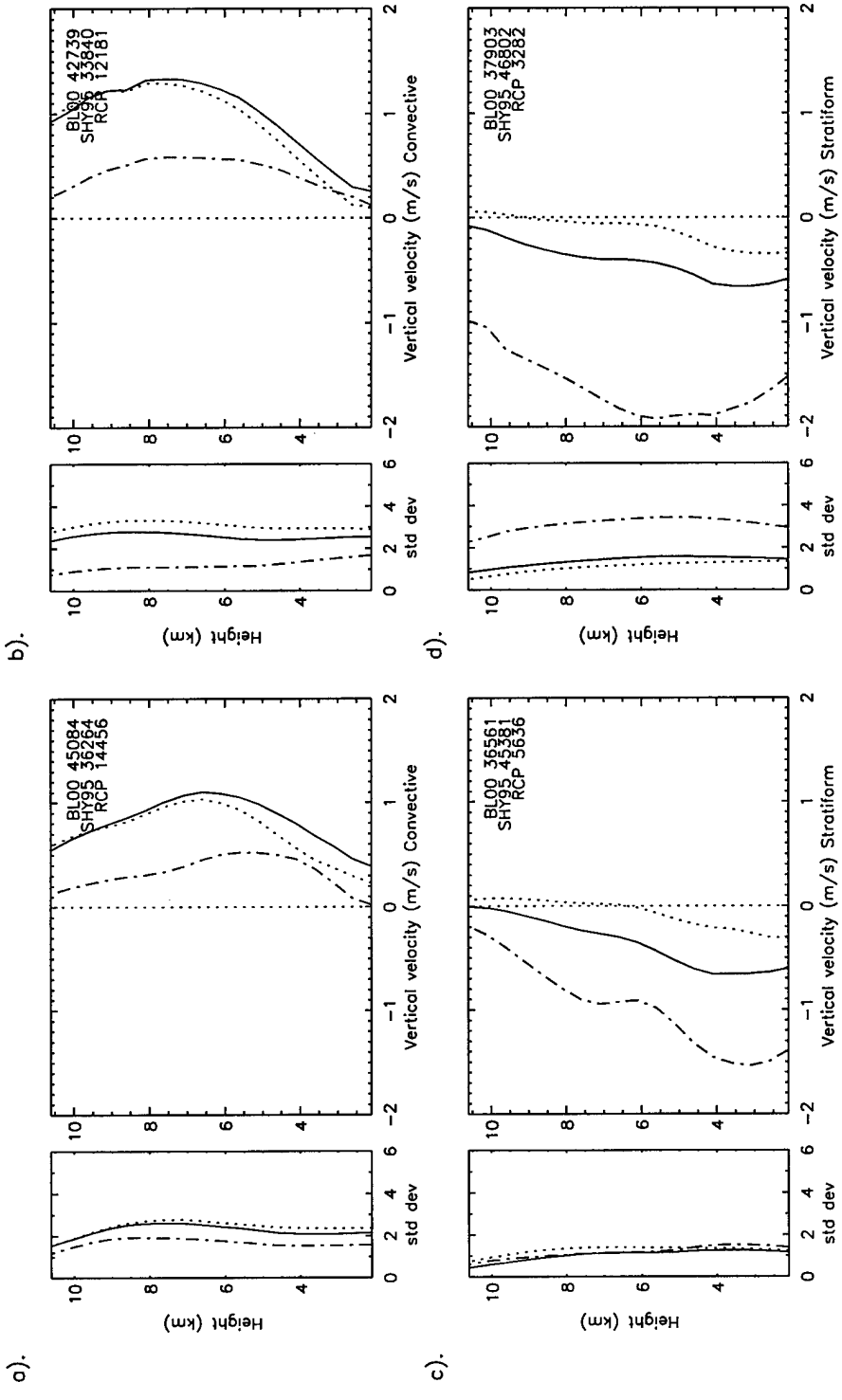

Fig. 34. Same as in Fig. 13 except for 2058 UTC and 2112 UTC of the 24 May 1997 case.

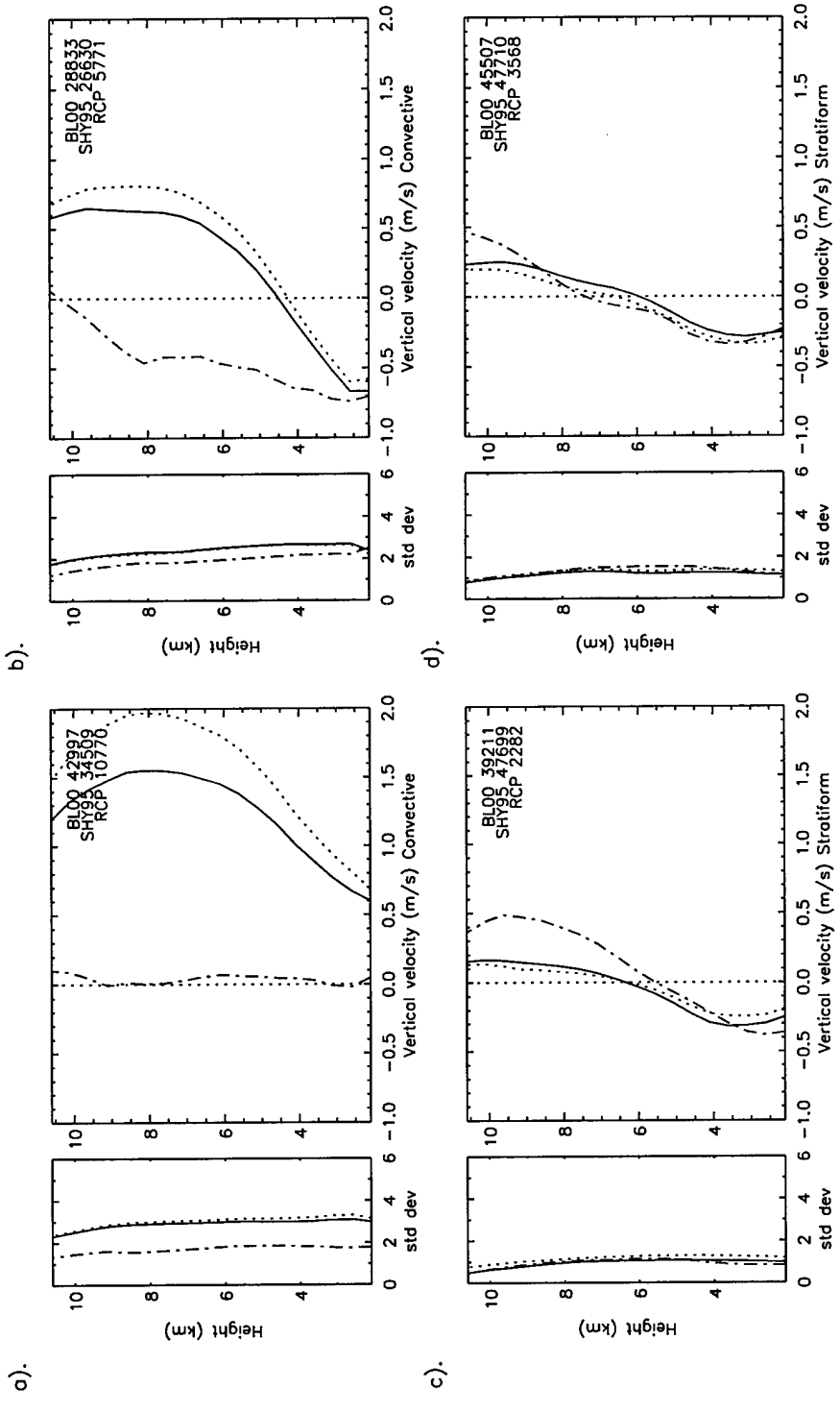

Fig. 35. Same as in Fig. 13 except for 2123 UTC and 2155 UTC of the 24 May 1997 case.

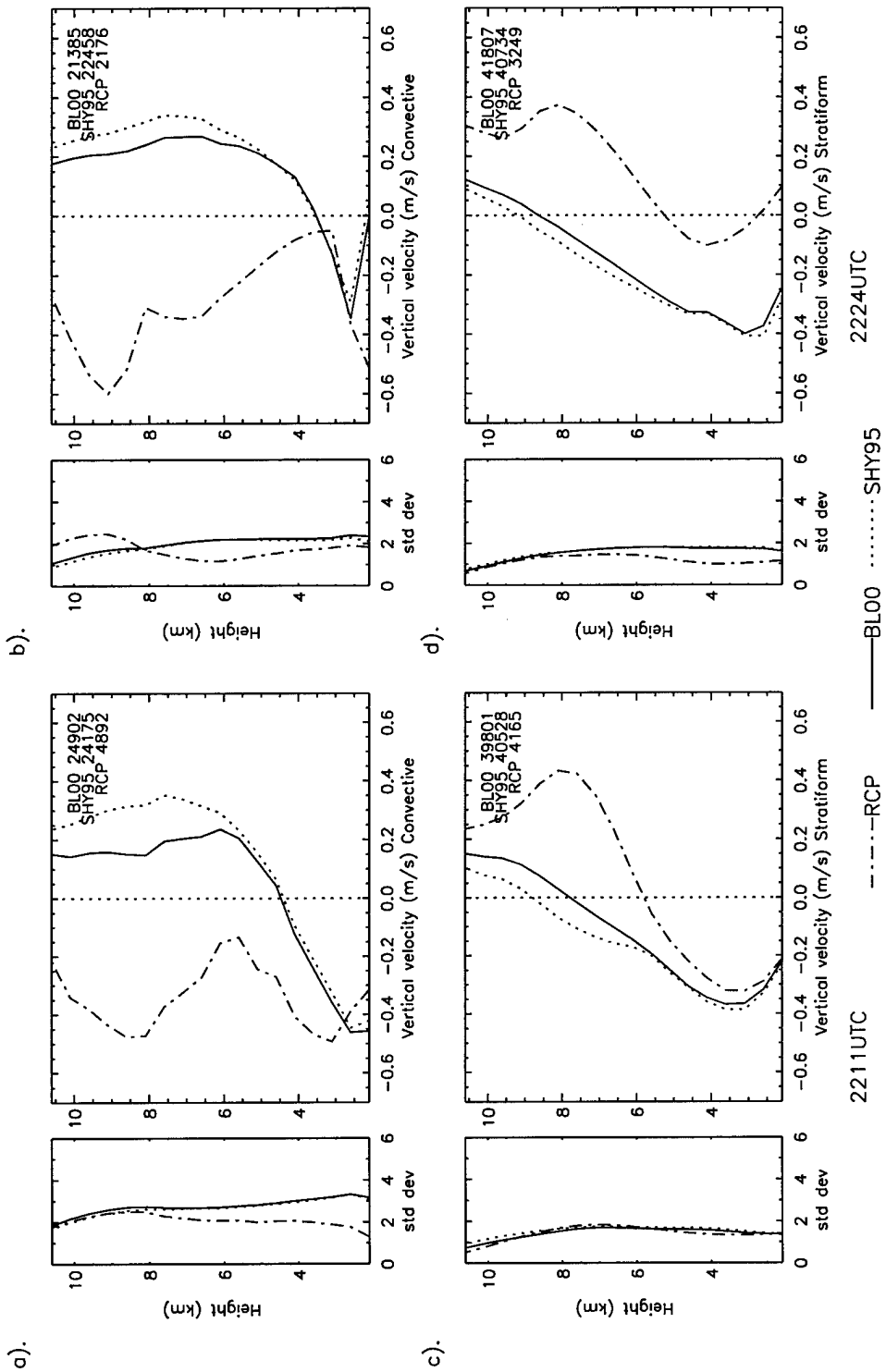

Fig. 36. Same as in Fig. 13 except for 2211 UTC and 2224 UTC of the 24 May 1997 case.

In the stratiform regions, the BL and SHY95 profiles indicate net subsidence until 2112 UTC (Figs. 34c,d) with BL having smaller mean values than that of SHY95. After 2112 UTC (Figs. 35c,d), the profiles take on the typical backward "S" shape often seen in stratiform vertical velocity profiles where the low levels contain subsidence and the upper levels contain upward vertical motion. For the points where BL changed the classification from convective to stratiform, this backward "S" profile is more pronounced, especially at 2211 UTC (Figs. 36c,d). In these profiles, the low level subsidence associated with the mesoscale downdraft is stronger as well as the mid and upper level updrafts associated with the mesoscale updraft. One can infer that BL correctly reclassified these points.

e) Reflectivity CFADs

A representative sample of reflectivity CFADs are shown in figures 37, 38, and 39. As expected, the BL reflectivity CFADs for the convective regions contain wider distributions in the low level reflectivity than shown in the SHY95 CFADs (Figs. 37a,b). In the stratiform regions, BL has a slightly narrower distribution in the mid level reflectivities (Figs. 37c,d). In the low levels, a slightly wider distribution can be seen in the later volume scans where BL correctly classified the enhanced regions of reflectivity in the stratiform region that resulted from the melting of ice particles (Figs. 38c,d). The frequency distributions shown in the CFADs for the reclassified points (Fig. 39c,d) have narrow distributions in the stratiform regions and wide distributions in the convective

regions. Furthermore, there is a weak indication of the enhanced reflectivity values associated with melting ice particles in the stratiform regions. It is not as pronounced as in the previous case because fewer points were reclassified from convective to stratiform. This is because the area of enhanced reflectivity in the stratiform region was not as extensive as in the previous case.

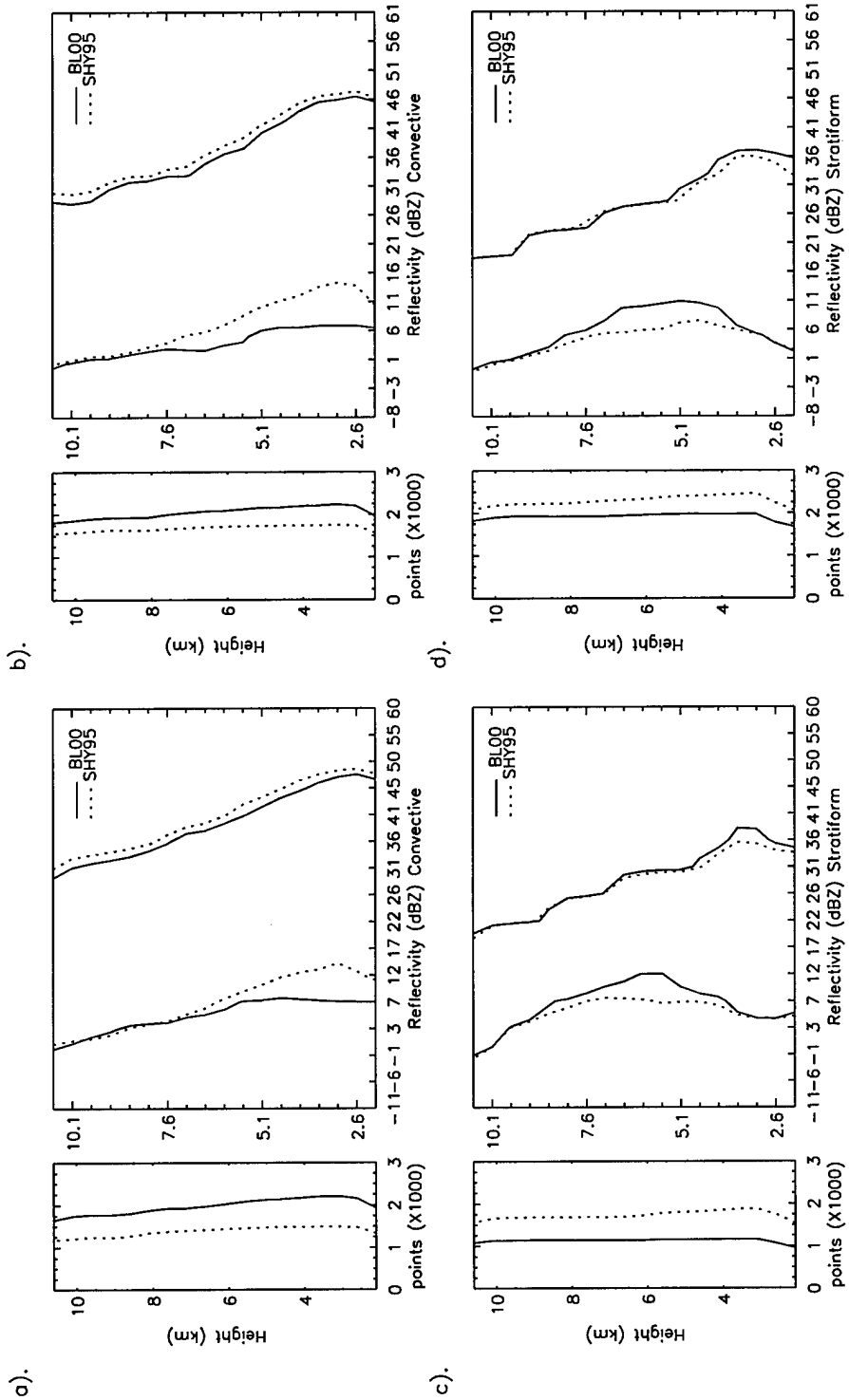

Fig. 37. As in Fig. 16 except for the 24 May 1997 case. (a) and (c) are for 2013 UTC. (b) and (d) are for 2034 UTC.

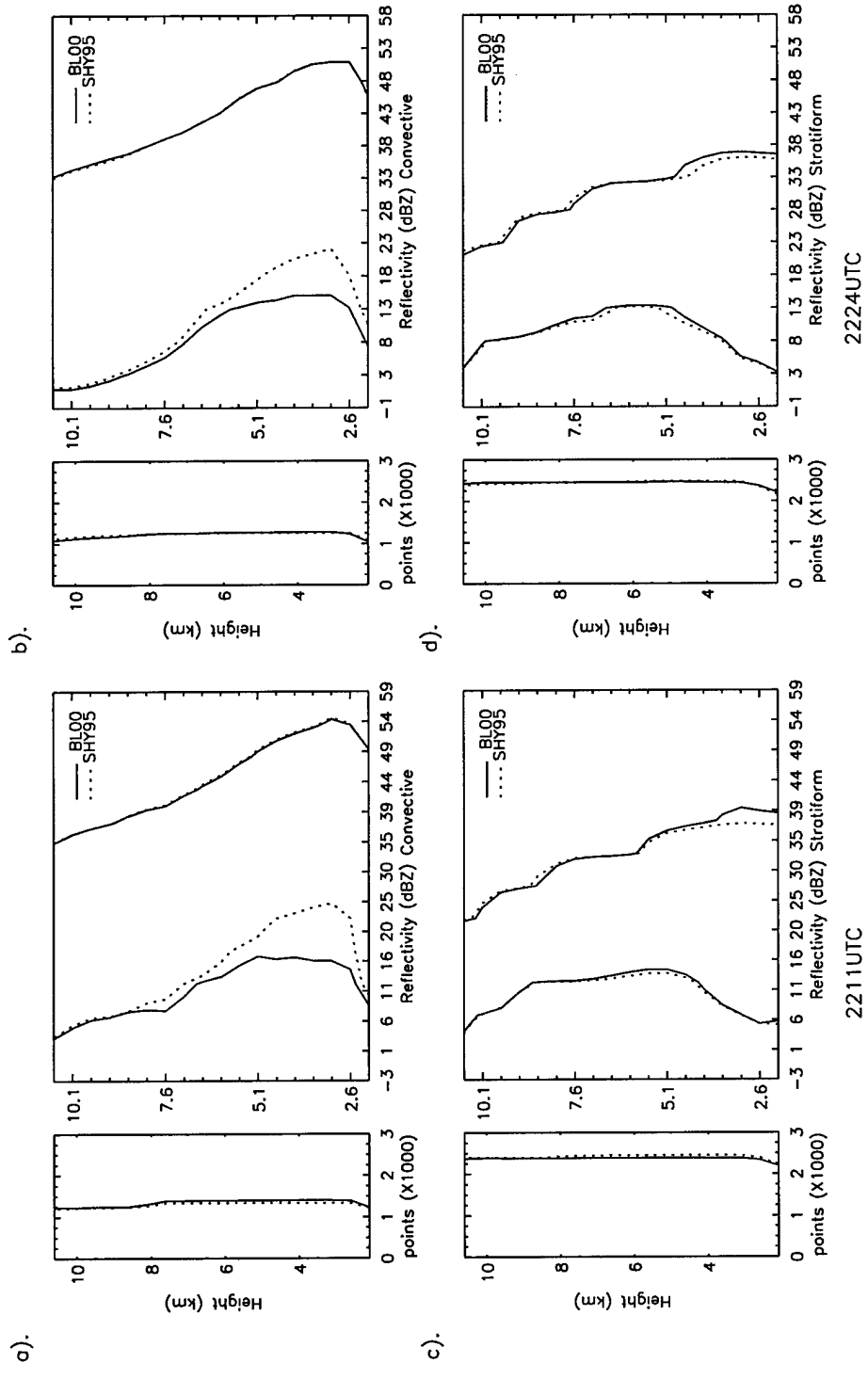

Fig. 38. As in Fig. 16 except for the 24 May 1997 case. (a) and (c) are for 2211 UTC. (b) and (d) are for 2224 UTC.

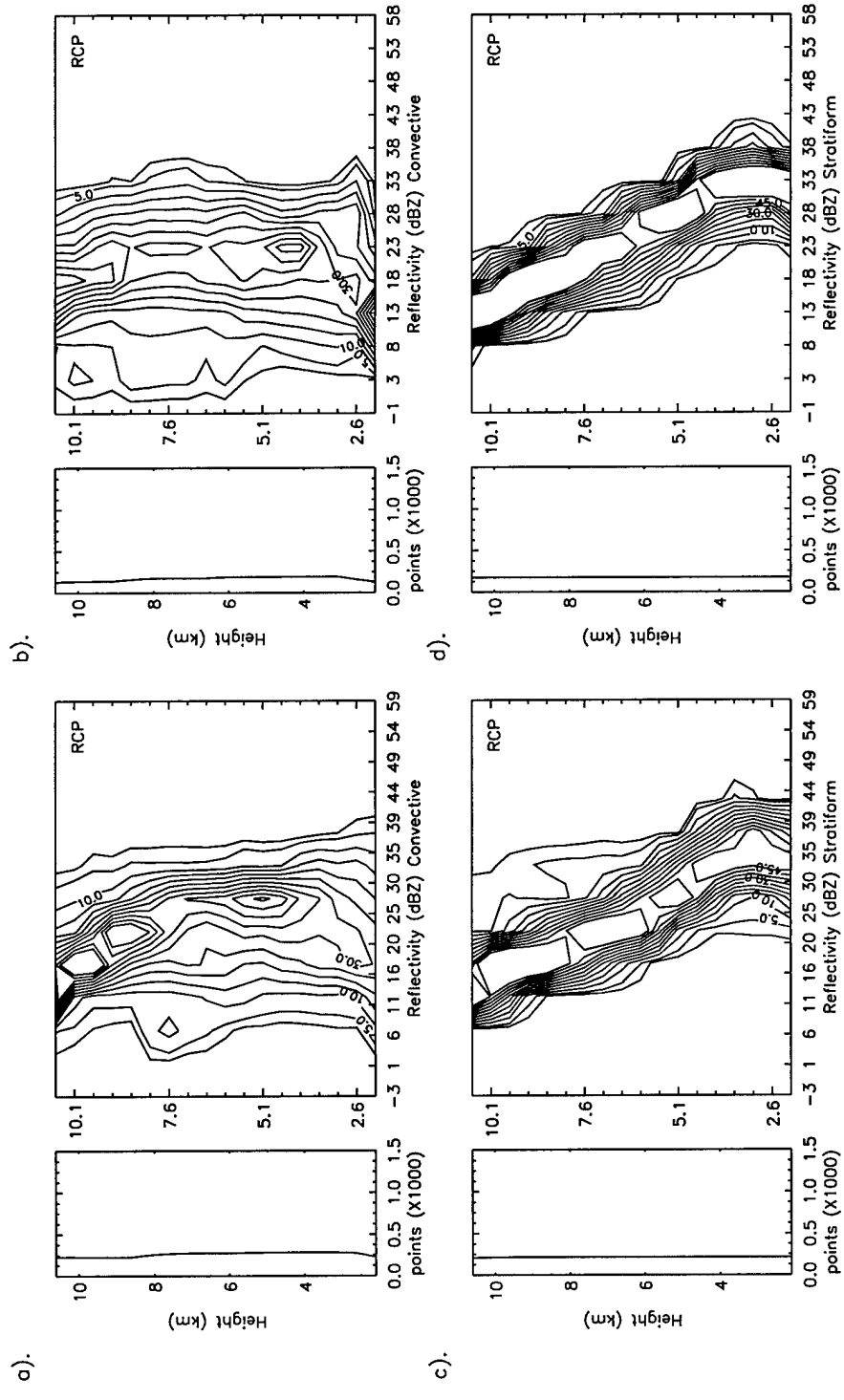

Fig. 39. As in Fig. 17 except for the 24 May 1997 case. (a) and (c) are for 2211 UTC. (b) and (d) are for 2224 UTC.

f) Vertical Velocity CFADs

The CFADs of vertical velocity have similar shapes for both BL and SHY95. This is true for the convective and the stratiform regions. In general, the stratiform CFADs have narrower vertical velocity distributions than the convective CFADs (Fig. 40). For the reclassified points, the convective and stratiform CFADs are somewhat similar. One slight difference is that the contours for the points that were reclassified as convective show a stratiform pattern. This reveals that BL incorrectly classified the back edge of the trailing stratiform region as convective (Fig. 41a).

g) Mixed Phase Lapse Rates

The convective region 4 - 7 km lapse rate distributions show similar results as in the first case. The BL and SHY95 distributions are unimodal and nearly normal for BL and SHY95 with the BL distributions slightly shifted toward smaller lapse rates as seen in figures 42a,b and 43a,b. The lapse rate distributions for the points that were reclassified as convective are often bimodal but continue to have distributions that are shifted to smaller lapse rates (Figs. 43a,b) implying that these should have generally been reclassified as convective. The points that were incorrectly reclassified probably lead to the bimodal distribution seen in these points.

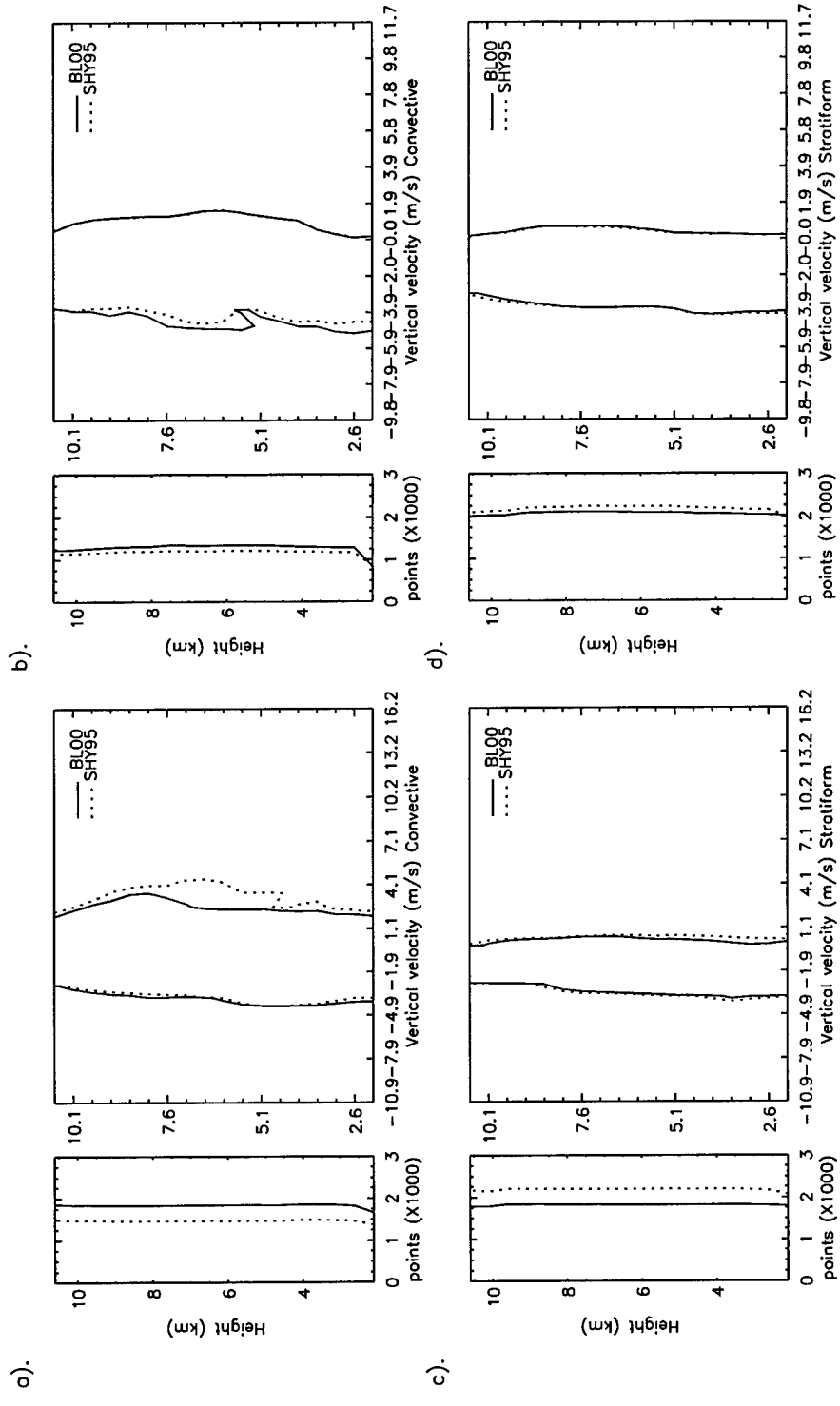

Fig. 40. As in Fig. 18 except for 2013 UTC and 2034 UTC from the 24 May 1997 case.

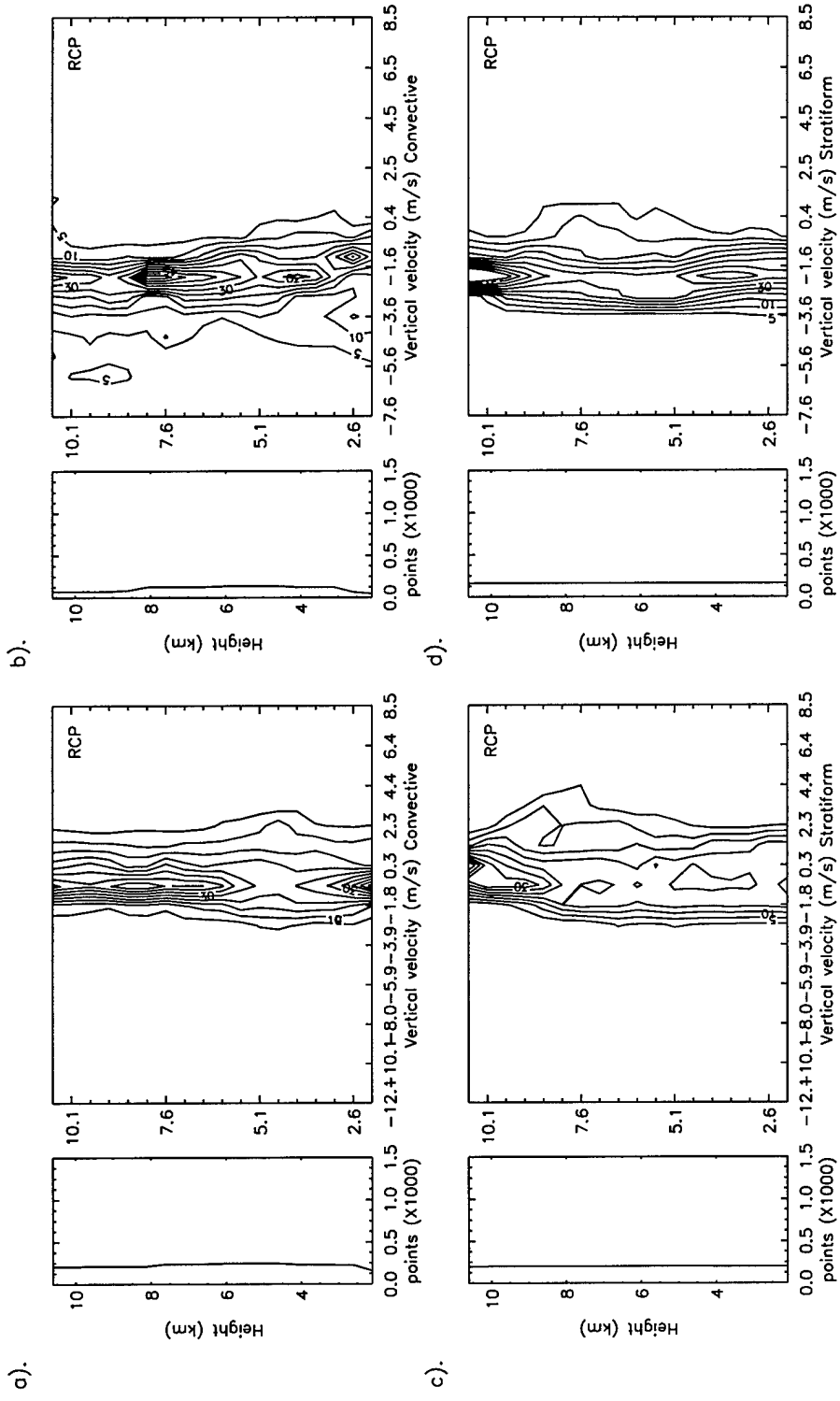

Fig. 41. As in Fig. 18 except for 2211 UTC and 2224 UTC from the 24 May 1997 case.

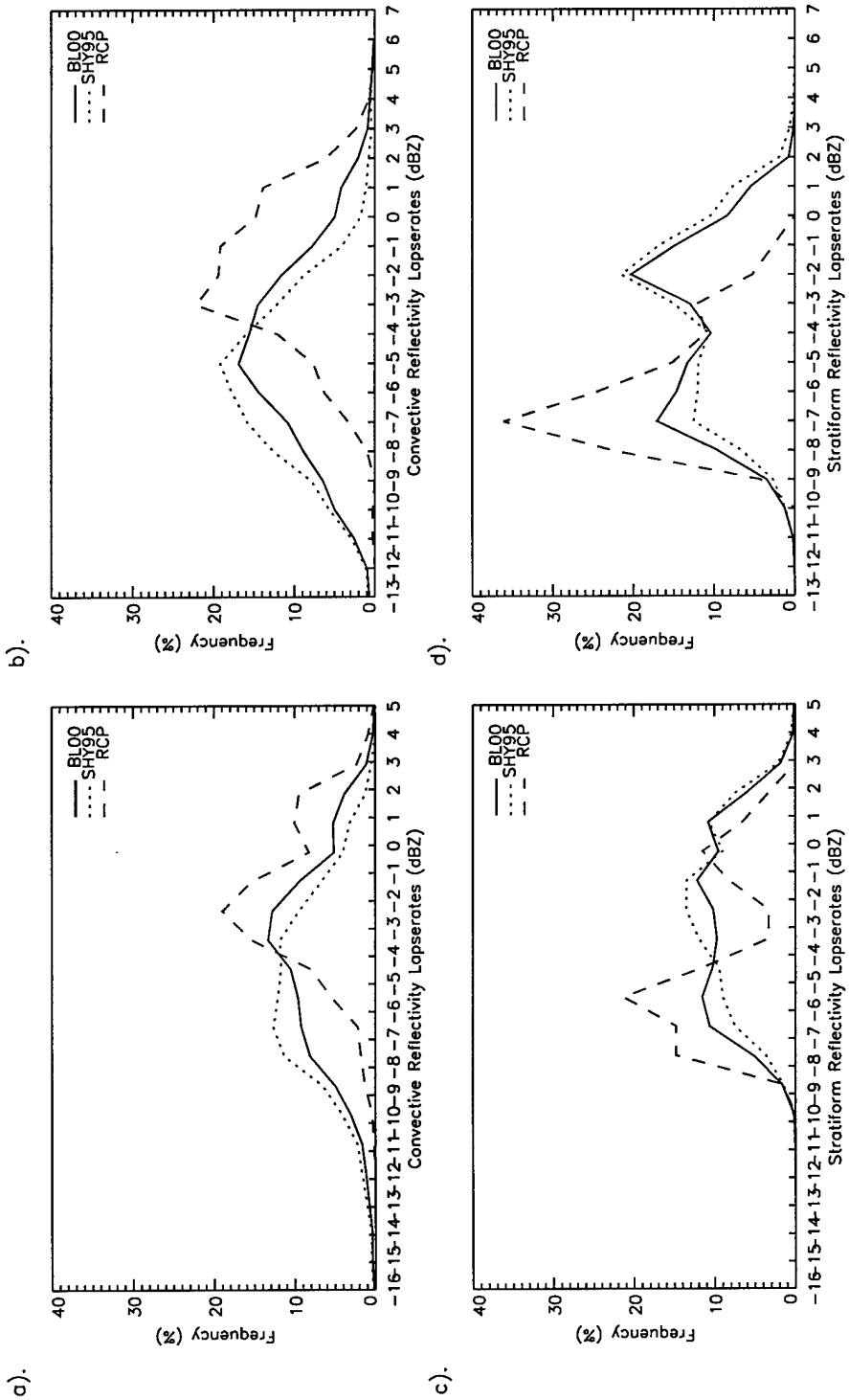

Fig. 42. As in Fig. 20 except for 2013 UTC and 2034 UTC from the 24 May 1997 case.

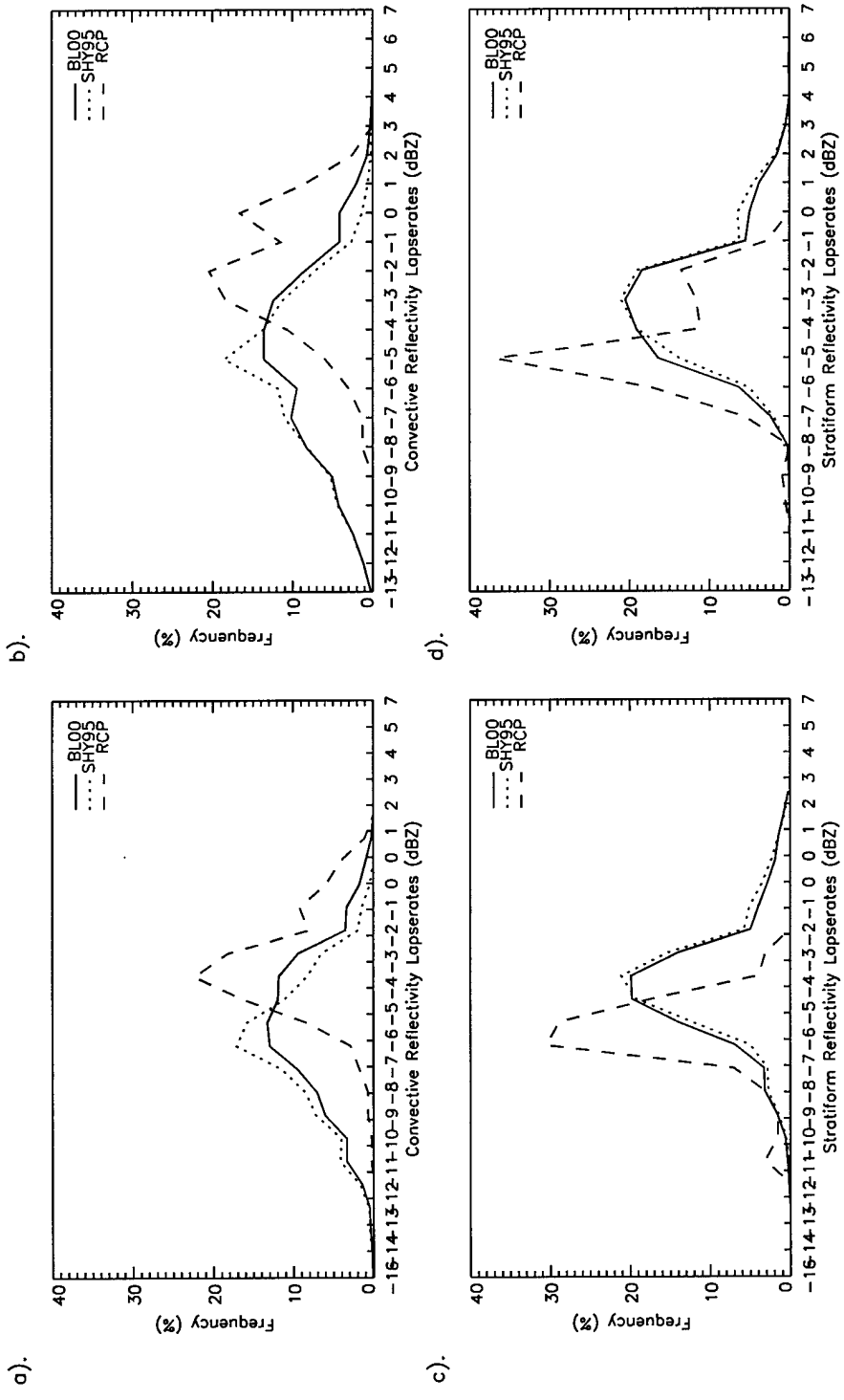

Fig. 43. As in Fig. 20 except for 2123 UTC and 2155 UTC from the 24 May 1997 case.

From figures 42c,d and 43c,d, we can see that the stratiform lapse rate distributions for BL and SHY95 are bimodal with no real differences seen between the two curves. The reclassified points once again have peaks that are shifted to the higher lapse rates, but they are still bimodal in most of the volumes (Figs. 43c,d). From figure 5b, one can see that the points that were reclassified as stratiform are generally located in two locations, one near the bright band and the other near the back edge of the line of convection. The points on the back edge of the convective line could be regions where convective cells are dissipating. This may explain why the reclassified points display a bimodal distribution and would still support the observation that BL does an overall better job in separating the reflectivity field into convective and stratiform regions.

h) Multivolume Profiles, CFADs, and Lapse Rates

For this case, the 2013 and the 2034 UTC volume scans were combined to represent the early stage of the system's evolution and the volume scans from 2058 through 2224 UTC were combined to reflect the mature stage. The deciding factor on when to classify a volume as early or mature was the organization of the convective regions; the volumes where the convection was more organized were considered as mature. The 1853 and 1930 UTC volumes were not used due to the differences in the size of the volumes used at these times.

The multivolume mean profiles generally show the same results as for the individual volume scans (Fig. 44). The CFADs are similar as well with the exception of the stratiform CFAD for the early stage of the system (Fig. 44c). The BL CFAD has a

slightly wider distribution in the low levels. However, the bright band signature is more easily identifiable in the BL curve than in the SHY95.

The multivolume vertical velocity CFADs are more revealing. While the CFADs for the individual volumes were generally the same, the ones for the combined volumes show differences in the shifts in the distributions. BL has distributions that are shifted to smaller velocities in the early stage of the system (Fig. 45a) but the same for the mature stage (Fig. 45b). In the stratiform regions, the BL distribution is shifted to smaller velocities for the early volumes (Fig. 45c) but shifted toward higher velocities for the mature volumes (Fig. 45d).

The lapse rate distributions are as expected for the combined volumes where the reclassified points have distributions that are shifted toward smaller lapse rates for the convective regions and shifted to higher lapse rates for the stratiform regions (not shown).

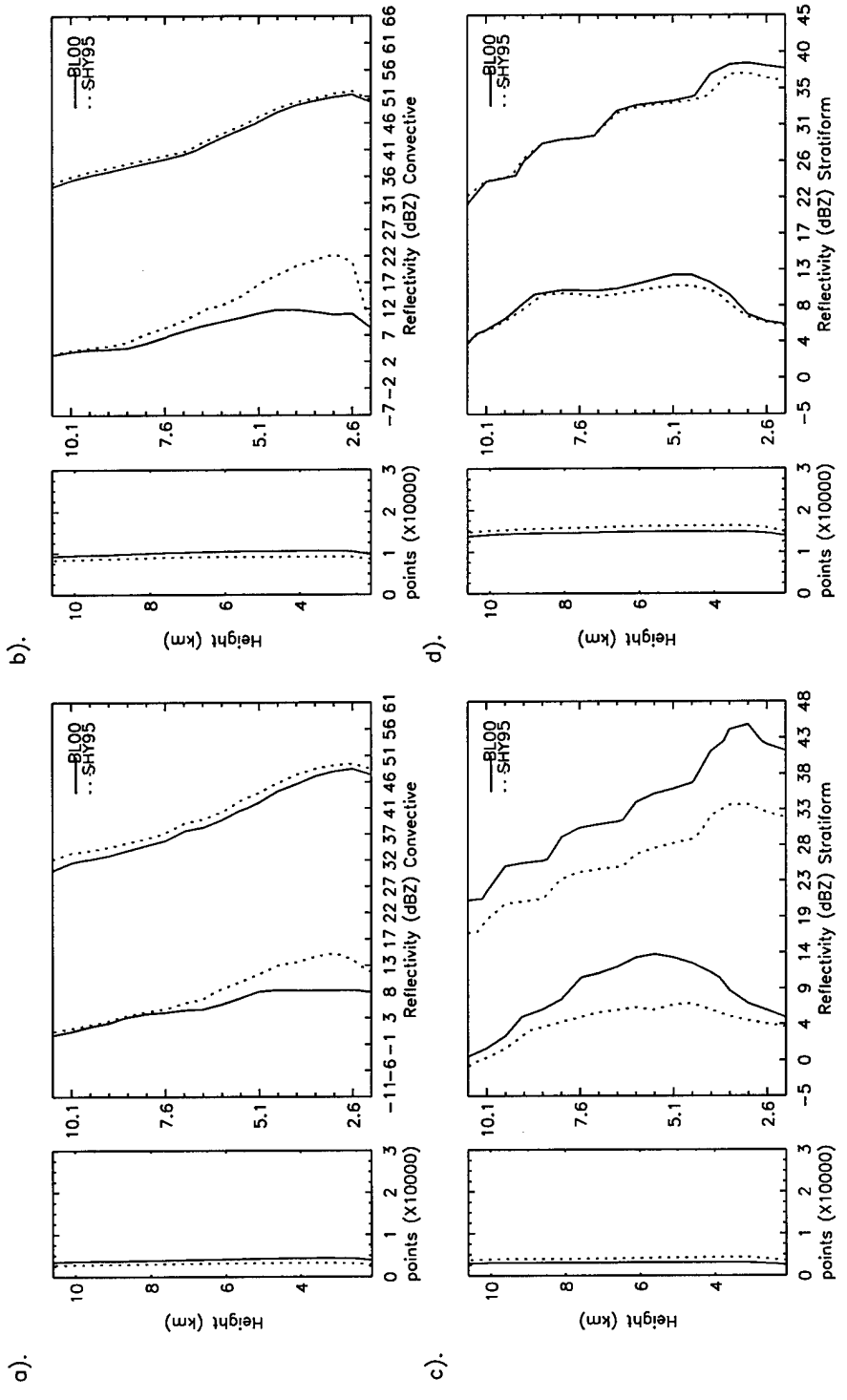

Fig. 44. As in Fig. 16 except for early (left) and mature (right) stages of the 24 May 1997 case.

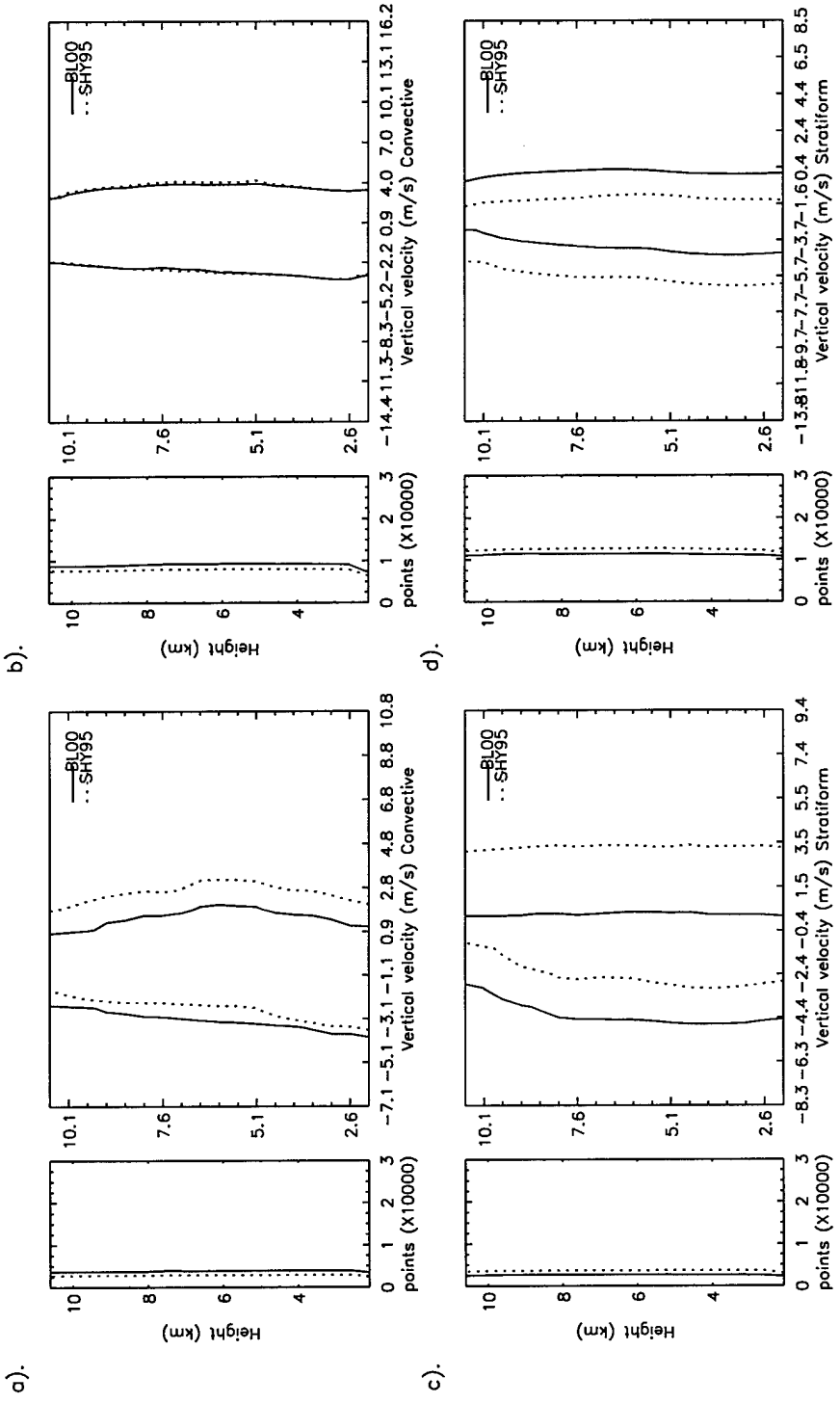

Fig. 45. As in Fig. 18 except for early (left) and mature (right) stages of the 24 May 1997 case.

CHAPTER VIII

A MORE DIFFICULT CASE—THE BOW ECHO

Case 3: The Bow Echo (970617)

The bow echo case presented below is one that is more challenging to decipher. Whereas the previous cases gave results that were more or less expected and easily discernable, this case did not. For the most part, the previous cases represented those that contained a mixture of convective and stratiform regions such that enough points existed for use in generating somewhat representative plots for profiles and CFADs. This case is predominantly convective in nature and makes it more difficult to judge the results, especially for the stratiform regions.

a) Reflectivity Description

This case consists of seven volume scans taken eleven minutes apart. The storm's evolution is displayed using the 3.1 km CAPPIs (Figs. 46 and 47). At 1228 UTC (Fig. 46a), two regions of high reflectivity values (> 50 dBZ) can be found with along a southwest – northeast oriented cold front. With time, the cells in the east move outside of the domain by 1301 UTC (Fig. 46d) while the cell in the west continues to move rapidly to the east away from the cold front. By 1250 UTC (Fig. 46c), this cell

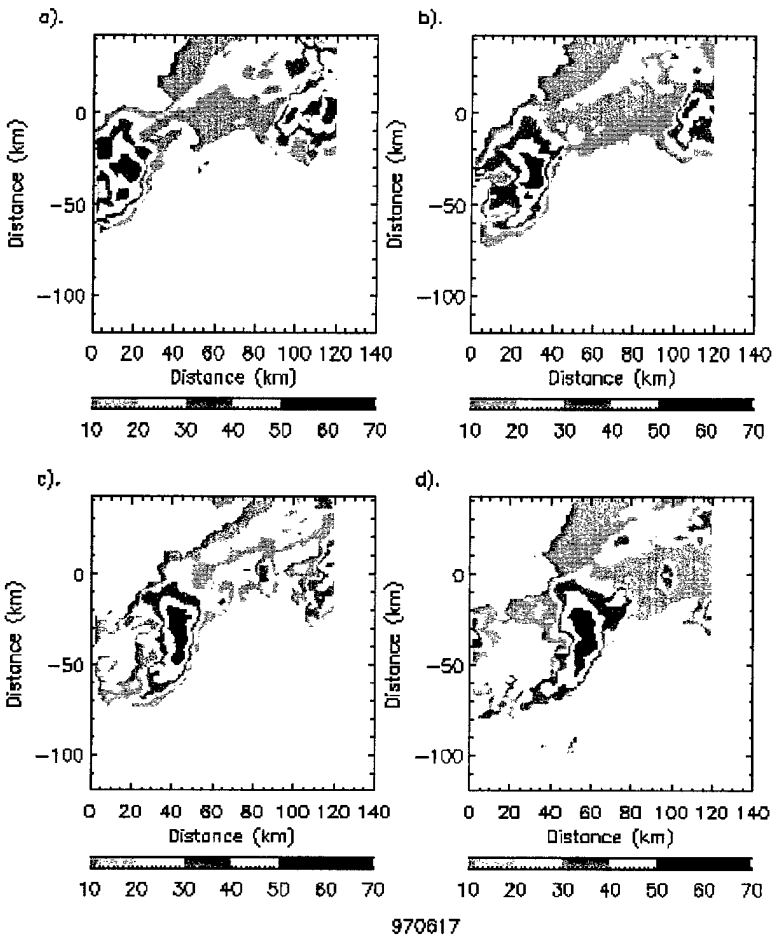

Fig. 46. Same as in Fig. 6 but for the 17 June 1997 case; (a) 1228 UTC, (b) 1239 UTC, (c) 1250 UTC, and (d) 1301 UTC.

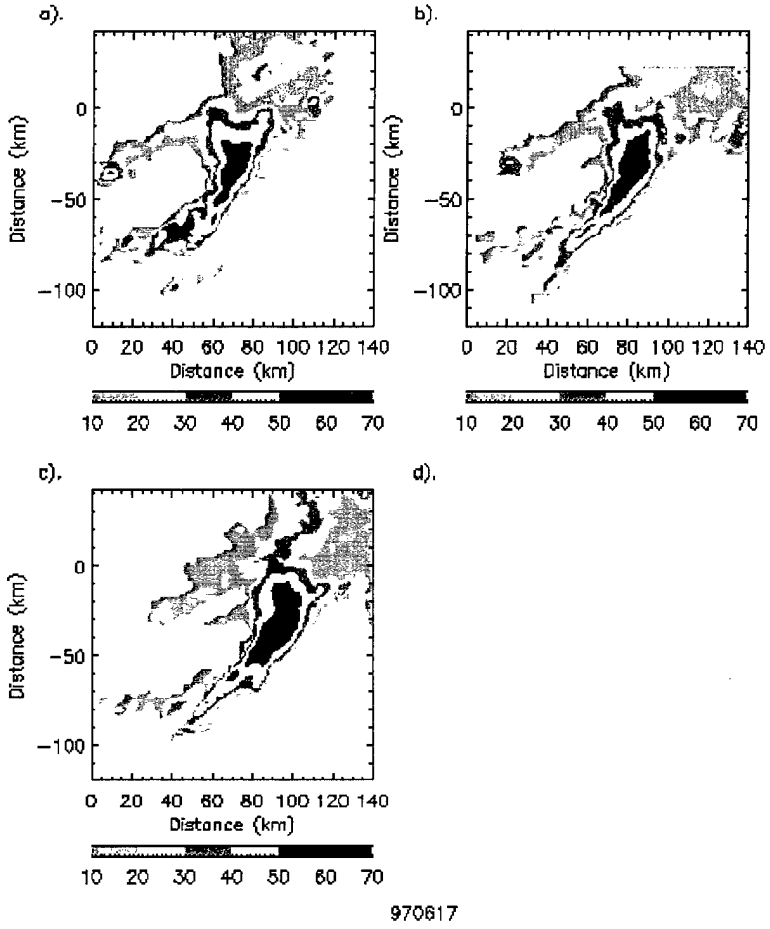

Fig. 47. Same as in Fig. 6 but for the 17 June 1997 case; (a) 1312 UTC, (b) 1323 UTC, and (c) 1334 UTC.

begins to take the shape of a bow and continues to intensify with reflectivities in the 60 – 70 dBZ range near the apex of the bow. By 1334 UTC (Fig. 47c), the system is well developed and has an extensive region of intense reflectivities (> 50 dBZ). As the bow echo developed, reflectivity values associated with weaker convection could be found along the frontal boundary.

b) BL and SHY95 Convective-Stratiform Maps

The convective-stratiform maps for this case do not reveal anything different from the previous cases. The difference maps, like the one shown in Fig. 48b, show that a majority of the reclassification occurred with points that went from stratiform to convective. This resulted from BL extending the convective regions well past the 40 dBZ reflectivity contour (Figs. 48c,d). There are very few areas where points were reclassified as stratiform.

c) Mean Reflectivity Profiles

The convective mean reflectivity profiles for BL and SHY95 closely parallel each other. Like the previous cases, the curves indicate that the highest mean reflectivity values are found in the low levels, but unlike the previous cases, the higher mean reflectivities extend as high as 6 km (Figs. 49a,b). In the earlier volumes, the profiles show a slight increase in the low and mid level mean reflectivities with height. This is consistent with strong storms that are in the developing stage of their life cycle. In the developing stage, the higher reflectivities are first seen in the midlevels. The mean

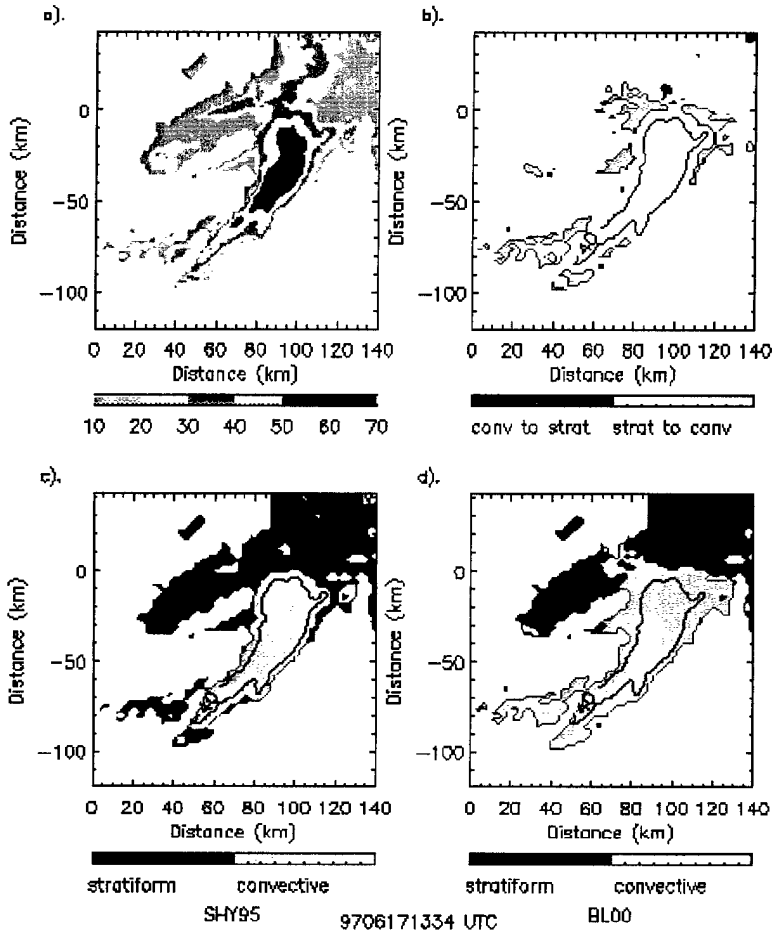

Fig. 48. Same as in Fig. 8 except for 1334 UTC 17 June 1997.

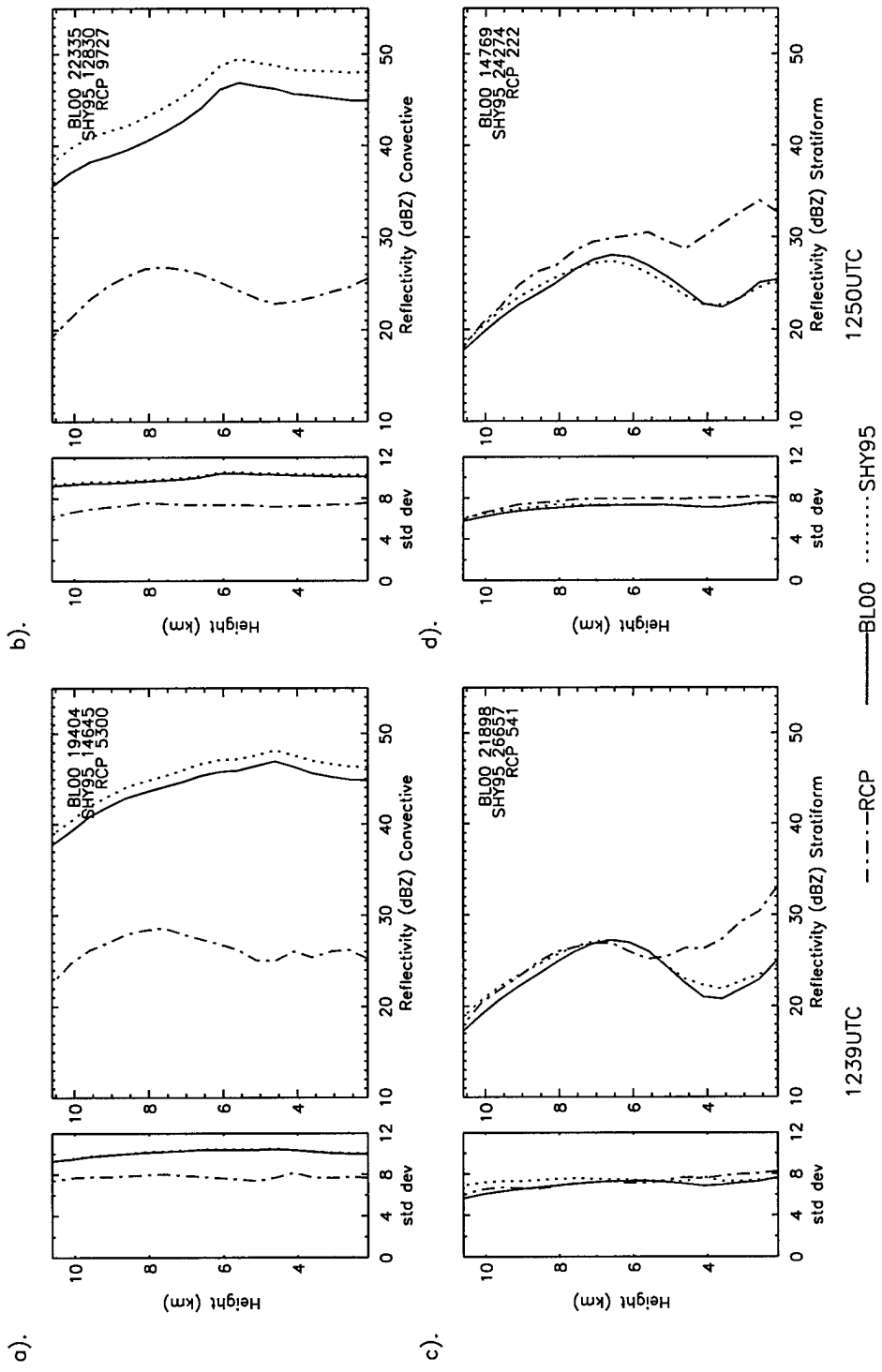

Fig. 49. Same as in Fig. 12 except for 1239 UTC and 1250 UTC of the 17 June 1997 case.

reflectivity profiles for the points that were reclassified as convective by BL are significantly different than the BL and SHY95 profiles. These profiles generally show a decrease in the mean reflectivity with increasing height up to 4 km. Then there is an increase in mean reflectivity with increasing height up to 7 – 8 km followed again by a decrease in mean reflectivity. These mean profiles are also as much as 20 dBZ less than the BL and SHY95 profiles. Because this storm developed in an environment that was very dry in the mid and upper levels, it is believed that the reflectivity bulge seen in the mid levels is an indication that significant evaporation is preventing the precipitation from reaching the surface. If precipitation was reaching the surface in these reclassified regions, one should see significantly higher reflectivity values in the low levels.

The mean reflectivity profiles for the stratiform regions (Figs. 49c,d) exhibit profiles that are similar to the ones generated for the points that were reclassified to convective. This could indicate that these regions are being classified incorrectly as stratiform. Upon closer inspection of the reflectivity CAPPIs for 1239 UTC and 1250 UTC (FIGs. 46b,c), it appears that most of the region that was classified as stratiform is located in the vicinity of the quasi-stationary cold front where elevated convection may have existed. Both algorithms were designed for deep convective systems and appear to have trouble classifying areas of elevated weak convection. This is particularly true for the BL algorithm due to the smoothing effect of the classification window which has a tendency to change narrow embedded lines of convection into stratiform classification.

For the points that were reclassified as stratiform, the mean reflectivity profiles vary in shape from one volume scan to the other. The lack of consistency can be

explained by the fact that few points were reclassified as stratiform and therefore the profiles for these points are of no value.

d) Mean Vertical Velocity Profiles

Both the BL and the SHY95 mean vertical velocity profiles indicate updrafts in the convective regions (Figs. 50a,b). Stronger mean updrafts can be found in the mid to upper levels. At times, the profiles have mean values that are as high as 4 ms^{-1} (3 ms^{-1}) in the SHY95 (BL) profiles (not shown), which is much stronger than shown in the previous two cases. The reclassified points have mean profiles that show weak updrafts at levels below 4 km and weak subsidence above 6 km. This type of profile could be indicative of weak convection. In figure 48c, two regions where points were reclassified as convective can be seen, one region on the northern periphery of the 40 dBZ contour and the other on the southern periphery. The reclassified points on the southern periphery are located where new convection would develop within the bow echo complex. Those in the northern periphery are located in the region where weak convection would be found along the cold frontal boundary.

The stratiform mean vertical velocity profiles indicate very weak subsidence in the low levels and upward vertical motion in the upper levels at 1239 UTC and 1250 UTC (Figs. 50c,d). After this time (not shown), there is net upward vertical motion throughout all the levels with the higher vertical velocities once again found aloft. These profiles are more representative of convection and can be interpreted as BL and SHY95

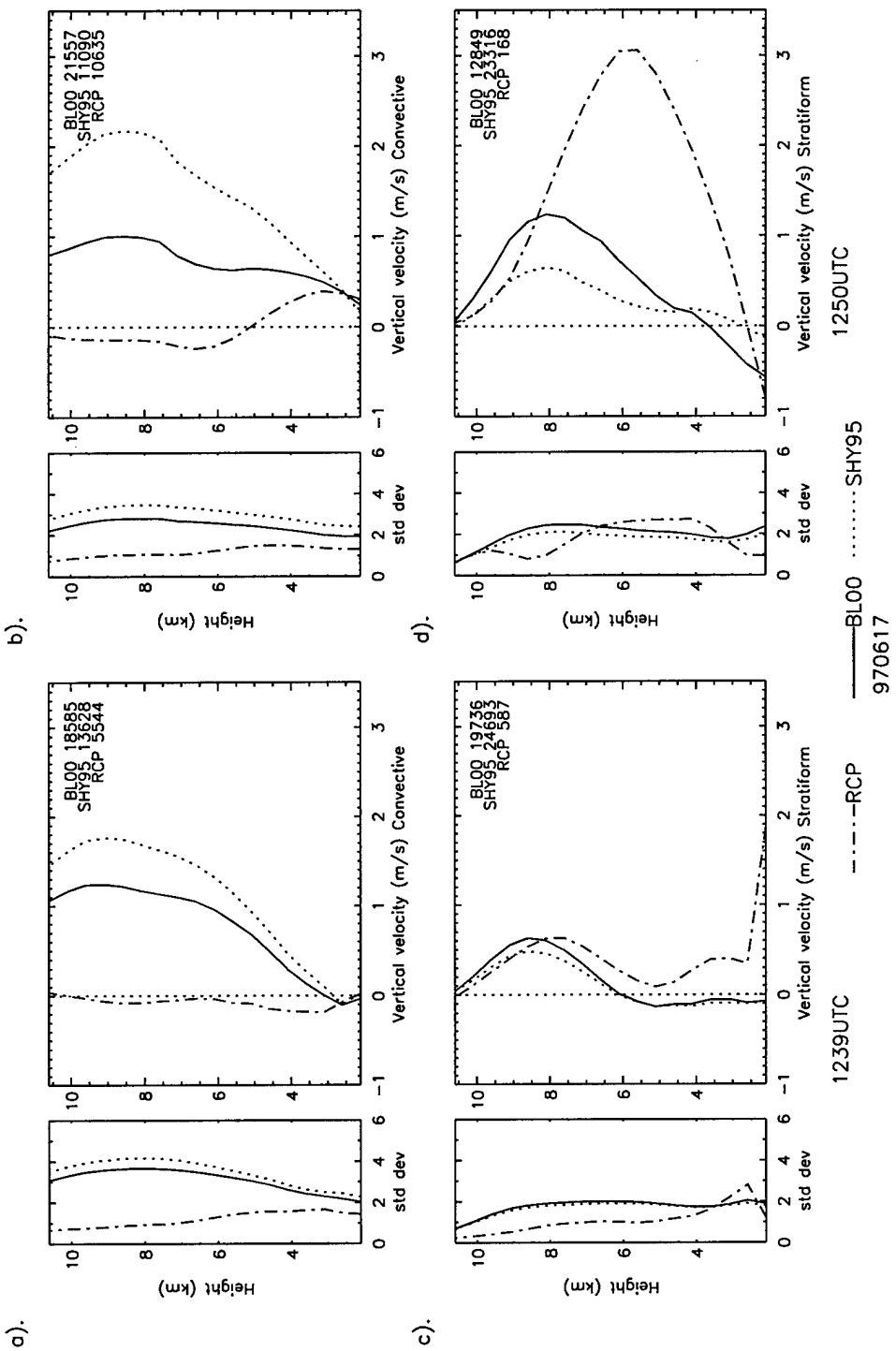

Fig. 50. Same as in Fig. 13 except for 1239 UTC and 1250 UTC of the 17 June 1997 case.

incorrectly classifying the narrow weak convection along the cold frontal boundary as stratiform.

e) Reflectivity CFADs

For the most part, the BL CFADs are as expected with the low level reflectivities having a wider distribution than in the SHY95 CFADs for the convective regions. At 1312 UTC (Fig. 51b), however, the BL CFAD actually has a narrower distribution in the mid levels as seen in the 5% contour that indicates the higher reflectivity values (e.g. the 5% contour on the right side). This is the influence of the weaker reflectivity values associated with convection along the cold front. The CFADs for the stratiform regions (Figs. 51c,d) do not exhibit any noticeable differences although they do have much narrower distributions than seen in the CFADs for the convective regions (Figs. 51a,b). Due to the limited number of points that were classified differently, the CFADs for the reclassified points do not provide any useful information.

f) Vertical Velocity CFADs

No significant differences were noted in the convective CFADs for BL and SHY95 other than that BL sometimes show slightly narrower distributions (Figs. 52a,b). The same can be said of the stratiform CFADs with the only difference found at 1250 UTC (Fig. 52d) where BL has a much wider distribution at 7 km, again a reflection of the weak convection along the cold front. Furthermore, the stratiform distributions were just as wide as the convective distributions.

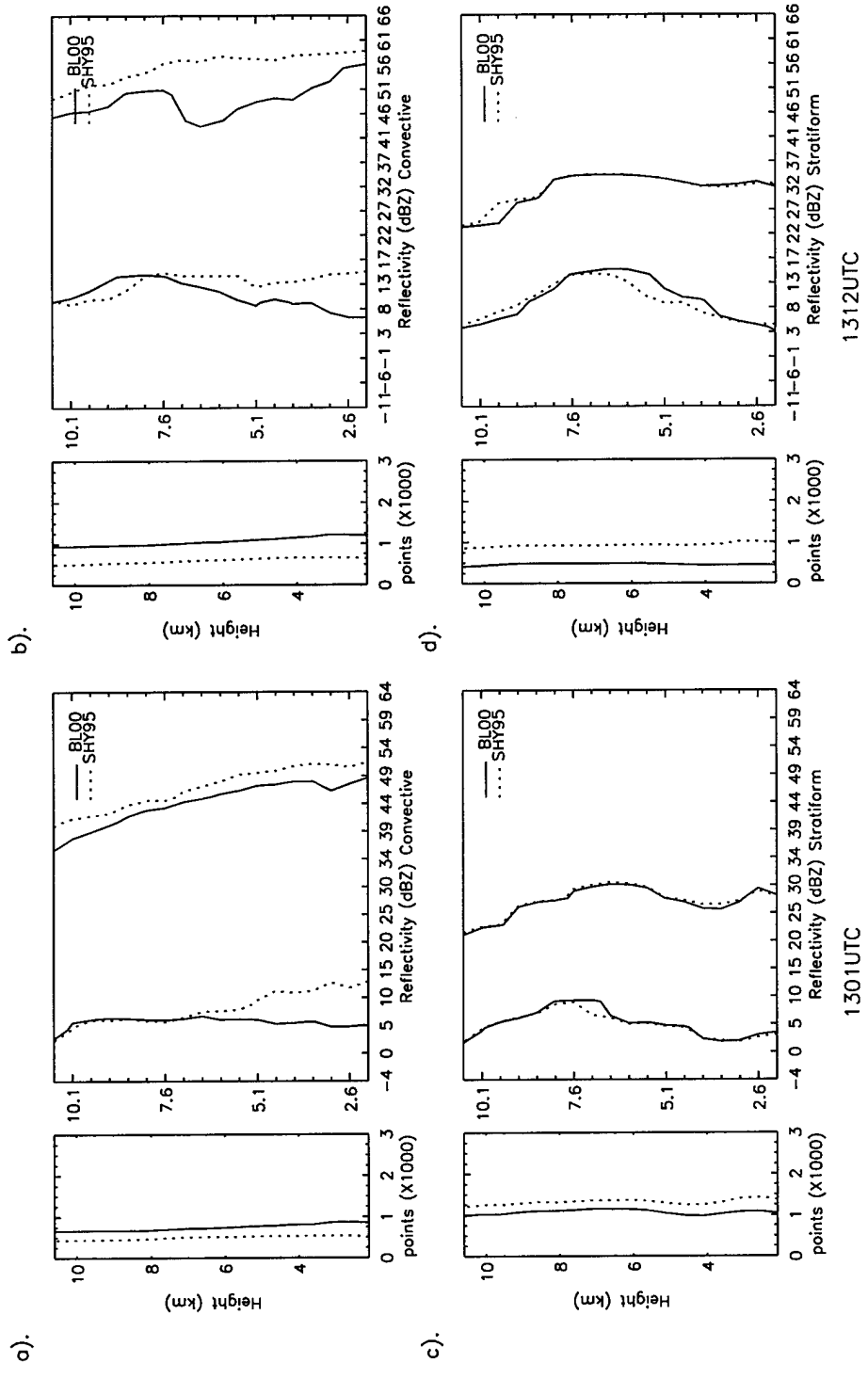

Fig. 51. Same as in Fig. 16 except for 1301 UTC and 1312 UTC of the 17 June 1997 case.

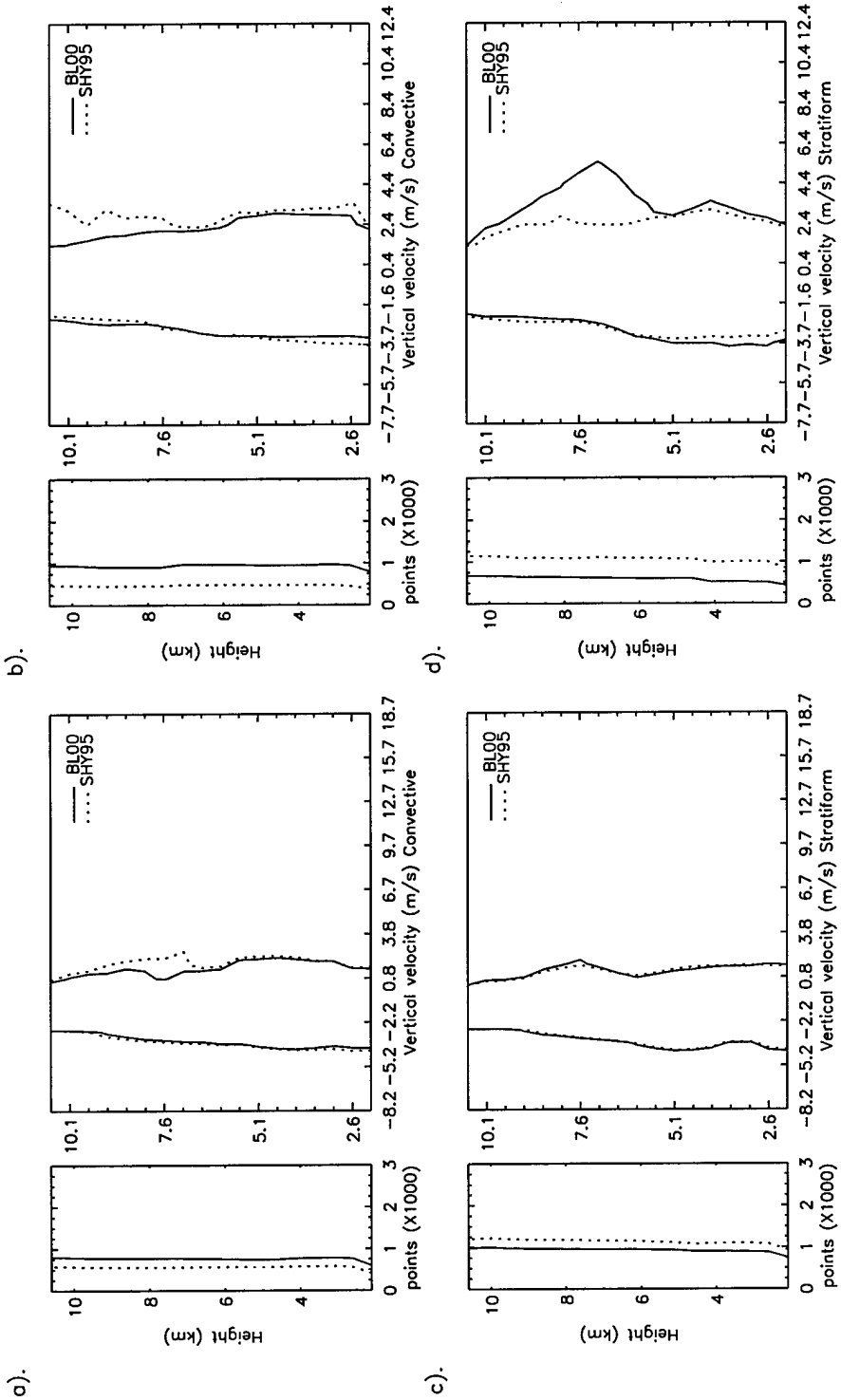

Fig. 52. Same as in Fig. 16 except for 1239 UTC and 1250 UTC of the 17 June 1997 case.

g) Mixed Phase Lapse Rates

Distributions of the mixed phase region lapse rates are shown in figures 53 and 54. In the previous cases, we saw that the 4 – 7 km lapse rates had a near normal unimodal distribution in the convective regions. In this case, however, the distributions are often bimodal which stems from the fact that there are two distinct regions of convection, that associated with the bow echo and that associated with the cold front. The reclassified points have distributions that are bimodal as well but still generally favor lower lapse rates and suggest that these points were correctly reclassified as convective.

For the stratiform regions, BL and SHY95 exhibit very similar distributions that are also bimodal as well (Figs. 53c,d). For these regions, the bimodal distribution shows that BL and SHY95 both classified points as stratiform that probably should have been classified as convection, such as along the cold front.

h) Multivolume Profiles, CFADs, and Lapse Rates

Multivolumes of data were created for this case by combining the volumes from 1228 UTC to 1301 UTC to represent the early stages of the evolution of the bow echo. The mature stage was represented by combining the volumes from 1312 UTC to 1334 UTC where the region enclosed by the 40 dBZ contour doubles in size. The mean profiles, CFADs, and lapse rate distributions generated from these multivolumes fail to reveal any information that is different from that already discussed for the individual volume scans.

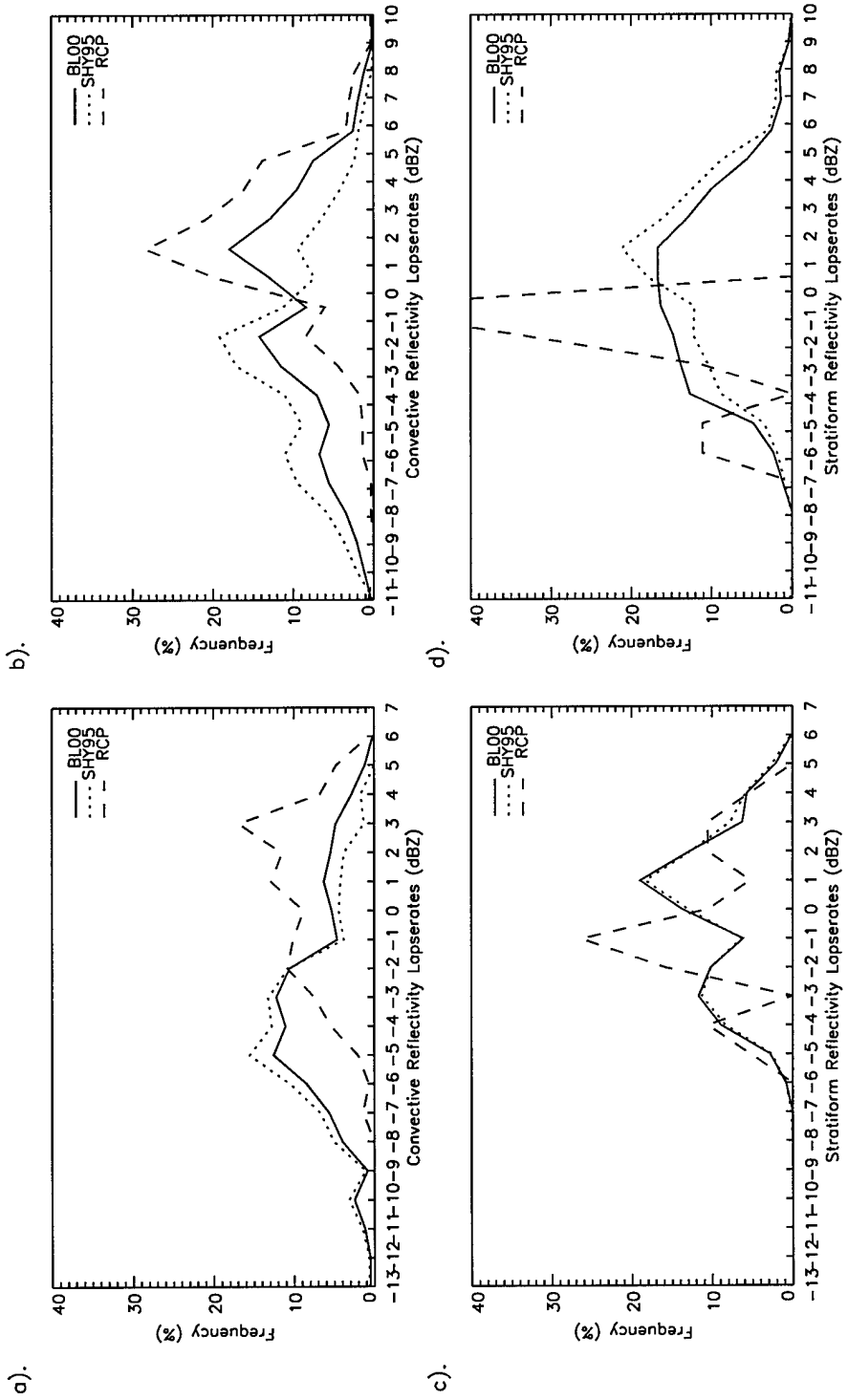

Fig. 53. Same as in Fig. 20 except for 1239 UTC and 1250 UTC of the 17 June 1997 case.

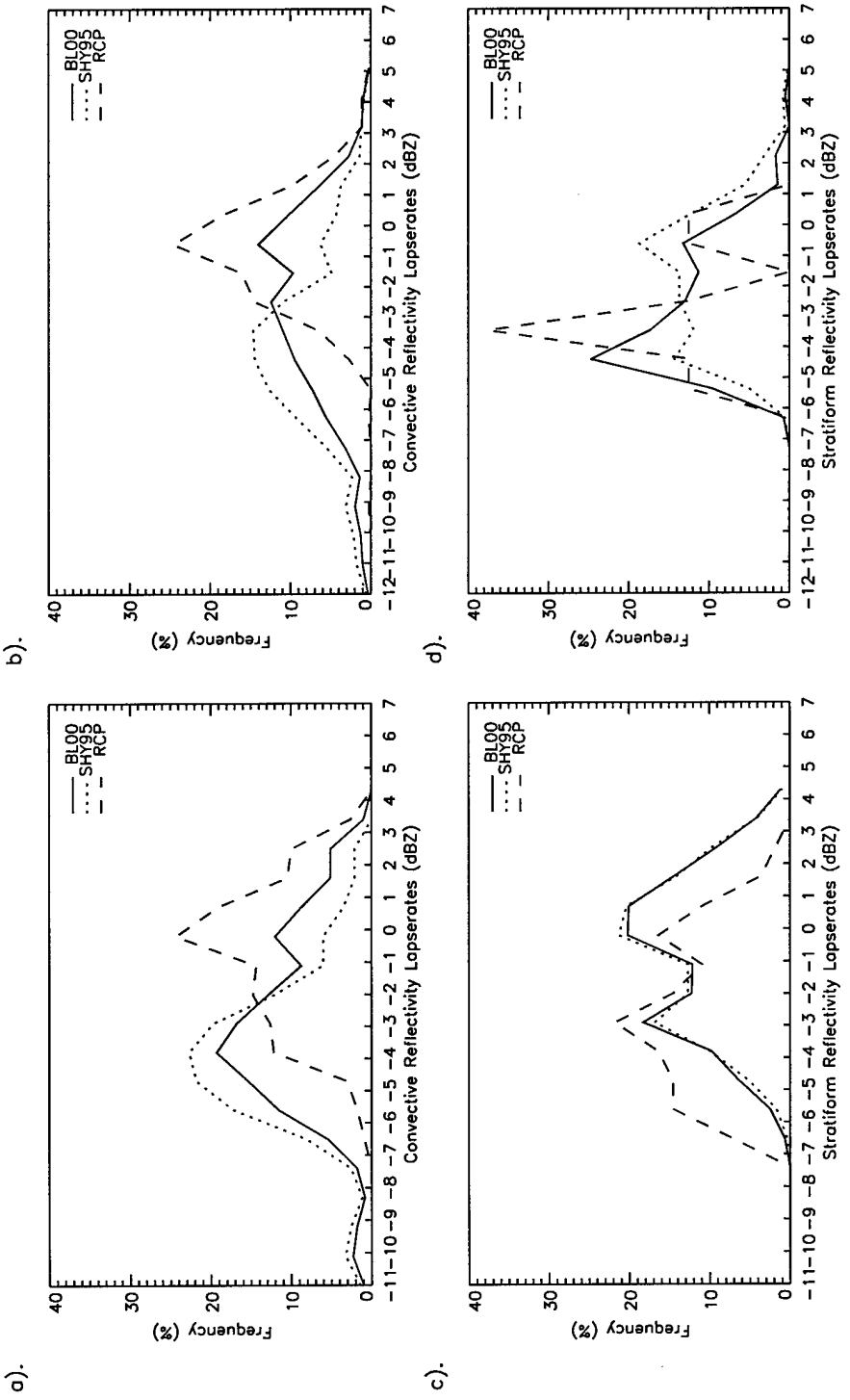

Fig. 54. Same as in Fig. 16 except for 1301 UTC and 1312 UTC of the 17 June 1997 case.

CHAPTER IX

CONCLUSIONS

A validation of two precipitation echo classification schemes was completed using radar reflectivity data and dual-Doppler derived vertical velocity data collected for three separate precipitation systems during a springtime field campaign. The first echo classification technique tested was developed by Steiner et al. (1995) (SHY95) and is currently used in the TRMM project to aid in identifying regions of convective and stratiform precipitation so that better estimates of latent heating can be obtained. Biggerstaff and Listemaa (2000) recently introduced the second algorithm (BL) and argued that it is an improvement over the SHY95 technique. These improvements stem from the fact that BL classifies radar reflectivity echoes based on the three dimensional characteristics of typical precipitation systems. This is substantially different from the SHY95 technique, which classifies echoes based only on the horizontal properties at one level of a system. While preliminary tests indicated that BL is an overall improvement over SHY95, further validation was required.

Validation of the algorithms was performed by first classifying radar reflectivity data using the two algorithms. Convective-stratiform maps were then created to indicate the classification given by the algorithms. These maps were examined and areas where there were differences in classification were noted. Next, separate vertical profiles of mean reflectivity and vertical velocity were created for algorithm assigned convective

and stratiform regions. The profiles based on the BL results were compared to those of the SHY95 results to determine the overall performance. Vertical profiles for the points that were reclassified by BL were also plotted and compared to the convective and stratiform profiles. Contoured frequency by altitude diagrams (CFAD) of reflectivity and vertical velocity were then plotted to verify the performance information obtained from the mean profiles. Finally, the distribution of the 4 – 7 km lapse rate was determined individually for stratiform and convective regions as well as for the points that were reclassified.

The results from this study suggest that, in general, the BL echo classification scheme provides better results than the SHY95 scheme. The SHY95 technique often partitions a precipitation system such that convection is limited to the areas bounded by reflectivity values that are close to 40 dBZ. By limiting convection to these regions, the forward edge of squall line convection is often misclassified as stratiform by SHY95. By taking horizontal reflectivity gradients into consideration, BL is able to extend the regions of convection such that these types of misclassifications are substantially reduced.

Improvements in performance are also seen when classifying regions that contain high reflectivities associated with the bright band. SHY95 classifies these regions as convective. Furthermore, SHY95 often produces a classification in stratiform regions that gives the appearance of the presence of random cores of convection. By including vertical characteristics of precipitation systems, such as vertical lapse rates, BL is able to properly reclassify most of these regions as stratiform.

Even though the BL algorithm is based on the horizontal and vertical characteristics often seen in precipitating systems, it is quite evident that improvements are still needed. For example, this study found that BL experiences difficulty in classifying the back edge of trailing stratiform regions. Furthermore, as in the Biggerstaff and Listemaa study (2000), this study also found that BL has trouble in properly classifying thin lines of convection, especially when the convection is relatively weak or elevated.

It is anticipated that improving the windowing technique used to smooth the classification can eliminate these limitations. It's been suggested that the windowing technique could be made "smarter" by assigning a type of assurance probability to each classified point indicating the level of confidence in the classification assigned at each point. The reclassification that takes place in the smoothing step would then depend on the confidence levels of the points located within the window. These suggested improvements will be the focus of future studies.

REFERENCES

Adler, R. F., and A. J. Negri, 1988: A satellite infrared technique to estimate tropical convective and stratiform rainfall. *J. Appl. Meteor.*, **27**, 30-51.

——, G. J. Huffman, D. T. Bolvin, S. Curtis, and E. J. Nelkin, 2000: Tropical rainfall distributions determined using TRMM combined with other satellite and rain gauge information. J. Appl. Meteor., **39**, 2007-2023.

Anagnostou, E. N., and W. F. Krajewski, 1998: Calibration of the WSR-88D Precipitation Processing Subsystem. *Wea. Forecasting*, **13**, 396–406.

——, and W. F. Krajewski, 1999a: Real-Time Radar Rainfall Estimation. Part I: Algorithm Formulation. *J. Atmos. Oceanic Tech.*, **16**, 189–197.

——, and W. F. Krajewski, 1999b: Real-time radar rainfall estimation. Part II: Case study. *J. Atmos. Oceanic Tech.*, **16**, 198–205.

Atlas, D., and C. W. Ulbrich, 1990: Early foundations of the measurement of rainfall by radar. *Radar in Meteorology*, D. Atlas, Ed., Amer. Meteor. Soc., 806pp.

——, C. W. Ulbrich, F. D. Marks Jr., E. Amitai, and C. R. Williams, 1999: Systematic variation of drop size and radar–rainfall relations. *J. Geophys. Res.*, **104**, 6155–6169.

——, C. W. Ulbrich, F. D. Marks, R. A. Black, E. Amitai, P. T. Willis, and C. E. Samsury, 2000: Partitioning tropical oceanic convective and stratiform rains by draft strenght. *J. Geophys. Res.*, **105**, 2259-2267.

Austin, P. M., 1987: Relation between measured radar reflectivity and surface rainfall. *Mon. Wea. Rev.*, **115**, 1053-1070.

——, and A. C. Bemis, 1950: A quantitative study of the "bright band" in radar precipitation echoes. *J. Meteor.*, **7**, 145-151.

Battan, L. .J., 1973: *Radar Observation of the Atmosphere*. The University of Chicago Press, 324 pp.

Biggerstaff, M. I., and R. A. Houze Jr., 1991: Kinematic and precipitation structure of the 10-11 June 1985 squall line. *Mon. Wea. Rev.,* **119**, 3034-3065.

——, and R. A. Houze Jr., 1993: Kinematic and microphysics of the transition zone of the 10-11 June 1985 squall line. *J. Atmos. Sci.,* **50**, 3091-3110.

——, and S. A. Listemaa, 2000: An improved scheme for convective/stratiform echo classification using radar reflectivity. *J. Appl. Meteor.*, **39**, 2129-2149.

——, J. Guynes, S. Hristova-Veleva, E. Seo, B. Karl, and Coauthors, 1997: The Texas A&M University Convection And Lightning Experiment—TEXACAL 97. Preprints, *28th Conf. on Radar Meteor.*, Austin, TX, Amer. Meteor. Soc., 588-589.

Burgess, D., and P. S. Ray, 1986: Principles of Radar. *Mesoscale Meteorology and Forecasting.* Amer. Meteor. Soc., 793pp.

——, and L.. R. Lemon, 1990: Severe thunderstorm detection by radar. *Radar in Meteorology*, D. Atlas, Ed., Amer. Meteor. Soc., 806pp.

Churchill, D. D., and R. A. Houze Jr., 1984: Development and structure of winter monsoon cloud clusters on 10 December 1978. *J. Atmos. Sci.,* **41**, 933-960.

Crum, T. D., and R. L. Alberty, 1993: The WSR-88D and the WSR-88D Operational Support Facility. *Bull. Amer. Meteor. Soc.,* **74**, 1669–1687.

DeMott, C. A., S. A. Rutledge, 1998: The vertical structure of TOGA COARE convection. Part I: Radar echo distributions. *J. Atmos. Sci.*, **55**, 2730–2747.

——, R. Cifelli., and S. A. Rutledge, 1995: An improved method for partitioning radar data into convective and stratiform components. Preprints, *27th Conf. on Radar. Meteorology*, Vail, CO, Amer. Meteor. Soc., 233-236.

Doviak, R. J., and D. S. Zrnic, 1993: *Doppler Radar and Weather Observations.* Second Edition. Academic Press, 562pp.

Fulton, R. A., 1999: Sensitivity of WSR-88D Rainfall Estimates to the Rain-Rate Threshold and Rain Gauge Adjustment: A Flash Flood Case Study. *Wea. Forecasting*, **14**, 604–624.

——, J. P. Breidenbach, D. Seo, D. A. Miller, and T. O'Bannon, 1998: The WSR-88D rainfall algorithm. *Wea. Forecasting*, **13**, 377–395.

Gamache, J. F., and R. A. Houze Jr., 1982: Mesoscale air motions associated with a tropical squall line. *Mon. Wea. Rev.*, **110**, 118-134.

Glitto, P., and B. Choy, 1997: A Comparison of WSR-88D Storm Total Precipitation Performance during Two Tropical Systems following Changes to the Multiplicative Bias and Upper Reflectivity Threshold. *Wea Forecasting*, **12**, 459–471.

Hong, Y., C. D. Kummerow, and W. S. Olson, 1999: Separation of convective and stratiform precipitation using microwave brightness temperature. *J. Appl. Meteor.*, **38**, 1195-1213.

Houghton, H. G., 1968: On precipitation mechanisms and their artificial modification. *J. Appl. Meteor.*, **7**, 851-859.

Houze, R. A., Jr., 1973: A climatological study of vertical transports by cumulus-scale convection. *J. Atmos. Sci.*, **30**, 1112-1123.

——, 1989: Observed structure of mesoscale convective systems and implications for large-scale heating. *Quart. J. Roy. Meteor. Soc.*, **115**, 425-461.

——, 1993: *Cloud Dynamics*. Academic Press, 573 pp.

——, B. F. Smull, and P. Dodge, 1990: Mesoscale Organization of Springtime rainstorms in Oklahoma. *Mon. Wea. Rev.*, **118**, 613-654.

Johnson R. H., and P. J. Hamilton, 1988: The relationship of surface pressure features to the precipitation and airflow structure of an intense midlatitude squall line. *Mon. Wea. Rev.*, **116**, 1444-1472.

Joss, J., 1990: Precipitation measurement and hydrology. *Radar in Meteorology*. D. Atlas, Ed., Amer. Meteor. Soc., 806pp.

Kummerow, C., I. M. Hakkarinen, H. F. Pierce, and J. A. Weinman, 1991: Determination of precipitation profiles from airborne passive microwave radiometric measurements. *J. Atmos. Oceanic Tech.*, **8**, 148-158.

——, W. Barnes, T. Kozu, J. Shiue, and J. Simpson, 1998: The Tropical Rainfall Measuring Mission (TRMM) sensor package. *J. Atmos. Oceanic Tech.,* **15**, 809-817.

——, J. Simpson, O. Thiele, W. Barnes, A. T. C. Chang, 2000: The status of the Tropical Rainfall Measuring Mission (TRMM) after two years in orbit. *J Appl Meteor.*, **39**, 1965–1982.

Marks, D.A., M.S. Kulie, M. Robinson, B. S. Ferrier, and E. Amitai, 1999: Standardized reference rainfall products used in TRMM Ground Validation. Preprints, *29th Conference on Radar Meteorology*, Montreal, Quebec, Canada, Amer. Met. Soc., 744-747.

Mohr, C. G., and R.L.. Vaughn, 1979: An economical procedure for Cartesian interpolation and display or reflectivity factor data in three-dimensional space. *J. Appl. Meteor.*, **18**, 661-670.

——, and L.. J. Miller, 1983: CEDRIC – A software package for Cartesian space editing, synthesis and display of radar fields under interactive control. Preprints, *21st Conf. on Radar Meteorology*, Edmonton, Canada, Amer. Meteor. Soc., 559-574.

Oye, R., and R. E. Carbone, 1981: Interactive Doppler editing software. Preprints, *20th Conf. on Radar Meteorology*, Boston, MA, Amer. Meteor. Soc. 683-689.

Pereira, A. J., K. C. Crawford, and C. L.. Hartzell, 1998: Improving WSR-88D hourly rainfall estimates. *Wea. and Forecast.,* **13**, 1016-1028.

Rinehart, R. E., 1997: *RADAR for Meteorologists*. Third Edition. Rinehart Publications, 428 pp.

Rosenfeld, D., E. Amitai, and D. B. Wolff, 1995a: Classification of rain regimes by the three-dimensional properties of reflectivity fields. *J. Appl. Meteor.,* **34**, 198-211.

——, E. Amitai, and D. B. Wolff, 1995b: Improved accuracy of radar WPMM estimated rainfall upon application of objective classification criteria. *J. Appl. Meteor.,* **34**, 212-223.

Schumacher, C. and R. A. Houze, Jr., 2000: Comparison of radar data from the TRMM satellite and Kwajalein Oceanic Validation Site. *J. Appl. Meteor.*, **39**, 2151–2164.

Shelton-Mur, K. J., 1998: Radar reflectivity-rainrate relationships using the classified window probability matching method. M.S. thesis, Dept. of Meteorology, Texas A&M University, 116 pp.

Simpson, J., R. F. Adler, and G. R. North, 1988: A proposed Tropical Rainfall Measuring Mission (TRMM) satellite. *Bull. Amer. Met. Soc.*, **69**, 278-295.

Steiner, M., and R. A. Houze, Jr., 1993: Three-dimensional validation at TRMM ground truth sites: Some early results from Darwin, Australia. Preprints, *26th Conf. on Radar Meteorology*, Norman, OK, Amer. Meteor. Soc., 417-420.

——, and R. A. Houze, Jr., 1997: Sensitivity of the estimated monthly convective rain fraction to the choice of Z-R relation. *J. Appl. Meteor.*, **36**, 452-462.

——, R. A. Houze, Jr., and S. E. Yuter, 1995: Climatological characterization of three-dimensional storm structure from operational radar and rain guage data. *J. Appl., Meteor.*, **34**, 1978-2007.

Tao, W. K., S. Lang, J. Simpson, and R. Adler, 1993: Retrieval algorithms for estimating the vertical profiles of latent heat release: Their applications for TRMM. *J. Meteor. Soc. Japan.*, **71**, 685-699.

Tokay, A.., and D. A. Short, 1996: Evidence from tropical raindrop spectra of the origin of rain from stratiform versus convective clouds. *J. Appl. Meteor.*, **35**, 355-371.

——, D. A. Short, C. R. Williams, W. L. Ecklund, and K. S. Gage, 1999: Tropical rainfall associated with convective and stratiform clouds: Intercomparison of disdrometer and profiler measurements. *J. Appl. Meteor.*, **38**, 302-320.

Tuttle, A., and M. I. Biggerstaff, 1997: *The Texas A&M University Convection and Lightning Experiment (TEXACAL 1997).* Texas A&M University, Department of Meteorology.

Vieux, B. E., and P. B. Bedient, 1998: Estimation of Rainfall for Flood Prediction from WSR-88D Reflectivity: A Case Study, 17–18 October 1994*. *Wea. Forecasting*, **13**, 407–415.

Williams, C.R., W. L. Ecklund, and K. S. Gage, 1995: Classification of precipitating clouds in the tropics using 915-MHz wind profilers. *J. Atmos. Oceanic Tech.,* **12**, 996-1012.

Yuter, S. E., and R. A. Houze Jr., 1995a: Three-dimensional kinematic and microphysical evolution of Florida cumulonimbus. Part I: Spatial distribution of updrafts, downdrafts, and precipitation. *Mon. Wea. Rev.,* **123**, 1921–1940.

——, and R. A. Houze Jr., 1995b: Three-dimensional kinematic and microphysical evolution of Florida cumulonimbus. Part II: Frequency distributions of vertical velocity, reflectivity, and differential reflectivity. *Mon. Wea. Rev.,* **123**, 1941–1963.

Zawadzki, I., 1984: Factors affecting the precision of radar measurements of rain. Preprints, *22nd Conf on Radar Meteorology*, Zurich, Switzerland. Amer. Meteor. Soc., 251-256.

APPENDIX A

ALGORITHM SOURCE CODE

The following is a copy of the source code used in the echo classification algorithm. The original version was developed by Steven Listemaa, a former Texas A&M graduate student, and was later modified by Gordon Carrie, a member of the Mesoscale Research Group at Texas A&M University. The version that follows is Mr Carrie's modified version written in the C programming language.

```
/ * YAVOTMA - Yet Another Version Of The Modified Algorithm
 * Runs the Steiner-Houze-Yuter 1995 and Biggerstaff-Listemaa 2000
 * convective-stratiform separation schemes on a dual-Doppler volume
 * created by cedric.
 *
 * USAGE: yavotma fieldName inFile outFile
  * fieldName should identify a reflectivity field inFile is the name of the input file.
  * Upon successful completion, outFile will be an ascii file that looks like:
 *
 * imax=### jmax=###
 *
 * wl
 * value value value ...
 * value value value ...
 *
 * stein_res
 * value value value ...
 * value value value ...
 *
 * result_final
 * value value value ...
 * value value value ...
 *
 * diff
 * value value value ...
 * value value value ...
 *
 *
 * where value is a grid point value for the listed field.
 * The fields are described below.
 *
```

```
*************************************************************************
* References:
*   Steiner, Houze, Yuter.  J Appl Met. 1995.  (SHY95)
*   Biggerstaff, Listemaa.  J Appl Met. 2000.  (BL00)
*
*/
#include <stdio.h>
#include <stdlib.h>
#include <math.h>
#include <limits.h>
#include "fld.h"

#define RAD_PER_DEG 0.0174532925199

/* Use Cedric (mudhouse) input */
#include "readmud.h"
#define READFLD readmud

/*************************************************************************/
/*Variable and function declarations*/
/*
 * Classification values:
 * UNK = unknown
 * STR = stratiform
 * CNV = convective
 */
typedef enum CLASS {UNK, STR, CNV} CLASS;

/ * Results of reclassification (go into diff)
 *   UNK_STR - unknown became stratiform
 *   UNK_CNV - unknown became convective
 *   STR_CNV - stratiform became convective
 *   STR_UNK - stratiform became unknown
 *   CNV_UNK - convective became unknown
 *   CNV_STR - convective became stratiform
 *   NOCHG   - no change
 */
enum CHANGE {NOCHG, CNV_STR, STR_CNV, UNK_STR, UNK_CNV,
STR_UNK, CNV_UNK};

/* Global functions */
float OrigRange(int i, int j, struct fld fld);
```

```
float Range(int i0, int j0, int i1, int j1, struct fld fld);
int IMin(int i, int j);
int IMax(int i, int j);
int **Alloc2DInt(int jmax, int imax);
CLASS **Alloc2DClass(int jmax, int imax);
float **Alloc2DFloat(int jmax, int imax);
void PrintFArr(FILE *fl, char *hdr, float **arr, int jmax, int imax, char *fmt);
void PrintIArr(FILE *fl, char *hdr, int **arr, int jmax, int imax, char *fmt);
void PrintClassArr(FILE *fl, char *hdr, CLASS **arr, int jmax, int imax);

int main(int argc, char *argv[])
{
 char *progNm = argv[0];
 char
  *fldNm,                    /* Name of field */
  *inFlNm,                   /* Name of mudhouse input file */
  *outNm;                    /* Name of output file */
 FILE *in;                   /* Input file */
 FILE *outf;                 /* Output file */
 struct fld *fld;            /* header and data from mudhouse file */
 float ***Z;                 /* field values from mudhouse file */
 int kmax, jmax, imax;              /* Number of grid points */
 float *z, *y, *x;           /* Coordinate values */
 float dz, dy, dx;           /* Distances between grid points (km) */
 float dz2;                  /* Distances between grid two points (km) */

 /* Loop indeces */
 int i, ii, j, jj, k;
 int n, e, s, w; /* North, east, south, west */

 /* Loop bounds for rectangle around grid point */
 int iimin, iimax, jjmin, jjmax;

 /* Working level array */
 int
  kLo,              /* Working level index for near points */
  kHi;              /* Working level index for far points */
 float wl_rng;              /* Boundary between near and far (km) */
 float
  **wl,                     /* Working level values (decibels) */
  **wl_lin;                 /* wl in linear units. */

 /* Lapse rate */
```

```
float maxv;             /* Max value seen so far in a search */
int k_maxval;                   /* Index of level with max value */
int k0, k1;             /* Levels for computing lapse rate */
int **maxZ_k;                   /* max dBZ height (index) */
float
 **maxZ_hgt,                    /* max dBZ height (km) */
 **maxZ_val,                    /* max dBZ value */
 **mdZdz;               /* reflectiviy lapse rate. */

/* Horizontal gradient */
float dZdx, dZdy;       /* d(field) / dx, d(field) / dy */
float **gradhZ;         /* horizontal dBZ gradients. */

/* Peakedness calculation */
int bg_dj, bg_di;       /* gridpts used for background reflectivity */
int cv_dj, cv_di;       /* gridpts used for convection radius */
int bg_count;           /* Number of points used in background calc */
float conv_radius;      /* Convective radius (km) */
float bg_z;             /* Background value */
float conv_peak;        /* Intensity dependent peakedness threshold */
CLASS **stein_res;      /* original Steiner class map. */
CLASS **stein_40;       /* new Steiner class map. */
CLASS **stein_temp;             /* SHY95 before conv radius test. */
CLASS **stein_temp2;            /* SHY95 before conv radius test. */

/* Bright band fraction */
float bbf_rng;          /* Range for BBF calculation */
int bbf_dj, bbf_di;     /* Num pts in square used in BBF calculation */
float area;             /* Area around point for bbf calc (km^2) */
int numpoints;          /* Number of points in area */
int cntBB, cntPt, usePt;/* Counters for bright band points */
float **bbf;            /* bright-band fraction. */

/* Biggerstaff Listemaa reclassification */
CLASS **result;         /* initial classification map. */
CLASS **result_final;           /* final classification map. */
int **diff;             /* stein_res - result. */
int **out;              /* step where yavotma exited loop. */

/* Grid windowing parameters. BL00, p. 2136. */
int
 point,                 /* Hold opposite of grid point value */
 win_count,             /* Num pts in window area with different val */
```

```
  win_total;                    /* Num pts in window area */

/*********************************************************************/
/*MAIN PROGRAM*/

 /* Parse command line */
 if (argc != 4) {
  fprintf(stderr, "Usage: %s fieldName inFile outFile\n", progNm);
  exit(-1);
 }
 fldNm = argv[1];
 inFlNm = argv[2];
 outNm = argv[3];

 /* Set parameters */
 fprintf(stderr, "Assuming one radar at origin\n");
 kLo = 3;                       /* Working level index for near points */
 kHi = 6;                       /* Working level index for far points */
 wl_rng = 80.0;                 /* Boundary between near and far (km) */
 bbf_rng = 7.0;                 /* Range for BBF calculation (km)*/

 /* Read cedric "mudhouse" file */
 if ( !(in = fopen(inFlNm, "r")) ) {
  fprintf(stderr, "%s ERROR: cannot open %s", progNm, inFlNm);
  exit(-1);
 }
 if ( !(fld = readmud(fldNm, in, NULL)) ) {
  fprintf(stderr, "%s ERROR: could not read field %s from %s\n",
    progNm, fldNm, inFlNm);
  exit(-1);
 }
 fclose(in);
 Z = fld->f;

 /* Get dimension information */
 kmax = fld->kmax;
 jmax = fld->jmax;
 imax = fld->imax;
 dz = fld->dz;
 dy = fld->dy;
 dx = fld->dx;
 dz2 = 2.0 * dz;
```

```
/* Allocate float arrays of dimension [jmax][imax] */
 if (   !(gradhZ = Alloc2DFloat(jmax, imax))
    || !(wl = Alloc2DFloat(jmax, imax))
    || !(maxZ_hgt = Alloc2DFloat(jmax, imax))
    || !(maxZ_val = Alloc2DFloat(jmax, imax))
    || !(mdZdz = Alloc2DFloat(jmax, imax))
    || !(wl_lin = Alloc2DFloat(jmax, imax))
    || !(bbf = Alloc2DFloat(jmax, imax))

    || !(maxZ_k = Alloc2DInt(jmax, imax))
    || !(diff = Alloc2DInt(jmax, imax))
    || !(out = Alloc2DInt(jmax, imax))

    || !(stein_res = Alloc2DClass(jmax, imax))
    || !(stein_40 = Alloc2DClass(jmax, imax))
    || !(stein_temp = Alloc2DClass(jmax, imax))
    || !(stein_temp2 = Alloc2DClass(jmax, imax))
    || !(result = Alloc2DClass(jmax, imax))
    || !(result_final = Alloc2DClass(jmax, imax)) ) {
  fprintf(stderr, "%s ERROR: memory allocation failed for %d by %d arrays\n",
    progNm, imax, imax);
  exit(1);
 }

 /* Coordinate values */
 z = fld->z;
 y = fld->y;
 x = fld->x;

 /* Initialize some arrays */
 fprintf(stderr, "%s: Initializing arrays...  ", progNm);

 /********* End of declarations *********/

 /* Initialize arrays */
 for (j = 0; j < jmax; ++j) {
  for (i = 0; i < imax; ++i) {

    /* Initialize Steiner arrays */
```

```
    stein_res[j][i] = STR;
    stein_40[j][i] = STR;
    stein_temp[j][i] = UNK;
    stein_temp2[j][i] = UNK;

    /* Working level value (set to bad value if Z is bad) */
    if (OrigRange(i, j, *fld) < wl_rng)
      wl[j][i] = fisok(Z[kLo][j][i]) ? Z[kLo][j][i] : badf();
    else
      wl[j][i] = fisok(Z[kHi][j][i]) ? Z[kHi][j][i] : badf();

    /* Working level linear value */
    if ( fisok(wl[j][i]) )
      wl_lin[j][i] = (wl[j][i] <= 0.0) ? 0.0 : pow(10.0, 0.1 * wl[j][i]);
    else
      wl_lin[j][i] = badf();

    /* Find level with maximum value */
    for (k = 0, k_maxval = 0, maxv = -FLT_MAX; k < kmax; ++k) {
      if (fisok(Z[k][j][i]) && Z[k][j][i] > maxv) {
        k_maxval = k;
          maxv = Z[k][j][i];
        }
    }
    if (k_maxval == kmax - 1) k_maxval = 0; /* Uniform column */
    maxZ_hgt[j][i] = fisok(Z[k_maxval][j][i]) ? z[k_maxval] : badf();
    maxZ_val[j][i] = fisok(Z[k_maxval][j][i]) ? Z[k_maxval][j][i] : badf();
    maxZ_k[j][i] = k_maxval;

    /* Compute "lapse rate" = -df/dz */
    k0 = k_maxval;
    k1 = IMin(k_maxval + 6, kmax - 1);      /* Don't go over the top */
    if ( fisok(Z[k0][j][i]) && fisok(Z[k1][j][i]) )
      mdZdz[j][i] = -(Z[k1][j][i] - Z[k0][j][i]) / (z[k1] - z[k0]);
    else
      mdZdz[j][i] = badf();
  }
 }
 fprintf(stderr, "Done.\n");

/ * Magnitude of horizontal gradient.  Do center differences when possible,
  * else do forward or backward differences, else gradient is undefined
  */
```

```
for (j = 1; j < jmax - 1; j++) {

 /* West side */
 n = fisok(wl[j+1][0]) ? j+1 : fisok(wl[j][0]) ? j : -1;
 s = fisok(wl[j-1][0]) ? j-1 : fisok(wl[j][0]) ? j : -1;
 dZdy = (n != -1 && s != -1 && n != s)
        ? (wl[n][0] - wl[s][0]) / (y[n] - y[s])
          : badf();
 dZdx = (fisok(wl[j][1]) && fisok(wl[j][0]))
        ? (wl[j][1] - wl[j][0]) / (x[1] - x[0])
          : badf();
 if (fisok(dZdy) && fisok(dZdx))
  gradhZ[j][0] = sqrt(dZdx * dZdx + dZdy * dZdy);
 else if (fisok(dZdy))
  gradhZ[j][0] = fabs(dZdy);
 else if (fisok(dZdx))
  gradhZ[j][0] = fabs(dZdx);
 else
  gradhZ[j][0] = badf();

 /* East side */
 n = fisok(wl[j+1][imax-1]) ? j+1 : fisok(wl[j][imax-1]) ? j : -1;
 s = fisok(wl[j-1][imax-1]) ? j-1 : fisok(wl[j][imax-1]) ? j : -1;
 dZdy = (n != -1 && s != -1 && n != s)
        ? (wl[n][imax-1] - wl[s][imax-1]) / (y[n] - y[s])
          : badf();
 dZdx = (fisok(wl[j][imax-2]) && fisok(wl[j][imax-1]))
        ? (wl[j][imax-1] - wl[j][imax-2]) / (x[imax-1]-x[imax-2])
          : badf();
 if (fisok(dZdy) && fisok(dZdx))
  gradhZ[j][imax-1] = sqrt(dZdx * dZdx + dZdy * dZdy);
 else if (fisok(dZdy))
  gradhZ[j][imax-1] = fabs(dZdy);
 else if (fisok(dZdx))
  gradhZ[j][imax-1] = fabs(dZdx);
 else
  gradhZ[j][imax-1] = badf();

 /* Interior */
 for (i = 1; i < imax - 1; i++) {
  n = fisok(wl[j+1][i]) ? j+1 : fisok(wl[j][i]) ? j : -1;
  s = fisok(wl[j-1][i]) ? j-1 : fisok(wl[j][i]) ? j : -1;
  dZdy = (n != -1 && s != -1 && n != s)
```

```
            ? (wl[n][i] - wl[s][i]) / (y[n] - y[s])
               : badf();
    e = fisok(wl[j][i+1]) ? i+1 : fisok(wl[j][i]) ? i : -1;
    w = fisok(wl[j][i-1]) ? i-1 : fisok(wl[j][i]) ? i : -1;
    dZdx = (e != -1 && w != -1 && e != w)
            ? (wl[j][e] - wl[j][w]) / (x[e] - x[w])
               : badf();
    if (fisok(dZdy) && fisok(dZdx))
      gradhZ[j][i] = sqrt(dZdx * dZdx + dZdy * dZdy);
    else if (fisok(dZdy))
      gradhZ[j][i] = fabs(dZdy);
    else if (fisok(dZdx))
      gradhZ[j][i] = fabs(dZdx);
    else
      gradhZ[j][i] = badf();
  }
}

for (i = 1; i < imax - 1; i++) {

  /* North side */
  dZdy = (fisok(wl[jmax-1][i]) && fisok(wl[jmax-2][i]))
          ? (wl[jmax-1][i] - wl[jmax-2][i]) / (y[jmax-1] - y[jmax-2])
             : badf();
  e = fisok(wl[jmax-1][i+1]) ? i+1 : fisok(wl[jmax-1][i]) ? i : -1;
  w = fisok(wl[jmax-1][i-1]) ? i-1 : fisok(wl[jmax-1][i]) ? i : -1;
  dZdx = (e != -1 && w != -1 && e != w)
          ? (wl[jmax-1][e] - wl[jmax-1][w]) / (x[e] - x[w])
             : badf();
  if (fisok(dZdy) && fisok(dZdx))
    gradhZ[jmax-1][i] = sqrt(dZdx * dZdx + dZdy * dZdy);
  else if (fisok(dZdy))
    gradhZ[jmax-1][i] = fabs(dZdy);
  else if (fisok(dZdx))
    gradhZ[jmax-1][i] = fabs(dZdx);
  else
    gradhZ[jmax-1][i] = badf();

  /* South side */
  dZdy = (fisok(wl[1][i]) && fisok(wl[0][i]))
          ? (wl[1][i] - wl[0][i]) / (y[1] - y[0])
             : badf();
  e = fisok(wl[0][i+1]) ? i+1 : fisok(wl[0][i]) ? i : -1;
```

```
 w = fisok(wl[0][i-1]) ? i-1 : fisok(wl[0][i]) ? i : -1;
 dZdx = (e != -1 && w != -1 && e != w)
        ? (wl[0][i+1] - wl[0][i-1]) / (x[i+1] - x[i-1])
          : badf();
 if (fisok(dZdy) && fisok(dZdx))
   gradhZ[0][i] = sqrt(dZdx * dZdx + dZdy * dZdy);
 else if (fisok(dZdy))
   gradhZ[0][i] = fabs(dZdy);
 else if (fisok(dZdx))
   gradhZ[0][i] = fabs(dZdx);
 else
   gradhZ[0][i] = badf();

}

/* SW corner */
dZdy = (fisok(wl[1][0]) && fisok(wl[0][0]))
       ? (wl[1][0] - wl[0][0]) / (y[1] - y[0])
         : badf();
dZdx = (fisok(wl[0][1]) && fisok(wl[0][0]))
       ? (wl[0][1] - wl[0][0]) / (x[1] - x[0])
         : badf();
if (fisok(dZdy) && fisok(dZdx))
  gradhZ[0][0] = sqrt(dZdx * dZdx + dZdy * dZdy);
else if (fisok(dZdy))
  gradhZ[0][0] = fabs(dZdy);
else if (fisok(dZdx))
  gradhZ[0][0] = fabs(dZdx);
else
  gradhZ[0][0] = badf();

/* NW corner */
dZdy = (fisok(wl[jmax-1][0]) && fisok(wl[jmax-2][0]))
       ? (wl[jmax-1][0] - wl[jmax-2][0]) / (y[jmax-1] - y[jmax-2])
         : badf();
dZdx = (fisok(wl[jmax-1][1]) && fisok(wl[jmax-1][0]))
       ? (wl[jmax-1][1] - wl[jmax-1][0]) / (x[1] - x[0])
         : badf();
if (fisok(dZdy) && fisok(dZdx))
  gradhZ[jmax-1][0] = sqrt(dZdx * dZdx + dZdy * dZdy);
else if (fisok(dZdy))
  gradhZ[jmax-1][0] = fabs(dZdy);
else if (fisok(dZdx))
```

```
  gradhZ[jmax-1][0] = fabs(dZdx);
 else
  gradhZ[jmax-1][0] = badf();

 /* NE corner */
 dZdy = (fisok(wl[jmax-1][imax-1]) && fisok(wl[jmax-2][imax-1]))
        ? (wl[jmax-1][imax-1] - wl[jmax-2][imax-1]) / (y[jmax-1] - y[jmax-2])
          : badf();
 dZdx = (fisok(wl[jmax-1][imax-2]) && fisok(wl[jmax-1][imax-1]))
        ? (wl[jmax-1][imax-1] - wl[jmax-1][imax-2]) / (x[imax-1] - x[imax-2])
          : badf();
 if (fisok(dZdy) && fisok(dZdx))
  gradhZ[jmax-1][imax-1] = sqrt(dZdx * dZdx + dZdy * dZdy);
 else if (fisok(dZdy))
  gradhZ[jmax-1][imax-1] = fabs(dZdy);
 else if (fisok(dZdx))
  gradhZ[jmax-1][imax-1] = fabs(dZdx);
 else
  gradhZ[jmax-1][imax-1] = badf();

 /* SE corner */
 dZdy = (fisok(wl[1][imax-1]) && fisok(wl[0][imax-1]))
        ? (wl[1][imax-1] - wl[0][imax-1]) / (y[1] - y[0])
          : badf();
 dZdx = (fisok(wl[0][imax-2]) && fisok(wl[0][imax-1]))
        ? (wl[0][imax-1] - wl[0][imax-2]) / (x[imax-1] - x[imax-2])
          : badf();
 if (fisok(dZdy) && fisok(dZdx))
  gradhZ[0][imax-1] = sqrt(dZdx * dZdx + dZdy * dZdy);
 else if (fisok(dZdy))
  gradhZ[0][imax-1] = fabs(dZdy);
 else if (fisok(dZdx))
  gradhZ[0][imax-1] = fabs(dZdx);
 else
  gradhZ[0][imax-1] = badf();

 /* Done with gradient */

/* Size of area for background reflectivity calculation */
 bg_dj = (int)(11.0 / dy + 0.5);
 bg_di = (int)(11.0 / dx + 0.5);

 fprintf(stderr, "%s: Classifying grid points... ", progNm);
```

```
for (j = 0; j < jmax; ++j) {
 for (i = 0; i < imax; ++i) {

  /* Steiner classification */
  if (fisbad(wl[j][i]) || wl[j][i] <= 10.0) {



    /* Do not perform Steiner classification in low reflectivity areas */
   stein_40[j][i] = UNK;
   stein_res[j][i] = UNK;

  } else {

   /* Reflectivity sufficient for Steiner classification */

    /* Compute background.  wl_lin is never negative, so I don't know what
     * the third comparison is for.  GDC */
   bg_z = 0.0;
   bg_count = 0;
     jjmin = IMax(j - bg_dj, 0);
     jjmax = IMin(j + bg_dj, jmax);
     iimin = IMax(i - bg_di, 0);
     iimax = IMin(i + bg_di, imax);
   for (jj = jjmin; jj < jjmax; jj++) {
    for (ii = iimin; ii < iimax; ii++) {
     if (  Range(i, j, ii, jj, *fld) <= 11.0
           && fisok(wl_lin[jj][ii]) && wl_lin[jj][ii] > 0.0) {
       bg_z = bg_z + wl_lin[jj][ii];
       ++bg_count;
     }
    }
   }
   if(bg_count <= 0) {
      /* No data in the background around point */
    fprintf(stderr, "%s WARNING: No background around j = %d i = %d\n",
            progNm, j, i);
    stein_temp = UNK;
    stein_temp2 = UNK;
   } else {
    bg_z = 10.0 * log10(bg_z / bg_count);
```

```
        /* Intensity dependent peakedness threshold
         * Partly based on Steiner, et al. 1995.  Eq. 2 */
        conv_peak = (bg_z < 0.0) ? 10.0 : 10.0 - bg_z * bg_z / 180.0;
        conv_peak = (conv_peak < 0.0) ? 0.0 : conv_peak;  /* nonnegative */

        /* Convection radius */
            if (bg_z >= 40.0) conv_radius = 5.0;
        else if (bg_z >= 35.0) conv_radius = 4.0;
        else if (bg_z >= 30.0) conv_radius = 3.0;
        else if (bg_z >= 25.0) conv_radius = 2.0;
        else conv_radius = 1.0;

        /* Loop limits for applying convective radius */
        cv_dj = (int)(conv_radius / dy + 0.5);
        cv_di = (int)(conv_radius / dx + 0.5);
        jjmin = IMax(j - cv_dj, 0);
        jjmax = IMin(j + cv_dj, jmax);
        iimin = IMax(i - cv_di, 0);
        iimax = IMin(i + cv_di, imax);

/* Peakedness test without 40 dBZ criterion. */
        stein_40[j][i]
            = fisbad(wl[j][i])
              ? UNK : (wl[j][i] - bg_z >= conv_peak) ? CNV : STR;
        if (stein_40[j][i] == CNV) {
            /* Make points within convection radius of j,i
             * convective as well.  Store in stein_temp. */
            for (jj = jjmin; jj < jjmax; jj++) {
              for (ii = iimin; ii < iimax; ii++) {
                if (   Range(i, j, ii, jj, *fld) <= conv_radius
                       && fisok(wl_lin[jj][ii]) && wl_lin[jj][ii] > 0.0) {
                stein_temp[jj][ii] = CNV;
                }
              }
            }
        }

        /* Peakedness test with 40 dBZ criteria */
        stein_res[j][i]
            = fisbad(wl[j][i])
              ? UNK : (wl[j][i] >= 40.0 || (wl[j][i] - bg_z >= conv_peak))
                ? CNV : STR;
```

```
  if (stein_res[j][i] == CNV) {
      /* Make points within convection radius of j,i
       * convective as well.  Store in stein_temp2. */
    for (jj = jjmin; jj < jjmax; jj++) {
     for (ii = iimin; ii < iimax; ii++) {
      if (   Range(i, j, ii, jj, *fld) <= conv_radius
              && fisok(wl_lin[jj][ii]) && wl_lin[jj][ii] > 0.0) {
       stein_temp2[jj][ii] = CNV;
      }
     }
    }
   }
    }

}   /* end if wl > 10.0.  end of Steiner block. */

/*
 * Compute bright band fraction (BBF) using the Biggerstaff Listemaa
 * method.
 * Area for BBF calculation depends on distance to origin (assumed to be
 * location of radar).
 * A point i,j contributes to BBF if
 *   wl[j][i] > 10.0 AND 2.5 <= maxZ_hgt <= 5.5 AND mdfdbz > 3.5
 */

/* Area of 7 km by 11 degree pie slice */
area = 7.0 * 11.0 * RAD_PER_DEG * OrigRange(i, j, *fld);

/* Square with the same area as the pie slice */
numpoints = sqrt(area) / dy;
bbf_dj = (int)(numpoints / 2.0 + 0.5);
bbf_di = bbf_dj;

/* Limits for loop around point */
cntBB = 0;
cntPt = 0;
usePt = 0;
jjmin = IMax(j - bbf_dj, 0);
jjmax = IMin(j + bbf_dj, jmax);
iimin = IMax(i - bbf_di, 0);
iimax = IMin(i + bbf_di, imax);
for (jj = jjmin; jj < jjmax; jj++) {
 for (ii = iimin; ii < iimax; ii++) {
```

```
      if (  fisok(wl[jj][ii]) && fisok(maxZ_hgt[jj][ii])
            && fisok(mdZdz[jj][ii]) ) {
          usePt++;
       if (  wl[jj][ii] > 10.0
          && maxZ_hgt[jj][ii] >= 2.5 && maxZ_hgt[jj][ii] <= 5.5
             && mdZdz[jj][ii] > 3.5
             && Range(i, j, ii, jj, *fld) <= bbf_rng) {
        cntBB++;
       }
        }
      cntPt++;
     }
    }
    bbf[j][i] = (usePt == 0) ? badf()
                      : (cntPt == 0) ? 0
                                     : cntBB / (float)cntPt;

  }     /* end for i */
}       /* end for j */
/* Done with Steiner and BBF calculations at each grid point */

/* Put stein_temp's into stein's */
for (j = 0; j < jmax; j++) {
  for (i = 0; i < imax; i++) {
    if (stein_temp[j][i] == CNV) stein_40[j][i] = CNV;
    if (stein_temp2[j][i] == CNV) stein_res[j][i] = CNV;
  }
}
fprintf(stdout, "Done.\n");

/*
 * Perform Biggerstaff Listemaa partitioning.  See BL00 p 2136.
 *
 * The out matrix determines where in the loop the partition at
 *    that point was changed.
 */

fprintf(stderr, "%s: Adjusting classification... ", progNm);
for (j = 0; j < jmax; ++j) {
  for (i = 0; i < imax; ++i) {
    k = maxZ_k[j][i];
    if (maxZ_k[j][i] < 6) k += 6;
    out[j][i] = 0;
```

```
if (fisbad(wl[j][i]) || wl[j][i] < 10.0) {
    /* Low reflectivity and bad areas always unknown */
 result[j][i] = UNK;
 stein_res[j][i] = UNK;
 stein_40[j][i] = UNK;
} else if (stein_40[j][i] == CNV) {
    /* Reclassify convective point */
 if (  fisok(gradhZ[j][i]) && gradhZ[j][i] < 3.0
       && fisok(mdZdz[j][i]) && mdZdz[j][i] > 3.5
       && fisok(wl[j][i]) && wl[j][i] < 35.0) {
  result[j][i] = STR;
  out[j][i] = 1;
 } else if (
         fisok(Z[k][j][i]) && Z[k][j][i] < 28.0
    && fisok(gradhZ[j][i]) && gradhZ[j][i] < 3.0
    && fisok(mdZdz[j][i]) && mdZdz[j][i] > 3.5
       && fisok(bbf[j][i]) && bbf[j][i] >= 0.60) {
  result[j][i] = STR;
  out[j][i] = 2;

    /*
    Not in published version
 } else if (
         fisok(bbf[j][i]) && bbf[j][i] >= 0.60
    && fisok(gradhZ[j][i]) && gradhZ[j][i] < 3.0
    && fisok(Z[k][j][i]) && Z[k][j][i] < 28.0
       && fisok(wl[j][i]) && wl[j][i] < 35.0
    && fisok(mdZdz[j][i]) && mdZdz[j][i] > 3.5) {
  result[j][i] = STR;
  out[j][i] = 3;
    */

 } else {
  result[j][i] = CNV;
 }
} else if (stein_40[j][i] == STR) {
    /* Reclassify stratiform point */
 if (fisok(gradhZ[j][i]) && gradhZ[j][i] >= 3.0) {
  result[j][i] = CNV;
  out[j][i] = 4;

    /*
    Not in published version
```

```
    } else if (
            fisok(bbf[j][i]) && bbf[j][i] < 0.40
          && fisok(Z[k][j][i]) && Z[k][j][i] >= 28.0
        && fisok(Z[k][j][i]) && mdZdz[j][i] <= 3.5
          && fisok(gradhZ[j][i]) && gradhZ[j][i] >= 1.0) {
     result[j][i] = CNV;
     out[j][i] = 5;
      */

    } else if (
            fisok(gradhZ[j][i]) && gradhZ[j][i] > 2.0
          && fisok(bbf[j][i]) && bbf[j][i] < 0.40) {
     result[j][i] = CNV;
     out[j][i] = 6;
    } else {
     result[j][i] = STR;
    }
   } else {
    /* No classification */
    result[j][i] = UNK;
   }
  }     /* end for i */
}       /* end for j */

/*
 * Next pass through the grid applies grid point windowing.
 *
 * point takes on the value opposite of result[a][b]...i.e.
 * if result[a][b]==1, then point = 2.  Thus, win_count will be
 * the total number of points that have values not equal to
 * result[a][b] and percent will be the percent of points
 * not having result[a][b]'s value.
 */

for (j = 0; j < jmax; ++j) {
 for (i = 0; i < imax; ++i) {

   if (result[j][i] == UNK) {
    result_final[j][i] = UNK;
   } else {
      point = (result[j][i] == STR) ? CNV : STR;
    win_count = 0;
    win_total = 0;
```

```
    /* Loop limits for grid windowing (we must ensure in domain) */
    jjmin = IMax(j - 8, 0);
    jjmax = IMin(j + 8, jmax);
    iimin = IMax(i - 8, 0);
    iimax = IMin(i + 8, imax);
  for (jj = jjmin; jj < jjmax; jj++) {
   for (ii = iimin; ii < iimax; ii++) {
    if (result[jj][ii] != UNK) {
     win_total++;
     if (result[jj][ii] == point)
      win_count++;
    }
   }
  }

  result_final[j][i]
      = ((float)win_count / win_total >= 0.55) ? point : result[j][i];
} /* end if result != UNK */

/* Record how result changed with reclassification
 * Record in the form of AAA_BBB where AAA is what
 * the SHY95 algorithm classified the point as and
 * the BBB is what the BL algorithm changed the
 * classification to.  For example, a diff value of
 * STR_CNV implies that SHY classified the point as
 * STRATIFORM but the BL algorithm changed it to
 * CONVECTIVE*/
if (result_final[j][i] == UNK && stein_res[j][i] == STR) {
  diff[j][i] = STR_UNK;
} else if (result_final[j][i] == UNK && stein_res[j][i] == CNV) {
    diff[j][i] = CNV_UNK;
} else if (result_final[j][i] == STR && stein_res[j][i] == CNV) {
    diff[j][i] = CNV_STR;
} else if (result_final[j][i] == STR && stein_res[j][i] == UNK) {
    diff[j][i] = UNK_STR;
} else if (result_final[j][i] == CNV && stein_res[j][i] == UNK) {
    diff[j][i] = UNK_CNV;
} else if (result_final[j][i] == CNV && stein_res[j][i] == STR) {
    diff[j][i] = STR_CNV;
} else {
  diff[j][i] = NOCHG;
}
```

```
  } /* end for i */
 } /* end for j */
 fprintf(stderr, "Done.\n");

 /* Send output */
 fprintf(stderr, "%s: Sending output to %s... ", progNm, outNm);
 if ( !(outf = fopen(outNm, "w")) ) {
  fprintf(stderr, "%s ERROR: Could not open %s for output.\n", progNm, outNm);
  exit(1);
 }
 fprintf(outf, "imax=%3d jmax=%3d\n", imax, jmax);
 PrintFArr(outf, "\nwl", wl, jmax, imax, "%3g ");
 PrintFArr(outf, "\ngradhZ", gradhZ, jmax, imax, "%12g ");
 PrintFArr(outf, "\nbbf", bbf, jmax, imax, "%12g ");
 PrintFArr(outf, "\nmdZdz", mdZdz, jmax, imax, "%12g ");
 PrintFArr(outf, "\nmaxZ_hgt", maxZ_hgt, jmax, imax, "%4g ");
 PrintFArr(outf, "\nmaxZ_val", maxZ_val, jmax, imax, "%3g ");
 PrintClassArr(outf, "\nstein_40", stein_40, jmax, imax);
 PrintClassArr(outf, "\nstein_res", stein_res, jmax, imax);
 PrintClassArr(outf, "\nresult", result, jmax, imax);
 PrintClassArr(outf, "\nresult_final", result_final, jmax, imax);
 PrintIArr(outf, "\ndiff", diff, jmax, imax, "%d");
 PrintIArr(outf, "\nout", out, jmax, imax, "%d");
 fclose(outf);

 fprintf(stderr, "  %s done.\n", progNm);
 return 0;
}       /* end of main */

/*************************************************************/
/********************** Global functions **********************/
/*************************************************************/

float
Range(int i0, int j0, int i1, int j1, struct fld fld)
{
 /* Return distance between grid points (i0, j0) and (i1, j1)
  * for mudras field fld */
 double dx, dy;
 dy = fld.y[j1] - fld.y[j0];
 dx = fld.x[i1] - fld.x[i0];
 return sqrt(dy * dy + dx * dx);
}
```

```
float
OrigRange(int i, int j, struct fld fld)
{
 /* Return distance from origin to point (i, j)
  * for mudras field fld */
 return sqrt(fld.y[j] * fld.y[j] + fld.x[i] * fld.x[i]);
}

int IMin(int i, int j) { return (i < j) ? i : j; }
int IMax(int i, int j) { return (i > j) ? i : j; }

float **
Alloc2DFloat(int jmax, int imax)
{
 /*
  * Allocate a 2D data array of floats.
  * Returns a 2D array dimensioned r[jmax][imax], or NULL on failure.
  * Return value can be freed with stdlib function free.
  */

 float **r;      /* Return value */
 int j;  /* Row index */

 r = (float **)malloc(jmax * sizeof(float *) + jmax * imax * sizeof(float));
 if (r) {
  r[0] = (float *)(r + jmax);
  for (j = 0; j < jmax; j++)
   r[j] = *r + imax * j;
 }
 return r;
}

int **
Alloc2DInt(int jmax, int imax)
{
 /*
  * Allocate a 2D data array of integers.
  * Returns a 2D array dimensioned r[jmax][imax], or NULL on failure.
  * Return value can be freed with stdlib function free.
  */

 int **r;        /* Return value */
```

```
 int j;  /* Row index */

 r = (int **)malloc(jmax * sizeof(int *) + jmax * imax * sizeof(int));
 if (r) {
  r[0] = (int *)(r + jmax);
  for (j = 0; j < jmax; j++)
   r[j] = *r + imax * j;
 }
 return r;
}

CLASS **
Alloc2DClass(int jmax, int imax)
{
 /*
  * Allocate a 2D data array of CLASS values.
  * Returns a 2D array dimensioned r[jmax][imax], or NULL on failure.
  * Return value can be freed with stdlib function free.
  */

 CLASS **r;  /* Return value */
 int j;  /* Row index */

 r = (CLASS **)malloc(jmax * sizeof(CLASS *) + jmax * imax * sizeof(CLASS));
 if (r) {
  r[0] = (CLASS *)(r + jmax);
  for (j = 0; j < jmax; j++)
   r[j] = *r + imax * j;
 }
 return r;
}

void
PrintFArr(FILE *fl, char *hdr, float **arr, int jmax, int imax, char *fmt)
{
 /* Print 2D float array arr, dimensioned [jmax][imax] onto stream fl
  * using format fmt */
 int j, i;
 fprintf(fl, "%s\n", hdr);
 for (j = 0; j < jmax; j++) {
  for (i = 0; i < imax; i++) {
   fprintf(fl, fmt, arr[j][i]);
  }
```

```
    fprintf(fl, "\n");
  }
}

void
PrintIArr(FILE *fl, char *hdr, int **arr, int jmax, int imax, char *fmt)
{
 /* Print 2D integer array arr, dimensioned [jmax][imax] onto stream fl
  * using format fmt */
 int j, i;
 fprintf(fl, "%s\n", hdr);
 for (j = 0; j < jmax; j++) {
   for (i = 0; i < imax; i++) {
     fprintf(fl, fmt, arr[j][i]);
   }
   fprintf(fl, "\n");
 }
}

void
PrintClassArr(FILE *fl, char *hdr, CLASS **arr, int jmax, int imax)
{
 /* Print 2D CLASS array arr, dimensioned [jmax][imax] onto stream fl */
 int j, i;
 char pvals[] = {'0', '1', '2'}; /* Printing values */
 fprintf(fl, "%s\n", hdr);
 for (j = 0; j < jmax; j++) {
   for (i = 0; i < imax; i++) {
     fprintf(fl, "%c", pvals[arr[j][i]]);
   }
   fprintf(fl, "\n");
 }
}
```

VITA

Edward T. Amrhein was born to Regis and Patricia Amrhein on October 26, 1967 at Offutt Air Force Base, Bellevue, Nebraska. He graduated from Bishop McNamara High School in Forestville, Maryland in May 1985.

Ed entered the Air Force in November 1985. His first assignment was to Moody Air Force Base near Valdosta, Georgia where he worked as a weather observer. From there he was assigned to the 3rd Weather Squadron at Fort Hood, in Killeen, Texas. While stationed at Fort Hood, he worked as a weather forecaster and deployed with the First Cavalry Division in support of operations Desert Shield and Desert Storm. Upon returning from the Gulf War, Ed served as the WSR-88D site manager for the Granger Radar site.

After spending seven years at Fort Hood, Ed was selected to attend Texas A&M University under the Air Force's Airman Education and Commissioning Program. He graduated from Texas A&M in May 1999 with a Bachelor of Science degree in Meteorology. After completing Officer Training School in August 1999, Ed returned to Texas A&M to pursue a Master of Science degree in Atmospheric Sciences and will graduate in December 2001. Ed's next assignment will be with the Air Force Combat Climatology Center in Asheville, North Carolina.

Ed is married to the former Cynthia L. Buhler of Valdosta, Georgia. They have a daughter Tara. Their permanent address is:

99 Ascension Dr., APT J-108, Asheville, NC 28806